

Towards clinical implementation of quantitative PET and SPECT imaging

Burgt, A. van de

Citation

Burgt, A. van de. (2025, October 21). *Towards clinical implementation of quantitative PET and SPECT imaging*. Retrieved from https://hdl.handle.net/1887/4279582

Version: Publisher's Version

Licence agreement concerning inclusion of doctoral

License: thesis in the Institutional Repository of the University

of Leiden

Downloaded from: https://hdl.handle.net/1887/4279582

Note: To cite this publication please use the final published version (if applicable).

Towards Clinical Implementation of Quantitative PET and SPECT Imaging



Alina van de Burgt

TOWARDS CLINICAL IMPLEMENTATION OF QUANTITATIVE PET AND SPECT IMAGING

Copyright © Alina van de Burgt, Amsterdam, The Netherlands 2025
All rights reserved. No part of this work may be reproduced in any form by any means, without prior permission of the author.
Author: Alina van de Burgt Printing: Ridderprint, ridderprint.nl Layout and design: Indah Hijmans, persoonlijkproefschrift.nl Cover images: Alina van de Burgt Cover design: Indah Hijmans ISBN: 978-94-6522-614-9

Towards Clinical Implementation of Quantitative PET and SPECT Imaging

Proefschrift

ter verkrijging van

de graad van doctor aan de Universiteit Leiden,
op gezag van rector magnificus prof.dr.ir. H. Bijl,
volgens besluit van het college voor promoties
te verdedigen op dinsdag 21 oktober 2025

klokke 10.00 uur

door

Alina van de Burgt

geboren te Arnhem

in 1993

Promotor

Prof. dr. L.F. de Geus-Oei

Co-promotors

Dr. F.H.P. van Velden

Dr. I.A. Dekkers Amsterdam University Medical Center

Leden promotiecommissie

Prof. dr. R.J. Bennink

Prof. dr. M. Lubberink University Hospital Uppsala

Dr. J. R. Kroep

Dr. J. van Sluis University Medical Center Groningen

TABLE OF CONTENTS

Chapter 1	General introduction and outline	7
Part 1: Nove	el clinical quantitative PET/CT applications	
Chapter 2	Dynamic rubidium-82 PET/CT as a novel tool for quantifying hemodynamic differences in renal blood flow using a one-tissue compartment model	17
Chapter 3	Investigating the potential added value of [18F]FDG-PET/CT in long COVID patients with persistent symptoms: a proof of concept study	41
Chapter 4	[¹⁸ F]FDG administered activity reduction capabilities of a 32-cm axial field-of-view solid-state digital bismuth germanium oxide PET/CT system while maintaining EARL compliance	59
Part 2: Nove	el clinical quantitative SPECT/CT applications	
Chapter 5	Experimental validation of absolute SPECT/CT quantification for response monitoring in patients with coronary artery disease	75
Chapter 6	Comparison between prone SPECT-based semi-quantitative parameters and MBI-based semi-quantitative parameters in patients with Locally Advanced Breast Cancer	93
Chapter 7	Summary, General Discussion and Future Perspectives	111
Chapter 8	Nederlandse Samenvatting (Dutch Summary)	129
Appendices	Curriculum vitae	137
	List of publications	138
	Dankwoord	140



CHAPTER 1

General introduction and outline

Since its introduction in the late 1940s, nuclear medicine has become essential in healthcare for diagnosis, staging, and treatment by providing unique insights into in vivo physiological and metabolic functions. Nuclear imaging makes use of radiotracers, small amounts of chemical compounds labelled with radioactive isotopes, to image the distribution of the radiotracer within the body [1]. Attributed to a variety of radiotracers that have been developed, multiple tissue functions can be visualized including perfusion, metabolism, receptor systems and hypoxia [2], offering insights across various medical disciplines. Single Photon Emission Computed Tomography (SPECT) is the most widely adopted camera using gamma-emitting radiotracers to generate three-dimensional (3D) images of the body. Another frequently used nuclear imaging technique is Positron Emission Tomography (PET) which detects pairs of annihilated gamma photons emitted by positron-emitting isotopes to compose a 3D image. Integrating SPECT or PET with Computed Tomography (CT) provides anatomical information and enables attenuation correction by compensating for photon absorption in different tissues. [2, 3]

Qualitative image evaluation, which relies on the visual interpretation of radiotracer uptake and tissue density on CT, has been the primary approach in nuclear imaging since its introduction in healthcare. This method is essential for diagnosing diseases and assessing their presence and progression. The limitation of visual interpretation is that it might lead to observer variability, causing inconsistent and unreliable imaging data interpretations. Especially when we want to monitor the course of a disease or determine the response to therapy, we need to be able to measure whether there is an increase or decrease in tracer uptake. In such cases, in addition to visual inspection, accurate quantification tools are highly beneficial, and almost unaffected by inter-observer variability. Quantifying radioactivity concentration within a tissue volume supports personalized treatment through dosimetry calculations, optimizing therapeutic efficacy, while also enabling early disease detection by identifying subtle metabolic changes before structural abnormalities become apparent on conventional imaging [4]. Recent developments in nuclear medicine have enabled (semi-)quantitative analysis as a complementary assessment to visual interpretation, enabling objective measurements of concentrations of radiotracers in tissues, metabolic rates, and functional activity of organs.

QUANTITATIVE PET/CT

PET is widely known as a quantitative imaging tool due to its ability to calibrate voxel values in reconstructed images to absolute units of radioactivity concentration with high accuracy and precision [5]. This facilitates accurate interpretation of PET images by representing underlying physiology in absolute units and enables tracer kinetic modelling

for quantifying physiological parameters. Various factors influence the accuracy of PET imaging. Count-rate losses, detector efficiency variations, scattered coincidences, and signal dilution (partial volume effect), amongst others, significantly affect PET accuracy, necessitating precise corrections to preserve image quality [2]. Advances in radiotracer development, image reconstruction algorithms, and correction methods continue to enhance the capabilities of PET/CT. The implementation of quantitative PET/CT is slowly expanding within clinical practice.

Standardized Uptake Value (SUV) is commonly used for assessing radiotracer uptake in tumors and other tissues [6]. The SUV, measured in [g/mL], represents the ratio of the local activity concentration to the decay-corrected quantity of injected radiotracer predominantly per unit of body weight. This metric reflects the concentration of the radiotracer in a particular area relative to its uniform distribution across the body. SUV is useful for comparing measurements within an individual against standard values from a reference population. Additionally, it enables the longitudinal tracking of subtle changes in the body, whether due to disease progression, response to therapy, treatment related effects on (normal) tissues or physiological day-to-day variations in the human body.

A single static image can be captured at a specific moment after radiotracer injection, or the radioactivity can be continuously monitored over time. When the right radiotracer is chosen and suitable imaging conditions are applied, the activity values measured in a region of interest (ROI) in the image should primarily reflect the physiological characteristic of interest, such as blood flow, metabolism or receptor concentration. A kinetic model seeks to describe the relationship between these measurements and the parameters of interest. Essentially, an accurate tracer kinetic model can account for a proximity of the biological factors contributing to the tissue radioactivity signal. Kinetic tracer modelling, including dynamic PET analysis, are employed to measure absolute parameters such as blood flow, volume of distribution, metabolic rate and binding potential. [5]

Advancements in PET/CT technology have improved image quality and sensitivity, enhancing diagnostic accuracy and potentially improving patient outcomes [7]. The integration of precision deep learning-based image enhancement further sharpens features and accelerates convergence [8]. Increased sensitivity enables possibilities to reduce both scan duration and/or the administered activity of radiopharmaceuticals. Shorter scan durations may enhance patient comfort, increase patient throughput and decrease motion effects. [9]. However, limited literature exists on cutting-edge PET/CT systems, making a thorough evaluation of their scan-time and administered activity reduction capabilities essential before widespread implementation.

QUANTITATIVE SPECT/CT

Historically, gamma cameras assessed relative uptake of radiopharmaceuticals, while PET imaging provided absolute quantification with units like kBq/mL that can be used for detailed 3D disease assessment. Although, in a clinical setting, SPECT/CT was once seen as less advanced than PET/CT, recent advancements in iterative image reconstruction have improved its capabilities. These advancements allow (semi-)quantification of SPECT/CT by incorporating compensation for collimator—detector response, photon attenuation, and scatter, as well as resolution recovery into the reconstruction process, greatly enhancing its quantitative accuracy. [10] Consequently, SPECT/CT enables the measurement of (semi-)quantitative imaging features based on SUV, leading to more accurate measurements for various clinical applications.

However, quantitative SPECT presents more challenges compared to PET due to the increased number of variables involved, including radionuclides with differing photon energies, various collimators, the possibility of using multiple energy windows, and the potential for performance drifts given the greater number of moving parts in a SPECT system [11]. Despite these complexities, SPECT is evolving from a primarily qualitative modality to one that also incorporates (semi-)quantification for clinical evaluation.

AIM

Quantitative PET and SPECT have significantly advanced over the past decades and are integrated into clinical guidelines, particularly for oncology, neurology, cardiology, inflammation and infection. However, there is substantial potential for broader use of quantitative PET and SPECT across other indications and fields, suggesting that existing capabilities remain underutilized. A key barrier is the lack of robust evidence, underscoring the need for further research to validate their expanded applications, including in drug development. This would support the development of tailored treatment plans, ultimately improving outcomes across a wider range of diseases.

The general aim of this thesis is to deepen the understanding of quantitative PET and SPECT in clinical settings, explore their potential beyond current applications, and establish a foundation for their broader implementation in clinical practice.

OUTLINE OF THESIS

This thesis consists of two parts. **Part 1** explores two novel applications of quantitative PET/CT and focusses on a novel PET/CT scanner with precision deep learning for improved feature sharpness comparable to time-of-flight reconstruction.

Assessing renal perfusion in-vivo is challenging and quantitative information regarding renal hemodynamics is hardly incorporated in medical decision-making while abnormal renal hemodynamics might play a crucial role in the onset and progression of renal disease. Combining physiological stimuli with [82Rb]Cl PET/CT offers opportunities to test the kidney perfusion under various conditions. **Chapter 2** investigates the application of a one-tissue compartment model for measuring renal hemodynamics using dynamic [82Rb]Cl PET/CT imaging, and whether dynamic PET/CT is sensitive to detect differences in renal hemodynamics in stress compared to rest.

Since the end of 2019, the coronavirus disease 2019 (COVID-19) virus has infected millions of people, of whom a significant group suffers from sequelae from COVID-19, termed long COVID. **Chapter 3** outlines the potential added value of non-metabolizable glucose analogue 2-[18F]fluoro-2-deoxy-D-glucose ([18F]FDG)-PET/CT for this group of long COVID patients.

The enhanced sensitivity allows shorter scan durations, improving patient comfort, throughput, and reducing motion effects, or lowering the administered radiopharmaceutical activity to save costs and minimize radiation risks for staff and patients. Furthermore, a lower dose and/or reduced costs could potentially open up new applications for (quantitative) PET. **Chapter 4** assesses the lower [18F]FDG limit in administered activity and/or scan time reduction capabilities of a digital bismuth germanium oxide 32-cm axial field-of-view PET system while being compliant with current and updated EANM Research Ltd Fluorine-18 accreditation specifications (EARL, and EARL, respectively).

Part 2 presents two potential clinical applications of quantitative SPECT/CT. **Chapter 5** investigates the quantitative accuracy and precision of a novel iterative reconstruction technique for the potential application of response monitoring using [99mTc]Tc-tetrofosmin SPECT/CT in patients with coronary artery disease. **Chapter 6** evaluates the semi-quantitative SPECT parameters of prone SPECT using [99mTc]Tc-sestamibi and compares them with Molecular Breast Imaging (MBI)-derived semi-quantitative parameters for the potential use of response prediction in women with locally advanced breast cancer.

Chapter 7 provides a summary, general discussion and future perspectives in English and **Chapter 8** a summary in Dutch.

REFERENCES

- Weber WA, Czernin J, Anderson CJ, Badawi RD, Barthel H, Bengel F, et al. The future of nuclear medicine. molecular imaging. and theranostics. Journal of Nuclear Medicine. 2020;61:263S-72S.
- 2. Cherry SR, Sorenson JA, Phelps ME. Physics in Nuclear Medicine: Elsevier Health Sciences; 2012.
- 3. Zaidi H. Quantitative analysis in nuclear medicine imaging: Springer; 2006.
- Frey EC, Humm JL, Ljungberg M. Accuracy and precision of radioactivity quantification in nuclear medicine images. Semin Nucl Med. 2012;42:208-18.
- 5. Bailey DL, Maisey MN, Townsend DW, Valk PE. Positron emission tomography: Springer; 2005.
- Boellaard R, Delgado-Bolton R, Oyen WJ, Giammarile F, Tatsch K, Eschner W, et al. FDG PET/ CT: EANM procedure guidelines for tumour imaging: version 2.0. Eur J Nucl Med Mol imaging. 2015;42:328-54.
- Singh M. A review of digital PET-CT technology: comparing performance parameters in SiPM integrated digital PET-CT systems. Radiography (Lond). 2024;30:13-20.
- 8. Mehranian A, Wollenweber SD, Walker MD, Bradley KM, Fielding PA, Huellner M, et al. Deep learning—based time-of-flight (ToF) image enhancement of non-ToF PET scans. Eur J Nucl Med Mol Imaging. 2022;49:3740-9.
- Kennedy JA, Palchan-Hazan T, Maronnier Q, Caselles O, Courbon F, Levy M, et al. An extended bore length solid-state digital-BGO PET/CT system: design, preliminary experience, and performance characteristics. Eur J Nucl Medi Mol Imaging. 2024;51:954-64.
- Bailey DL, Willowson KP. An evidence-based review of quantitative SPECT imaging and potential clinical applications. Journal of Nuclear Medicine. 2013;54:83-9.
- Bailey DL, Willowson KP. Quantitative SPECT/CT: SPECT joins PET as a quantitative imaging modality. European Journal of Nuclear Medicine Molecular Imaging. 2014;41:17-25. doi:10.1007/ s00259-013-2542-4.



PART 1

Novel clinical applications of quantitative PET/CT



CHAPTER 2

Dynamic rubidium-82 PET/CT as a novel tool for quantifying hemodynamic differences in renal blood flow using a one-tissue compartment model

Authors

A. van de Burgt, F.H.P. van Velden, K. Kwakkenbos, F. Smit, L.F. de Geus-Oei and I. A. Dekkers

Published

Medical Physics, 2024; 51(6): 4069-408, DOI: 10.1002/mp.17080

Supplementary materials

https://doi.org/10.1002/mp.17080

ABSTRACT

Background

Assessing renal perfusion in-vivo is challenging and quantitative information regarding renal hemodynamics is hardly incorporated in medical decision-making while abnormal renal hemodynamics might play a crucial role in the onset and progression of renal disease. Combining physiological stimuli with Rubidium-82 positron emission tomography/computed tomography (82Rb PET/CT) offers opportunities to test the kidney perfusion under various conditions.

Purpose

The aim of this study is: 1) to investigate the application of a one-tissue compartment model for measuring renal hemodynamics with dynamic ⁸²Rb PET/CT imaging, and 2) to evaluate whether dynamic PET/CT is sensitive to detect differences in renal hemodynamics in stress conditions compared to resting state.

Methods

A one-tissue compartment model for the kidney was applied to cardiac ⁸²Rb PET/CT scans that were obtained for ischemia detection as part of clinical care. Retrospective data, collected from 17 patients undergoing dynamic myocardial ⁸²Rb PET/CT imaging in rest, were used to evaluate various CT-based volumes of interest (VOIs) of the kidney. Subsequently, retrospective data, collected from 10 patients (5 impaired kidney function and 5 controls) undergoing dynamic myocardial ⁸²Rb PET/CT imaging, were used to evaluate image-derived input functions (IDIFs), PET-based VOIs of the kidney, extraction fractions and whether dynamic ⁸²Rb PET/CT can measure renal hemodynamics differences using the renal blood flow (RBF) values in rest and after exposure to adenosine pharmacological stress.

Results

The delivery rate (K_1) values showed no significant (p=0.14) difference between the mean standard deviation (SD) K_1 values using one CT-based VOI and the use of two, three and four CT-based VOIs, respectively 2.01(0.32), 1.90(0.40), 1.93(0.39) and 1.94(0.40) mL/min/mL. The ratio between RBF in rest and RBF in pharmacological stress for the controls were overall significantly lower compared to the impaired kidney function group for both PET-based delineation methods (region growing and iso-contouring), with the smallest median interquartile range (IQR) of 0.40(0.28-0.66) and 0.96(0.62-1.15), respectively (p<0.05). The K_1 of the impaired kidney function group were close to 1.0 mL/min/mL.

Conclusions

This study demonstrated that obtaining renal K_1 and RBF values using \$2Rb PET/CT was feasible using a one-tissue compartment model. Applying iso-contouring as the PET-based VOI of the kidney and using AA as an IDIF is suggested for consideration in further studies. Dynamic \$2Rb PET/CT imaging showed significant differences in renal hemodynamics in rest compared to when exposed to adenosine. This indicates that dynamic \$2Rb PET/CT has potential to detect differences in renal hemodynamics in stress conditions compared to the resting state, and might be useful as a novel diagnostic tool for assessing renal perfusion.

Keywords

⁸²Rb PET/CT, dynamic rubidium-82 PET/CT, one-tissue compartment model, renal blood flow, renal hemodynamics, renal perfusion

INTRODUCTION

The prevalence of chronic kidney disease (CKD) is projected to substantially increase upcoming decades, requiring new strategies for earlier diagnosis [1, 2]. The human kidney receives ca. 20% of cardiac output and disturbances in renal blood flow might play a major role in CKD [3]. However, evaluation of renal macro- and microcirculation is currently unused, since validated non-invasive methods for assessing kidney perfusion are lacking.

Imaging has important benefits for determining renal perfusion compared to time-honoured gold standard methods such as para-aminohippurate clearance; it is less invasive, faster and allows for regional comparison within the kidney and between the kidneys [3, 4, 5, 6]. [150]H₂O positron emission tomography/computed tomography (PET/CT) is a widely used technique to assess renal perfusion [3]. However, Rubidium-82 (82Rb) PET/CT might be an alternative technique, which is easy to implement as it does not require an on-site cyclotron.

82Rb PET/CT is increasingly being used for cardiac perfusion imaging. The flow tracer 82Rb accumulates in the cells, has a short physical half-life (75 s) and a high first-pass extraction in the kidneys that also enables renal perfusion quantification, but is not yet used for this application in clinical practice. From renal physiology studies it is known that kidney function increases after a stimulus such as an oral protein load or an intravenous infusion with amino acids, glucagon or dopamine[5]. Combining physiological stimuli with 82Rb PET/CT offers unique opportunities to test the kidney under various conditions making dynamic 82Rb PET/CT an interesting technique for dedicated renal stress testing [6-9].

One-tissue compartment models have been validated for myocardial blood flow quantification and are currently in routine clinical use [10, 11]. Previous work by Tahari et al. and Langaa et al. demonstrated the feasibility of ⁸²Rb PET/CT with one-tissue compartment models for assessing renal perfusion [12, 13]. However, there is no uniform approach regarding kidney compartment modelling and hence further research is necessary to investigate the effect of various inputs, outputs and extraction fractions on the renal blood flows to enable evaluation of disease activity and treatment response monitoring. Therefore, the aim of this study is: 1) to investigate the application of a one-tissue compartment model for measuring renal hemodynamics with dynamic ⁸²Rb PET/CT imaging, and 2) to evaluate whether dynamic PET/CT is sensitive to detect differences in renal hemodynamics in stress conditions compared to resting state.

MATERIALS AND METHODS

Study design

This was a retrospective proof-of-concept study and a waiver was obtained by the medical ethical review board to perform this study. Written informed consent was obtained from all participants. Clinical characteristics were collected from patient records and the ⁸²Rb PET/CT reports.

Population

Patients coming for a myocardial perfusion ⁸²Rb PET/CT in the period between March 2020 and November 2022 were retrospectively selected based on the amount of kidney tissue in the field of view (FoV). At least 5.7 cm (15 consecutive CT slices) of the most superior kidney on the CT data was required to perform the analysis.

Two different patient datasets were used in this study: (A) dynamic rest myocardial 82 Rb PET/CT data (N=17) were used to evaluate various manual CT-based volume of interest (VOIs) methods of the kidney with one-tissue compartment models to district between the cortex and the medulla. Subsequently, (B) dynamic myocardial rest and pharmacological stress 82 Rb PET/CT data with adenosine were selected to illustrate the effects of various semi-automatic PET-based kidney delineations, image derived input functions (IDIFs) and extraction fractions to convert the delivery rate (K_1) values to flow values, and to assess the resulting differences in renal hemodynamics in stress conditions compared to resting state with 82 Rb PET/CT imaging (N=10, 5 impaired kidney function and 5 controls). The 5 subjects with impaired kidney function were selected based on an eGFR < 60 mL/min/1.73 m² [14]. As comparison 5 subjects (considered as controls) without history of cardiovascular disease or interventions, calcium score 0, MFR >1.5, no cardiac perfusion defects, chronic obstructive pulmonary disease (COPD), lung emphysema, malignancies other than T1 locally resected, diabetes mellitus type 1 (DM1) or type 2 (DM2) were selected.

Data collection

PET/CT images were obtained on a Discovery MI 5-Ring PET/CT (GE Healthcare, Chicago, Illinois, USA). A low dose CT (20 mAs, 120 kV) was acquired for attenuation correction purposes and reconstructed in a 512 by 512 matrix and a FoV of 70 cm (with a voxel size of $1.4 \times 1.4 \times 3.75$ mm³).

PET data were acquired during a period of 6 min, starting 8 s after the automatic intravenous infusion of a bolus of approximately 750 MBq ⁸²RbCl (⁸²Sr/⁸²Rb generator, Rubigen B.V., 's Hertogenbosch, the Netherlands) in a resting state (referred to rest

acquisition). Subsequently, a second acquisition was started following the same protocol with similar activity 2.5 min after an adenosine infusion (140 μ g/kg/min over 6 min) (referred to as the stress acquisition).

PET data were acquired in list mode and reconstructed in multiple time frames using a time-of-flight ordered subset expectation maximization algorithm (VPFX TOF-OSEM; 2 subsets, 17 iterations) on a 128 by 128 matrix (with a voxel size of $2.8 \times 2.8 \times 2.8 \text{ mm}^3$) with a 5.0 mm full-width-at-half maximum (FWHM) Hanning filter. A total of 26 time frames were reconstructed per PET scan, i.e. 10x5s, 6x10s, 5x15s and finally 5x20s. Images were normalized and corrected for radioactive decay, attenuation and scatter.

Kinetic modelling

An existing one-tissue compartment model was used to calculate global K_1 values based on renal one-tissue compartment models from previous studies [12, 13], as depicted in Figure 1.

PMOD software package (version 4.2; PMOD Technologies Ltd., Zurich, Switzerland) was used for kinetic modelling. Equation (1) shows the change in ⁸²Rb concentration in the kidney compartment:

$$rac{dC_{k}\left(t
ight)}{dt}=K_{1}C_{A}\left(t
ight)-k_{2}C_{k}\left(t
ight) ag{7}$$

In this equation, the rate constant K_1 denotes the perfusion-dependent component and has unit mL/min/mL. The rate constant k_2 indicates the rate in which the ⁸²Rb leaves the kidney parenchyma and has unit min⁻¹. Furthermore, the functions C_A and C_k represent the concentration (kBq/mL) per timepoint in the vascular input and the kidney parenchyma, respectively. For the input C_A in equation (3) we used an IDIF, as no blood samples were drawn from patients during scanning. Equation (1) can be analytically solved, yielding:

$$C_{k}(t) = K_{1} \int_{0}^{t} C_{A}(t) e^{-k_{2}(t-\tau)} d\tau$$
 (2)

Which can be expressed as a convolution:

$$C_{k}\left(t\right) = K_{1}e^{-k_{2}t} * C_{A}\left(t\right) \tag{3}$$

Finally, an operational model curve is fitted by PMOD, considering the blood volume fraction (v_p) :

$$C_{\text{model}} = (1 - v_B) C_k(t) + v_B C_A(t)$$

$$\tag{4}$$

A constant value of 0.10 for v_B was used to account for activity from the fractional blood volume within the VOI, as previously used by Langaa et al. [13, 15]. The rate constants K_I and k_2 were estimated in PMOD by means of a least-squares method in an iterative manner, with a maximum of 20 random iterations. This was done by curve fitting which started with establishing a set of initial parameter values, from which the corresponding model curve was generated. Subsequently, the Chi-square criterion was computed, prompting adjustments to the model parameters with the goal of reducing Chi-square. Multiple fitting iterations were performed, and the result parameters were selected from the fit with the minimal chi-squared value. In this context, randomness entailed that fitting began with randomized sets of initial parameters, utilizing a uniform distribution within a $\pm 100\%$ range. This intentional introduction of randomness served the purpose of preventing convergence into local minima [16]. In preliminary experiments (data not shown), this number of iterations was found to be sufficient for PMOD to find a stable minimum.

Accurate measurement of the time base of the input signal is crucial for flow tracers with high first-pass extraction as $[^{15}O]H_2O$ and likely ^{82}Rb . Therefore, in line with existing literature, correction for delay and dispersion in the blood signal is essential [17-19]. The operational equations 1 to 4 provided above require modification to accommodate these factors. Equation 5 represents the relationship between measured and actual arterial concentration time courses.

$$\frac{dC_A^*(t)}{dt} = \frac{1}{\tau_d} \left(C_A(t - \Delta t) - C_A^*(t) \right) \tag{5}$$

In this equation C_A^* represents the measured arterial concentration (kBq/mL) per timepoint in the vascular input and C_A the true arterial concentration. The delay in units of time is represented as Δt and τ_d is the dispersion constant in units of min. Solving and substituting this equation into the prior operational equations 1 to 4 allows fitting for delay and dispersion. The correction of delay was performed in PMOD by fitting the delay together with the kinetic parameters of the tissue model [16]. The lower limit was fixed at 0, as kidney uptake cannot occur before the ⁸²Rb bolus injection. The correction for dispersion could be incorporated into the one-tissue compartment model and solved using the Laplace transform to yield the equation 4, as described by E. Meyer [20].

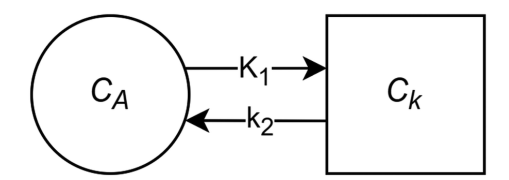


Figure 1. A visual representation of a one-tissue compartment model: C_A , vascular compartment; C_k , tissue compartment; K_1 , uptake rate of Rubidium-82 from the vascular compartment to the tissue compartment; k_2 , fraction of Rubidium-82 from the tissue compartment to the vascular compartment.

Various kidney VOI delineation methods

Manual delineations on CT

Using the rest dynamic 82 Rb PET/CT scans from dataset A (N=17), various manual kidney VOI delineations on CT were evaluated to assess K_1 values of a combination of different parts of the kidney. VOIs were placed in the upper pole of the left kidney on an axial view of CT scan. CT-based delineation was applied with one fixed sphere (radius of 10 mm) for one VOI and two, three or four fixed cuboids (5 mm x 10 mm x 10 mm) between the medulla and the cortex for multiple VOIs. In case two, three or four cuboids were placed in the kidney, the first VOI was placed medial (two voxels from the right of the calyx). The second VOI was placed on the same CT slice, but two voxels from the lateral kidney boundary. Subsequently, the remainder third and fourth cuboids were set between the first and second cuboids. Finally, VOI translation from CT to PET data was executed, as depicted in Figure S-1.

Effects of spill-over and partial volume were minimized by placement of the VOIs at least two voxels away from kidney boundary walls. The renal pelvis was not included in the VOI. The VOIs were not placed in the three most superior and inferior slides of the FoV, as these slides could have a slightly reduced spatial resolution as compared with more central slides of the FoV [21]. The position of the VOIs was checked for patient motion in every frame and slice.

Semi-automatic PET-based delineations

Because CT contrast agents are not clinically used in myocardial ⁸²Rb PET/CT imaging for the detection of ischemia, two other semi-automatic kidney delineation methods on PET were also explored using pharmacological stress data (dataset B, N=10), being (1) hot contouring with manual placement of a seed point and (2) an iso-contouring delineation method, only requiring the placement of a bounding box and a percentage. For the iso-contouring delineation method, a kidney VOI was placed in the average of the rest scan

over time, as described in previous studies for VOI delineation of the left ventricle wall [11] and the carotid arteries [22]. In this study, a bounding box was placed around the kidney volume, after which the iso-contour was automatically generated representing 40% of the maximum within the bounding box. The region growing method required the manual identification of a temporal frame showing high signal in the entire kidney volume and placing a seed point. These delineations were repeated in order to assess the intraobserver variability for establishing the renal blood flow in rest and stress.

Image-derived input functions

A 3D sphere with a radius of 10 mm was placed in the left ventricular blood pool (LVBP) and ascending thoracic aorta (ATA) and a 3D sphere with a radius of 5 mm was placed in the abdominal aorta (AA). VOIs were placed as centrally as possible in the vessels and the ventricle, avoiding delineation of the walls, to minimize partial volume effects and spill over, respectively. An overview of the IDIF delineations is depicted in Figure S-1.

After the placement of IDIFs and VOIs, time-activity curves (TACs) were generated depicting the mean activity concentrations in kBq/mL of ⁸²Rb per region over time (s) (Figure 2).

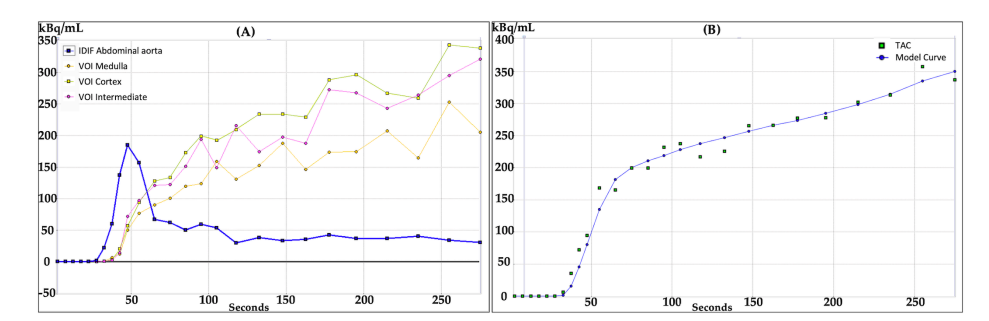


Figure 2. Time activity Curves (TAC) after applying a volume of interest (VOI) of kidney tissue using the abdominal aorta as image derived input function. (A) Unfitted time-activity curves of three VOIs. (B) Fitted TAC of one of the kidney tissue VOIs. VOI delineations on CT were applied between the medulla and the cortex.

Renal blood flow and renovascular reserve

K, is a product of flow (F) and the extraction factor (E) as calculated by equation (6):

$$K_1 = F \cdot E \tag{6}$$

The extraction factor can either be a constant value or derived from a Renkin-Crone function [23, 24]. The latter is given in equation (7), and is thought to be flow-dependent for ⁸²Rb:

$$K_1 = F \cdot \left(1 - a \cdot e^{-b/F}\right) \tag{7}$$

To convert the K, values to flow values, two approaches were evaluated:

- (i) assuming a constant extraction fraction of 0.9 as determined in canine experiments [7],
- (ii) using the values found by Gregg et al.[25] for the kidney: a = 0.94 and b = 1.86

All flow values were converted to mL/min/g by assuming a kidney density of 1.04 g/mL [26, 27].

Research suggests that a state of net vasodilation also occurs in kidney vasculature, but can be preceded by vasoconstriction of the afferent arterioles [28, 29]. We assume that an increase in renal functioning when exposed to a stimulus (stress) is accompanied by an increase in renal blood flow (RBF), and that the ratio compared to when such a stimulus is not present (rest) can be used for the measurement of renal hemodynamics. In this study we refer to this ratio of RBF during exposure to adenosine (stress) compared to rest as the renovascular reserve (RVR). The RVR is calculated using equation (8). This new parameter is similar to the coronary flow reserve used in clinical practice for assessing conditions affecting the coronary arteries.

Renovascular reserve
$$=\frac{RBF_{stress}}{RBF_{rest}}$$
 (8)

Statistical analysis

A Shapiro-Wilk test was performed to evaluate the (log)normality of the data. The statistical analyses of the non-paired data were performed with an independent T test or Mann-Whitney U depending on the (log)normality. Continuous data were expressed as mean standard deviation (SD) or median interquartile range (IQR) depending on (log) normality. Paired data were statistically performed with the paired T-test or Wilcoxon Signed Rank test depending on the (log)normality. A one-way repeated measures ANOVA was performed to compare the total K_1 values between the number of kidney VOIs. The RVRs and RBFs of both study arms were compared using the Wilcoxon rank-sum (Mann-Whitney U) test. A P-value < 0.05 was deemed significant.

Bland-Altman plots were composed to assess the intraobserver variability for establishing the RVR. Statistical analysis was performed using the statistics module SciPy (version 1.9.2) of Python (version 3.11) and Graphpad Prism (version 9.3.1; GraphPad Software, San Diego, California USA) [30].

RESULTS

Evaluation of various kidney VOI delineation methods on CT

 $\rm K_1$ values were composed for various kidney VOIs using AA as IDIF (dataset A, N=17), as depicted in Figure 3. The $\rm K_1$ values showed no significant (p=0.14) difference between the mean(SD) $\rm K_1$ values applying one VOI and the use of two, three and four VOIs, respectively 2.01(0.32), 1.90(0.40), 1.93(0.39) and 1.94(0.40) mL/min/mL. When two VOIs were applied, no significant difference (p=0.10) was found between the two VOIs in mean(SD) $\rm K_1$ values, respectively 1.81(0.39) and 1.98(0.50) mL/min/mL. Furthermore, significant differences (p<0.05) were identified between the VOIs of the three and four VOIs placements with mean(SD) $\rm K_1$ values, respectively 1.73(0.35), 2.12(0.52), 1.94(0.45) mL/min/mL and 1.65(0.36), 2.04(0.50), 2.12(0.56), 1.94(0.45) mL/min/mL. However, the deviation between the mean $\rm K_1$ values of applying one VOI is significantly smaller (p<0.05) compared to the SD applying two, three or four VOIs (max SD of one VOI; 0.32 versus four VOIs 0.56 mL/min/mL).

Evaluation of renal hemodynamics

For the remainder of the study, dataset B was used for the evaluation of renal hemodynamics (Table S-1). The obtained K_1 values are depicted in Figure 4 per IDIF (AA, ATA and LVBP) and per kidney delineation method (iso-contouring and region growing). The data showed a decrease in K_1 values in stress compared to rest for controls and patients with median impaired kidney function of 20.6% and 7.9%, respectively, when iso-contouring and AA as IDIF were applied. The K_1 values of this impaired kidney function group were close to 1.0. The numeric K_1 values, k_2 values and blood delay time per patient were reported in Table S-2.

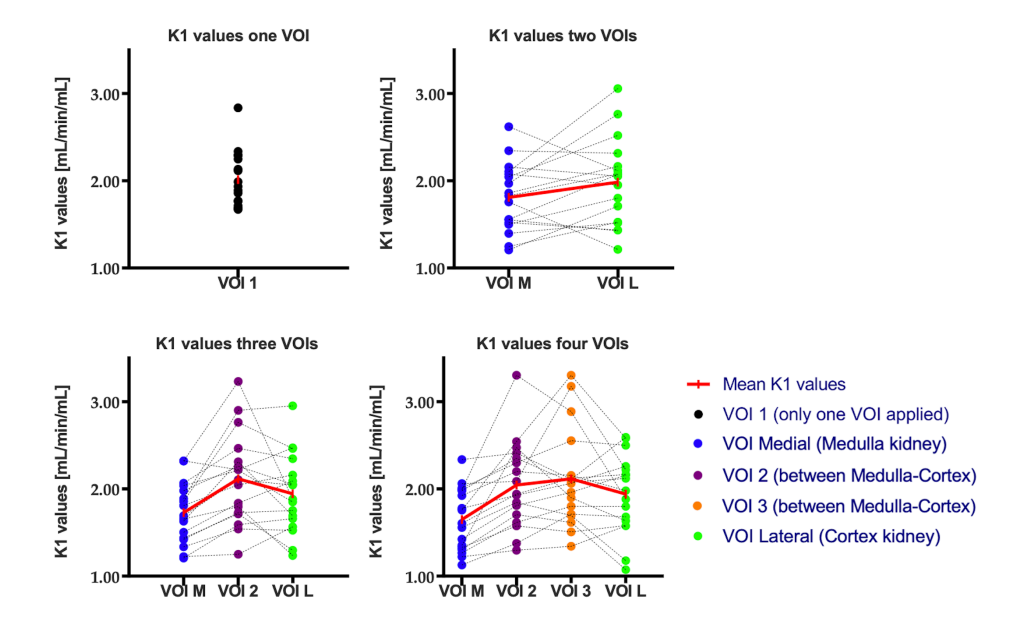


Figure 3. Visualization of K_1 values in mL/min/mL applying one or more volume of interest (VOI) of kidney tissue using the abdominal aorta as image derived input function (N=17). CT-delineation was applied with one fixed sphere (radius of 10 mm) for one VOI and two, three or four fixed cuboids (5 mm x 10 mm x 10 mm) between the medulla and the cortex for multiple VOIs. In case two, three or four cuboids were placed in the kidney, the first VOI was placed medial (two voxels from the right of the calyx). The second VOI was placed on the same CT slice, but two voxels from the lateral kidney boundary. Subsequently, the remainder third and fourth cuboids were set between the first and second cuboids. Every dot represents a K1 value of a subject (N=17).

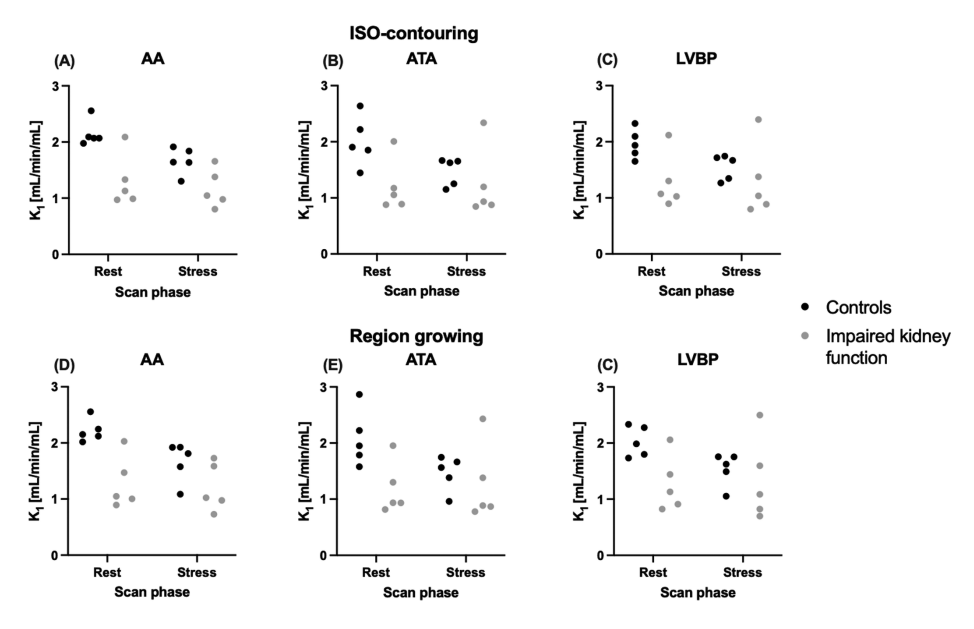


Figure 4. K_1 values from a one-tissue compartment model for the abdominal aorta (AA), ascending thoracic aorta (ATA) and left ventricular blood pool (LVBP) as vascular input functions. The figures A, B and C denote the models obtained by delineation the kidney using iso-contouring and D, E and F using region growing (dataset B, N=10)

RBF and RVR

RBF data (mL/min/g) are provided in Table S-3 (rest) and Table S-4 (stress). No significant differences in RBF between the control and impaired kidney group were found in stress state and in rest state (p>0.05). Furthermore, no significant differences between the two kidney delineations methods for both the rest and stress were found with regards to flow values (p>0.05). For the rest phase, no significant differences were found between the different IDIFs (p>0.05). In the stress phase, significant differences were identified between the LVBP and the ATA for all three flow methods, within the iso-contouring delineation method (p<0.05).

RVR data are presented in Table 1. The control group showed a larger range of values compared to the impaired kidney function group, the latter having median RVR values close to 1.0. The highest median RVR value in the control group was 0.81 (IQR: 0.75-0.82) when a constant extraction combined was applied with iso-contouring and the LVBP as input. The smallest median RVR values were found with flows calculated with Gregg's extraction and the ATA input and were 0.40 (IQR: 0.28-0.66) and 0.40 (IQR: 0.23-0.70) for iso-contouring and region growing, respectively. For the impaired kidney function group, the smallest median RVR value was 0.96 (IQR: 0.62-1.15), calculated with Gregg's

extraction fraction. The ATA IDIF yielded significant differences between the control and the impaired kidney function group for both extraction methods and both kidney delineation methods (p<0.05). RVR calculated using Gregg's method resulted in significant differences in all VOIs except for the AA obtained using region growing.

Table 1. Renovascular reserve (RVR) values as the ratio of renal blood flow in during adenosine (stress) compared to RBF in rest. RVR values were obtained of dataset B (N=10) with various IDIFs derived from abdominal aorta (AA), ascending thoracic aorta (ATA) and left ventricular blood pool (LVBP), two kidney volume of interest methods (Iso-contouring (ISO) and region growing (RG)) and two extraction methods (constant and Gregg). Values are displayed as median (interquartile range).

Adenosine reno	Adenosine renovascular reserve values							
Flow method	VOIs	Control	Impaired kidney function	Р				
	AA							
	ISO	0.79 (0.75-0.83)	0.99 (0.79-1.04)	0.251				
	RG	0.75 (0.70-0.84)	0.98 (0.85-1.08)	0.076				
	ATA							
Constant	ISO	0.74 (0.62-0.86)	1.02 (0.96-1.05)	0.028				
	RG	0.75 (0.55-0.88)	1.06 (0.95-1.07)	0.028				
	LVBP							
	ISO	0.81 (0.75-0.82)	0.99 (0.97-1.06)	0.047				
	RG	0.75 (0.71-0.83)	1.00 (0.96-1.11)	0.028				
	AA							
	ISO	0.48 (0.43-0.55)	0.98 (0.57-1.09)	0.076				
	RG	0.44 (0.33-0.58)	0.96 (0.62-1.15)	0.028				
	ATA							
Gregg	ISO	0.40 (0.28-0.66)	1.04 (0.95-1.08)	0.009				
	RG	0.40 (0.23-0.70)	1.10 (0.92-1.15)	0.009				
	LVBP							
	ISO	0.53 (0.41-0.57)	0.98 (0.94-1.14)	0.009				
	RG	0.41 (0.35-0.57)	1.00 (0.92-1.33)	0.009				

Intraobserver variability

Repeated intraobserver measurement data are illustrated in Figure 5. Bland-Altman analysis of the repeated measurements showed smaller agreement intervals for the isocontouring delineation method, irrespectively of the extraction method. The smallest 95% agreement interval was found for the constant extraction fraction and region

growing delineation (-0.2011–0.1857), while the largest interval was found for Gregg's extraction fraction in combination with the region growing delineation method (-0.6254–0.5945). Bias and agreement intervals from the Bland-Altman analysis of RVR values measurements are demonstrated in Supplementary Table S-5.

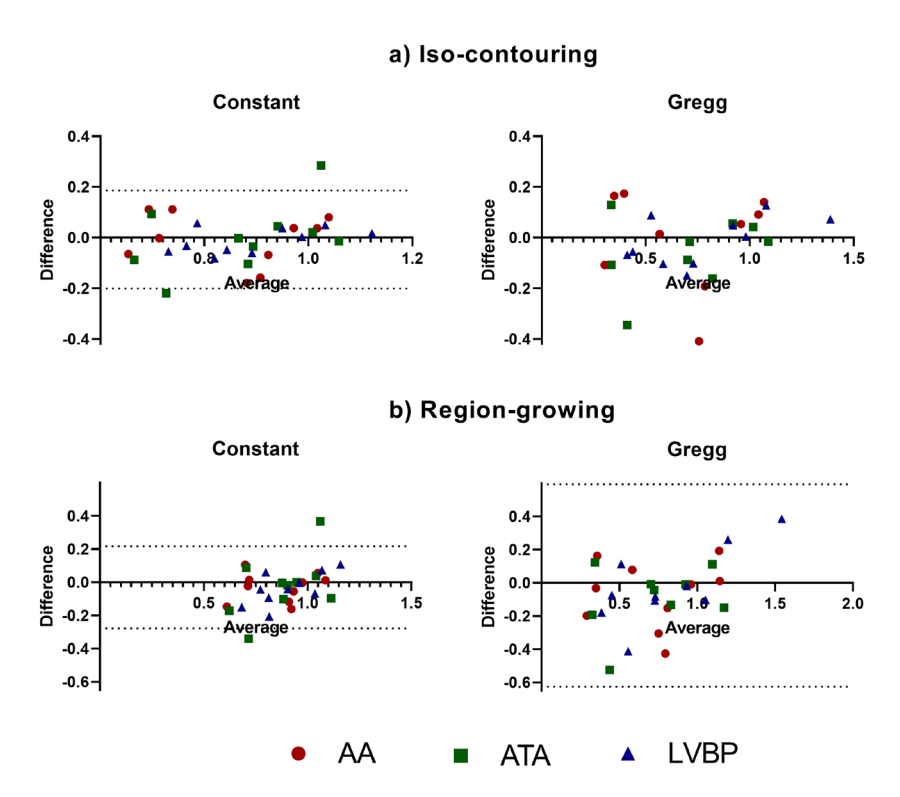


Figure 5. Bland-Altman plots of the repeated measurements of the renovascular reserve values: the ratio of renal blood flow during adenosine infusion (stress) compared to renal blood flow in rest. a) upper row denotes iso-contouring method and b) lower row denotes region growing. AA: abdominal aorta, ATA: ascending thoracic aorta and LVBP: left ventricular blood pool.

DISCUSSION

This study represents a unique exploration into the potential utilization of dynamic 82 Rb PET/CT for assessing renal perfusion. Various inputs, outputs and extraction fractions on the RBFs of an existing one-tissue compartment model were evaluated to explore the potential clinical application of 82 Rb PET/CT for assessing renal perfusion. First, K_1 values were generated with various CT-based kidney VOIs between the medulla and the cortex

(dataset A). Subsequently, myocardial perfusion data were analyzed retrospectively to obtain renal perfusion measurements in rest and when exposed to adenosine (stress) using various PET-based delineation methods, IDIFS and extraction fractions (dataset B). The RVR for the controls were overall significantly lower (p<0.05) compared to the impaired kidney function group indicating the possibility of measuring differences in kidney hemodynamics with ⁸²Rb PET/CT.

For practical reasons in subsequent analysis one single large VOI was used, even though composing K_I values for various numbers of CT-based kidney VOI delineations seemed feasible. Literature on kinetic modelling from other fields suggest that larger VOI reduces variation, which supports the use of one kidney VOI to illustrate the clinical applicability [31, 32]. Furthermore, VOI delineation was performed on unenhanced CT data obtained for attenuation purposes only (as part of the myocardial perfusion protocol for ischemia detection), limiting the ability to distinguish renal cortex and medulla. Therefore, two other PET-based kidney delineation methods were explored in the remainder of the study using dataset B.

Applying manual CT-based kidney delineations on dataset A, no significant differences were found between the total mean K, values of one, two, three and four kidney VOI placements, indicating that the mean K, values were independent of the number of VOI placements. However, significant differences in K, values between the VOIs were found applying three and four VOIs, which might indicate that distinction between the medulla and cortex was possible. Preclinical studies have shown that the medullary blood flow can be maintained when the cortical blood flow is severely decreased [3, 33]. In future studies, it might be worthwhile to incorporate a gradient of more layers between the medulla and cortex (as previously performed in MRI kidney studies [34-36]) that is adjusted to the spatial resolution of PET/CT [3]. However, applying three and four VOIs resulted in a larger SD of the mean K, values and outliers compared to the application of one VOI (Figure 3). This K, deviation might be a result of partial volume effects or manual VOI CT-delineations, but might also be explained by the heterogeneous retrospective dataset A with potentially diverse physiological renal K, values. Hypothetically, smaller VOIs are more affected by the spill-out effect of neighboring tissues, showing less 82Rb uptake of surrounded lower vascularized structures. Therefore, the optimal number of VOI delineations should be further explored in future studies that are dedicated to applying 82Rb PET/CT to the kidney.

Another possible explanation for the significant differences observed with three and four VOI placements may be attributed to the fixed $v_{\rm B}$ applied in this study. The value of 0.1 was estimated using the entire kidney of healthy subjects [13, 15], but different VOIs within the kidney might potentially have varying $v_{\rm B}$ values. However, the objective of our study was

to assess the applicability of various kidney VOIs, IDIFs and extraction fractions of a one-tissue compartment model. To achieve this, we extensively reviewed available literature and applied that in our study. Unfortunately, literature regarding $v_{\rm B}$ of the kidney and renal perfusion using imaging is currently hardly available. Consequently, further research is necessary to investigate the effects of $v_{\rm B}$ in patients with impaired kidney function and different parts of the kidney in a larger prospective study.

Reproducibility analysis of two PET-based delineation methods showed smaller agreement interval limits for iso-contouring compared to region growing kidney delineation, indicating that iso-contouring is less sensitive for repetition errors. Possible explanations are manual temporal frame selection and manual VOI adjustments, making region growing more prone for errors compared to iso-contouring (which only requires bounding box around the averaged kidney volume).

No significant difference between the region growing and iso-contouring delineations within the same vascular input was found. The LVBP and AA as IDIFs showed the least spread in the Bland-Altman plots, while the IDIF ATA showed the most outliers. Moreover, no significant differences between the IDIFs AA and LVBP with regards to RBF calculation were observed. The IDIF AA is especially interesting for measuring renovascular reserve, as this vessel would be in the scan FoV. Therefore, previous renal studies considered it as a suitable alternative to the LVBP, which we confirm in our study [12, 13]. Additionally, a high correlation was found between arterial sampling and AA as IDIF in renal studies [37]. This study supports the feasibility of the use of the AA as IDIF, possibly combined with an iso-contouring kidney delineation method.

Obtained renal K_1 values in five individuals without cardiovascular or renal disease were in line with previous reported renal K_1 values [12, 13]. However, to the best of our knowledge, the function describing the extraction of 82 Rb in the kidney and the conversion of K_1 to flow is currently unknown. Literature suggests, with a high first pass extraction, a nonlinear relationship between the flow and K_1 due to the retention of 82 Rb in tissue and the active transport into cells [38, 39]. Gregg et al. reported the relation between K_1 and flow in kidney tissue, showing that the extraction function by Gregg deflects more strongly with increasing flow [25]. Future studies comparing K_1 values obtained using 82 Rb as flow tracer with a gold standard reference radiopharmaceutical with a linear extraction such as 15 O] H_2 O, is therefore crucial in order to establish a more robust relationship between K_1 values and flow of 82 Rb in renal tissue. Moreover, it is essential to further investigate the extraction of 82 Rb in the kidney and the conversion of K_1 to flow before the clinical implementation of 82 Rb PET/CT measurements can take place.

Changes in RBF between rest and during exposure to adenosine (stress) led to renovascular reserves below 1.0 for the group consisting of individuals without cardiovascular or renal disease, while the renovascular reserves in the group of kidney patients were around 1.0. This might be a direct consequence of our pragmatic choice to use adenosine and retrospective cardiac data. Adenosine is considered a systemic vasodilatant while the spleen is also known to exhibit vasoconstriction after adenosine administration [40]. Previous research showed that adenosine has various effects on the renal perfusion [25, 28, 41-43]. Ultimately, we need a well-established renal stressor that can also be effectively combined with imaging from logistical and technical perspectives.

This study contains some limitations. First, the limited number of subjects constitutes a major limitation and hence our results should be interpreted carefully. However, little is known about the consequences of the changes in RBF, and 82Rb PET/CT data for renal perfusion imaging are scarce. Moreover, non-invasive imaging techniques for assessing renal are not incorporated in clinical practice guidelines due to the lack of evidence. Although our retrospective proof-of-concept study concerns only a small study population. we believe that our findings exhibit the complexity of assessing RBF and contribute to the knowledge of the application of 82Rb PET/CT for kidney perfusion imaging. Second, the study is retrospective in design and used cardiac 82Rb PET/CT data to evaluate the feasibility to assess renal perfusion. As such, the used scan data in the present study was obtained focused on myocardial ischemia detection, with the heart in the center of the FoV, yielding the highest sensitivity [44]. As a result, some parts of the kidney were imaged at the edge of the FoV with lower sensitivity, leading to poorer image quality for the kidney. In addition, adenosine was used as a pharmacological stress agent, however this is not the ideal 'stress agent' for the kidney compared to infusion of amino acids, dopamine or an acute protein. Langaa et al. has pioneered the use combining 82Rb PET/ CT with infusion of amino acids, demonstrating an increase in RBF in healthy volunteers [6]. Future prospective studies should focus on developing a dedicated kidney protocol for 82Rb PET/CT, where both kidneys are centered in the FoV to evaluate various parts of the kidney, applying a renal stress agent, and further explore kinetic modelling with its inputs, outputs and extraction fractions to evaluate disease activity and treatment response for CKD.

CKD is recognized as one of the leading causes of death worldwide [45-47]. In early-stage CKD, patients are often asymptomatic, leading to a diagnosis in later stages when substantial and irreversible kidney damage has already occurred. Given the asymptomatic nature of early-stage CKD, there is a need for a novel diagnostic tool or biomarker to enable early treatment, potentially slowing progression, while being cost effective [48, 49]. Current clinically available non-invasive imaging techniques for assessing the kidney

function or hemodynamics as renal scintigraphy, CT, magnetic resonance imaging (MRI) and ultrasound have drawbacks including limited resolution, observer dependency, scan duration, limited quantification possibilities and the use of contrast agents that may induce nephrotoxicity and allergic reactions [50-52].

The scarcity of evidence demonstrating heightened renal hypoxia in humans is mainly attributed to the absence of non-invasive (imaging) techniques for assessing renal oxygenation and fibrosis [53]. However, changes in renal microcirculation are crucial in the pathophysiological processes of renal disease [54]. Given the limited availability of literature in the field of kidney perfusion and various physiological and anatomical similarities among the perfusion of the heart and the kidneys, we found it worthwhile to investigate whether dynamic ⁸²Rb PET/CT was able to detect differences in renal hemodynamics in stress conditions compared to resting state (RVR). Moreover, the coronary flow reserve has been proven to be of added value and has been used in a routine clinical setting for the detection of myocardial ischemia [10, 55]. Therefore, ⁸²Rb PET/CT holds potential relevance as an accessible novel diagnostic tool for the early detection of CKD by assessing renal hemodynamics.

CONCLUSION

In this study, it was demonstrated that obtaining renal K_1 and RBF values using ⁸²Rb PET/CT was feasible using a one-tissue compartment model applying either CT- or PET-based kidney VOI delineation methods (region growing and iso-contouring), IDIFs (AA, ATA and LVBP) and Gregg's [25] and constant [7] extraction fractions. Applying iso-contouring as the PET-based VOI of the kidney and using AA as an IDIF is suggested for consideration in further studies. Moreover, it is crucial to further investigate the extraction of ⁸²Rb in the kidney and the conversion of K_1 to flow before the clinical implementation of ⁸²Rb PET/CT measurements can take place. Dynamic ⁸²Rb PET/CT imaging showed significant differences in renal hemodynamics in rest compared to when exposed to adenosine. This indicates that dynamic ⁸²Rb PET/CT has potential to detect differences in renal hemodynamics in stress conditions compared to the resting state, and might be useful as a novel diagnostic tool for assessing renal perfusion.

REFERENCES

- Bello AK, Levin A, Tonelli M, Okpechi IG, Feehally J, Harris D, et al. Assessment of global kidney health care status. Jama. 2017;317:1864-81.
- Stack AG, Casserly LF, Cronin CJ, Chernenko T, Cullen W, Hannigan A, et al. Prevalence and variation of Chronic Kidney Disease in the Irish health system: initial findings from the National Kidney Disease Surveillance Programme. BMC nephrology. 2014;15:1-12.
- Päivärinta J, Anastasiou IA, Koivuviita N, Sharma K, Nuutila P, Ferrannini E, et al. Renal Perfusion, Oxygenation and Metabolism: The Role of Imaging. Journal of Clinical Medicine. 2023;12:5141.
- Amoabeng KA, Laurila S, Juárez-Orozco LE, Marthinsen ABL, Moczulski D, Rebelos E, et al. The utilization of positron emission tomography in the evaluation of renal health and disease. Clinical and Translational Imaging. 2022:1-11.
- Palsson R, Waikar SS. Renal Functional Reserve Revisited. Adv Chronic Kidney Dis. 2018;25:e1e8. doi:10.1053/j.ackd.2018.03.001.
- Langaa SS, Mose FH, Fynbo CA, Theil J, Bech JN. Reliability of rubidium-82 PET/CT for renal perfusion determination in healthy subjects. BMC nephrology. 2022;23:1-10.
- Mullani N, Ekas R, Marani S, Kim E, Gould K. Feasibility of measuring first pass extraction and flow with rubidium-82 in the kidneys. American journal of physiologic imaging. 1990;5:133-40.
- 8. Koopman M, Koomen G, Krediet R, De Moor E, Hoek F, Arisz L. Circadian rhythm of glomerular filtration rate in normal individuals. Clinical science (London, England: 1979). 1989;77:105-11.
- Eckerbom P, Hansell P, Cox E, Buchanan C, Weis J, Palm F, et al. Circadian variation in renal blood flow and kidney function in healthy volunteers monitored with noninvasive magnetic resonance imaging. American Journal of Physiology-Renal Physiology. 2020;319(6):F966-F978.
- Ziadi MC. Myocardial flow reserve (MFR) with positron emission tomography (PET)/computed tomography (CT): clinical impact in diagnosis and prognosis. Cardiovasc Diagn Ther. 2017;7:206-18. doi:10.21037/cdt.2017.04.10.
- Lortie M, Beanlands RS, Yoshinaga K, Klein R, Dasilva JN, DeKemp RA. Quantification of myocardial blood flow with 82Rb dynamic PET imaging. Eur J Nucl Med Mol Imaging. 2007;34:1765-74. doi:10.1007/s00259-007-0478-2.
- Tahari AK, Bravo PE, Rahmim A, Bengel FM, Szabo Z. Initial human experience with Rubidium-82 renal PET/CT imaging. J Med Imaging Radiat Oncol. 2014;58:25-31. doi:10.1111/1754-9485.12079.
- Langaa SS, Lauridsen TG, Mose FH, Fynbo CA, Theil J, Bech JN. Estimation of renal perfusion based on measurement of rubidium-82 clearance by PET/CT scanning in healthy subjects. EJNMMI Phys. 2021;8:43. doi:10.1186/s40658-021-00389-0.
- Levey AS, Coresh J, Balk E, Kausz AT, Levin A, Steffes MW, et al. National Kidney Foundation practice guidelines for chronic kidney disease: evaluation, classification, and stratification. Annals of internal medicine. 2003;139:137-47.
- Effros RM, Lowenstein J, Baldwin DS, Chinard FP. Vascular and extravascular volumes of the kidney of man. Circ Res. 1967;20:162-73. doi:10.1161/01.res.20.2.162.
- 16. PMOD Kinetic Modeling User Manual. English. Version 4.4: 1996-2022; 2022 Nov 9
- Buchert R, Carson RE, Gunn RN, van den Hoff J, Innis RB, Moos Knudsen G, et al. PET Pharmacokinetic Course manual, Shanghai, China. In. 1999.
- Baron J, Frackowiak R, Herholz K, Jones T, Lammertsma A, Mazoyer B, et al. Use of PET methods for measurement of cerebral energy metabolism and hemodynamics in cerebrovascular disease. Journal of Cerebral Blood Flow & Metabolism. 1989;9:723-42.

- Herscovitch P, Markham J, Raichle M. Brain Blood Flow Measured with Intravenous H215O.: I. Theory and Error Analysis. Journal of Nuclear Medicine. 1983;24:782-9.
- Meyer E. Simultaneous correction for tracer arrival delay and dispersion in CBF measurements by the H215O autoradiographic method and dynamic PET. Journal of nuclear medicine. 1989:30:1069-78.
- Pan T, Einstein SA, Kappadath SC, Grogg KS, Lois Gomez C, Alessio AM, et al. Performance evaluation of the 5-Ring GE Discovery MI PET/CT system using the national electrical manufacturers association NU 2-2012 Standard. Medical Physics. 2019;46:3025-33. doi:https:// doi.org/10.1002/mp.13576.
- Bettinardi V, Castiglioni I, De Bernardi E, Gilardi MC. PET quantification: strategies for partial volume correction. Clinical and Translational Imaging. 2014;2:199-218. doi:10.1007/s40336-014-0066-v.
- 23. Renkin EM. Transport of potassium-42 from blood to tissue in isolated mammalian skeletal muscles. Am J Physiol. 1959;197:1205-10. doi:10.1152/ajplegacy.1959.197.6.1205.
- Crone C. The Permeability of Capillaries in Various Organs as Determined by Use of the 'Indicator Diffusion' Method. Acta Physiol Scand. 1963;58:292-305. doi:10.1111/j.1748-1716.1963.tb02652.x.
- 25. Gregg S, Keramida G, Peters AM. (82) Rb tissue kinetics in humans. Clin Physiol Funct Imaging. 2021;41:245-52. doi:10.1111/cpf.12691.
- Staanum PF, Frellsen AF, Olesen ML, Iversen P, Arveschoug AK. Practical kidney dosimetry in peptide receptor radionuclide therapy using [(177)Lu]Lu-DOTATOC and [(177)Lu]Lu-DOTATATE with focus on uncertainty estimates. EJNMMI Phys. 2021;8:78. doi:10.1186/s40658-021-00422-2.
- 27. Bouchet LG, Bolch WE, Blanco HP, Wessels BW, Siegel JA, Rajon DA, et al. MIRD Pamphlet No 19: absorbed fractions and radionuclide S values for six age-dependent multiregion models of the kidney. J Nucl Med. 2003;44:1113-47.
- 28. Hansen PB, Schnermann J. Vasoconstrictor and vasodilator effects of adenosine in the kidney. Am J Physiol Renal Physiol. 2003;285:F590-9. doi:10.1152/ajprenal.00051.2003.
- 29. Wierema TK, Houben AJ, Kroon AA, Postma CT, Koster D, van Engelshoven JM, et al. Mechanisms of adenosine-induced renal vasodilatation in hypertensive patients. J Hypertens. 2005;23:1731-6. doi:10.1097/01.hjh.0000180160.89264.9d.
- Virtanen P, Gommers R, Oliphant TE, Haberland M, Reddy T, Cournapeau D, et al. SciPy 1.0: fundamental algorithms for scientific computing in Python. Nature Methods. 2020;17:261-72. doi:10.1038/s41592-019-0686-2.
- van der Weerdt AP, Klein LJ, Boellaard R, Visser CA, Visser FC, Lammertsma AA. Imagederived input functions for determination of MRGlu in cardiac (18)F-FDG PET scans. J Nucl Med. 2001;42:1622-9.
- de Geus-Oei LF, Visser EP, Krabbe PF, van Hoorn BA, Koenders EB, Willemsen AT, et al. Comparison of image-derived and arterial input functions for estimating the rate of glucose metabolism in therapy-monitoring 18F-FDG PET studies. J Nucl Med. 2006;47:945-9.
- 33. Trueta J, Barclay AE. Studies of the renal circulation. Bristol Med Chir J. 1947;(1883).; 1947; 65(233):16-8.
- Pruijm M, Milani B, Pivin E, Podhajska A, Vogt B, Stuber M, et al. Reduced cortical oxygenation predicts a progressive decline of renal function in patients with chronic kidney disease. Kidney international. 2018;93:932-40.
- 35. Li LP, Tan H, Thacker JM, Li W, Zhou Y, Kohn O, et al. Evaluation of Renal Blood Flow in Chronic Kidney Disease Using Arterial Spin Labeling Perfusion Magnetic Resonance Imaging. Kidney Int Rep. 2017;2:36-43. doi:10.1016/j.ekir.2016.09.003.

- Milani B, Ansaloni A, Sousa-Guimaraes S, Vakilzadeh N, Piskunowicz M, Vogt B, et al. Reduction
 of cortical oxygenation in chronic kidney disease: evidence obtained with a new analysis method
 of blood oxygenation level-dependent magnetic resonance imaging. Nephrology Dialysis
 Transplantation. 2017;32:2097-105.
- Germano G, Chen BC, Huang SC, Gambhir SS, Hoffman EJ, Phelps ME. Use of the abdominal aorta for arterial input function determination in hepatic and renal PET studies. J Nucl Med. 1992;33:613-20.
- 38. Szabo Z, Xia J, Mathews WB, Brown PR. Future direction of renal positron emission tomography. Semin Nucl Med. 2006;36:36-50. doi:10.1053/j.semnuclmed.2005.08.003.
- Tamaki N, Rabito CA, Alpert NM, Yasuda T, Correia JA, Barlai-Kovach M, et al. Serial analysis of renal blood flow by positron tomography with rubidium-82. Am J Physiol. 1986;251:H1024-30. doi:10.1152/ajpheart.1986.251.5.H1024.
- 40. Manisty C, Ripley DP, Herrey AS, Captur G, Wong TC, Petersen SE, et al. Splenic Switch-off: A Tool to Assess Stress Adequacy in Adenosine Perfusion Cardiac MR Imaging. Radiology. 2015;276:732-40. doi:10.1148/radiol.2015142059.
- 41. Vallon V, Osswald H. Adenosine receptors and the kidney. Handb Exp Pharmacol. 2009:443-70. doi:10.1007/978-3-540-89615-9_15.
- Bidani AK, Polichnowski AJ, Loutzenhiser R, Griffin KA. Renal microvascular dysfunction, hypertension and CKD progression. Curr Opin Nephrol Hypertens. 2013;22:1-9. doi:10.1097/ MNH.0b013e32835b36c1.
- 43. Oyarzun C, Garrido W, Alarcon S, Yanez A, Sobrevia L, Quezada C, et al. Adenosine contribution to normal renal physiology and chronic kidney disease. Mol Aspects Med. 2017;55:75-89. doi:10.1016/j.mam.2017.01.004.
- 44. Pan T, Einstein SA, Kappadath SC, Grogg KS, Lois Gomez C, Alessio AM, et al. Performance evaluation of the 5-Ring GE Discovery MI PET/CT system using the national electrical manufacturers association NU 2-2012 Standard. Med Phys. 2019;46:3025-33. doi:10.1002/ mp.13576.
- Jager KJ, Kovesdy C, Langham R, Rosenberg M, Jha V, Zoccali C. A single number for advocacy and communication-worldwide more than 850 million individuals have kidney diseases. Kidney Int. 2019;96:1048-50. doi:10.1016/j.kint.2019.07.012.
- 46. Kovesdy CP. Epidemiology of chronic kidney disease: an update 2022. Kidney Int Suppl (2011). 2022;12:7-11. doi:10.1016/j.kisu.2021.11.003.
- Tonelli M, Wiebe N, Culleton B, House A, Rabbat C, Fok M, et al. Chronic kidney disease and mortality risk: a systematic review. Journal of the American Society of Nephrology: JASN. 2006;17:2034-47. doi:10.1681/ASN.2005101085.
- 48. Black C, Sharma P, Scotland G, McCullough K, McGurn D, Robertson L, et al. Early referral strategies for management of people with markers of renal disease: a systematic review of the evidence of clinical effectiveness, cost-effectiveness and economic analysis. Health Technol Assess. 2010;14:1-184. doi:10.3310/hta14210.
- Tonelli M, Dickinson JA. Early Detection of CKD: Implications for Low-Income, Middle-Income, and High-Income Countries. Journal of the American Society of Nephrology: JASN. 2020;31:1931-40. doi:10.1681/ASN.2020030277.
- 50. Andreucci M, Solomon R, Tasanarong A. Side effects of radiographic contrast media: pathogenesis, risk factors, and prevention. BioMed research international. 2014;2014.

- 51. Rydahl C, Thomsen HS, Marckmann P. High prevalence of nephrogenic systemic fibrosis in chronic renal failure patients exposed to gadodiamide, a gadolinium-containing magnetic resonance contrast agent. Investigative radiology. 2008;43:141-4.
- 52. Kishimoto N, Mori Y, Nishiue T, Nose A, Kijima Y, Tokoro T, et al. Ultrasound evaluation of valsartan therapy for renal cortical perfusion. Hypertension Research. 2004;27:345-9.
- 53. Fine LG, Norman JT. Chronic hypoxia as a mechanism of progression of chronic kidney diseases: from hypothesis to novel therapeutics. Kidney international. 2008;74:867-72.
- Alhummiany B, Sharma K, Buckley DL, Soe KK, Sourbron SP. Physiological confounders of renal blood flow measurement. Magnetic Resonance Materials in Physics, Biology and Medicine. 2023;1-18.
- 55. Ziadi MC, Dekemp RA, Williams KA, Guo A, Chow BJ, Renaud JM, et al. Impaired myocardial flow reserve on rubidium-82 positron emission tomography imaging predicts adverse outcomes in patients assessed for myocardial ischemia. Journal of the American College of Cardiology. 2011;58:740-8.



CHAPTER 3

Investigating the potential added value of [18F]FDG-PET/CT in long COVID patients with persistent symptoms: a proof of concept study

Authors

L. L. Chen*, A. van de Burgt*, F. Smit , R.S. Audhoe,

S.M. de Boer, F.H.P. van Velden and L.F. de Geus-Oei

* L. L. Chen and A. van de Burgt contributed equally to this work and share first authorship.

Published

Nuclear Medicine Communications, 2023; 44(6): 495-501,

DOI: 10.1097/MNM.000000000001689

Supplementary materials

https://doi.org/10.1097/MNM.000000000001689

ABSTRACT

Objective

Since the end of 2019, the SARS-CoV-2 virus has infected millions of people, of whom a significant group suffers from sequelae from coronavirus disease (COVID-19), termed long COVID. As more and more patients emerge with long COVID who have symptoms of fatigue, myalgia and joint pain, we must examine potential biomarkers to find quantifiable parameters to define the underlying mechanisms and enable response monitoring. The aim of this study is to investigate the potential added value of [18F]FDG-PET/CT for this group of long COVID patients.

Methods

For this proof of concept study, we evaluated [18F]FDG-PET/CT scans of long COVID patients and controls. Two analyses were performed: semi-quantitative analysis using target-to-background ratios (TBR) in 24 targets and total vascular score (TVS) assessed by two independent nuclear medicine physicians. Mann-Whitney U-test was performed to find significant differences between the two groups.

Results

13 patients were included in the long COVID group and 25 patients were included in the control group. No significant differences (p < 0.05) were found between the long COVID group and the control group in the TBR or TVS assessment.

Conclusion

As we found no quantitative difference in the TBR or TVS between long COVID patients and controls, we are unable to prove that [18F]FDG is of added value for long COVID patients with symptoms of myalgia or joint pain. Prospective cohort studies are necessary to understand the underlying mechanisms of long COVID.

Keywords

inflammation, infection, vasculitis, SARS-CoV-2, imaging

INTRODUCTION

Since the end of 2019, the severe acute respiratory syndrome coronavirus 2 (SARS-CoV-2) virus has been disrupting lives globally despite extensive efforts to contain the virus [1]. The most common symptoms of acute coronavirus disease 2019 (COVID-19) are fever, dry cough and fatigue, albeit the disease expression is highly heterogeneous [1–4]. About 80% of the patients experience mild to moderate disease, whilst 5% develop critical illness [5,6]. Moreover, the majority of patients develop sequelae after recovering from the acute SARS-CoV-2 infection that lasts for weeks to months [7]. This is called long COVID, or post-COVID syndrome [6,8,9]. Symptoms associated with long COVID include fatigue, dyspnea, poor memory, hair loss, joint pain, attention disorder and myalgia, although this disease expression is also heterogeneous [4,10]. The onset of arthritis and vasculitis has also been reported in long COVID patients, and there is a growing recognition that COVID-19 is a vascular disease that leads to an escalating cascade of inflammatory pathways [11–14].

Long COVID patients are often PCR-negative and show no radiological or biochemical abnormalities. The lag of clinical recovery can be exasperating, which causes mental problems on top of the physical problems [6]. As the primary focus of the pandemic was to investigate the optimal treatment for acute COVID-19 patients and deal with the latest mutations of SARS-CoV-2, optimizing the rehabilitation of long COVID patients lagged. As a result, clear guidelines on the optimal treatment for long COVID patients are lacking [4].

As more and more patients with COVID in the medical history are emerging with vague symptoms, e.g. fatigue, joint pain and myalgia similar to vasculitis, sarcoidosis and polymyalgia rheumatica (PMR), there is a need for (imaging) biomarkers to find quantifiable parameters in order to define the underlying mechanisms. As a result, this would enable evaluation of disease activity and treatment response monitoring. 18-F-2-fluoro-2-deoxyglucose ([¹8F]FDG) positron emission tomography/computed tomography (PET/CT) can potentially be of added value in this process, as [¹8F]FDG-PET/CT is able to determine localized metabolic activity, including infection, inflammation and malignancies [15]. Abnormal [¹8F]FDG-PET/CT scans in long COVID patients have been observed in earlier studies, albeit no study has been able to discern a typical visual [¹8F]FDG-uptake pattern in long COVID patients yet, which shows the need for further investigation [16–18]. This study aims to investigate the potential added value of [¹8F]FDG-PET/CT for long COVID patients with persistent symptoms such as myalgia, joint pain and fatigue, reminiscent of vasculitis, sarcoidosis and PMR.

METHODS

Study design and population

To investigate the potential added value of [18F]FDG-PET/CT for long COVID patients with persistent symptoms, we performed a retrospective proof of concept study to qualitatively and quantitatively compare [18F]FDG-PET/CT scans of long COVID patients and controls.

For the long COVID patient group, we included patients from our long COVID outpatient clinic who presented with symptoms of myalgia or joint pain, reminiscent of vasculitis, PMR or sarcoidosis, for whom an [18F]FDG-PET/CT scan was performed between May 2021 and October 2021. This study was retrospective and approval by the medical ethics committee was therefore not required according to the Dutch law. Nevertheless, written informed consent was obtained from all participants.

For the control group, we included patients who either i) had a malignancy in the past for which they were exclusively surgically curatively treated and for whom a routine [18F] FDG-PET/CT follow-up scan was performed, excluding recurrent/residual disease; or ii) received an [18F]FDG-PET/CT scan for a suspected malignancy or etiology of unknown origin, which did not show any disease. Moreover, we exclusively included [18F]FDG-PET/CT scans from June 2019 until October 2021, as the hospital acquired a new PET/CT scanner in June 2019. We did not include patients in the control group who had received systemic oncological treatment or radiotherapy in the past or had inflammatory diseases such as sarcoidosis, vasculitis, rheumatic diseases or COVID-19 in their medical history.

Baseline information was gathered from the electronic health records consisting of sex, age, BMI, pre-PET glycaemia, administered [18 F]FDG activity, interval time between [18 F]FDG administration and scan acquisition, and medicine use. Differences in age, BMI, pre-PET glycaemia, administered [18 F]FDG activity and interval time between [18 F]FDG administration and scan acquisition were investigated with an unpaired two-tailed Student's t-test and differences in sex using a Chi-squared test. We considered p < 0.05 to be significant.

Data collection

We anonymized patient data and recorded these in a database. Whole-body [¹⁸F]FDG-PET/CT was performed for long COVID patients on the 5-Ring Discovery MI PET/CT (GE Healthcare, Chicago, IL, USA) [19]. Control [¹⁸F]FDG-PET/CT scans were acquired as whole-body images if available and as torso (mid-thigh to skull base) images if no whole-body images were available. Data acquisition was performed approximately 60 min after intravenous [¹⁸F]FDG administration (1.5 MBq per kilogram bodyweight if BMI < 30, 2.1 MBq per kilogram bodyweight if BMI > 30). Of note, due to use of a highly sensitive

PET/CT system this dose is lower than the standard 3.0 MBq per kilogram bodyweight. An emission scan was obtained using multiple bed positions (50% overlap between bed positions, 75 sec per bed position) [19]. Time-of-flight PET data were reconstructed using the point spread function and CT-based attenuation correction (120 kV, smart mA modulations with a noise index of 49.5 and an mA ranging from 15 to 550, 0.5 sec rotation time). Body-weighted standardized uptake values (SUV) were obtained using Sectra IDS7 (Sectra AB, Linköping, Sweden) (PACS).

Data analysis

To compare long COVID patients with controls, a semi-quantitative analysis was performed by determining the target-to-background ratio (TBR) according to the nine research targets described in the European Association for Nuclear Medicine (EANM) recommendations for [18F]FDG-PET/CT imaging in large vessel vasculitis (LVV) and PMR to account for the variability of SUV values: the carotid, subclavian, axillary, vertebral, and pulmonary arteries, the ascending, descending, and abdominal aorta, and the aortic arch [20–23]. Additional targets consisted of the parotid glands, external iliac arteries, femoral arteries, tibial arteries, the liver and the brachioradialis muscle. The background was calculated as the average SUV in the vena cava inferior and vena cava superior (figure 1).

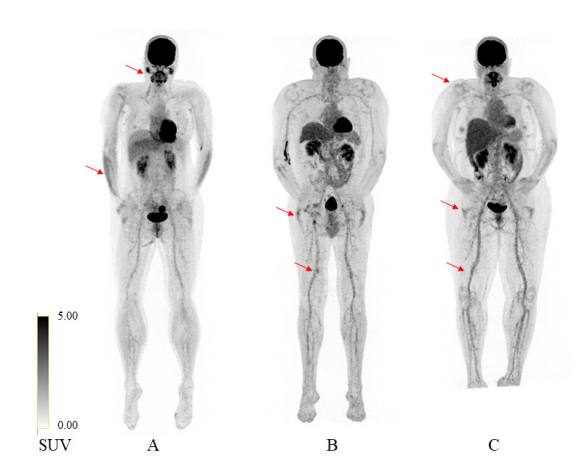


Figure 1. Examples of three long COVID patients with persistent symptoms of fatigue, myalgia or joint pain. (A) High to moderate [18F]FDG-uptake in the m. brachioradialis and parotid glands (red arrows). (B and C) Low to moderate [18F]FDG-uptake in joints and vessels in the lower extremities (red arrows).

In order to assess the difference in overall [18F]FDG-uptake between the long COVID group and control group, we used the total vascular score (TVS), as this takes heterogeneity within groups into account. The TVS was determined using the seven clinical targets

described in the EANM recommendations for [¹8F]FDG-PET/CT imaging in LVV and PMR: thoracic aorta, abdominal aorta, subclavian arteries, axillary arteries, carotid arteries, iliac arteries and femoral arteries [22]. Additional targets consisted of the parotid glands, shoulder girdle, and hip girdle (analysis of 10 targets, performed on all patients). Additionally, the tibial arteries, lower arm muscles and hands were assessed if visible on the scan (analysis of 13 targets, performed on patients with total body scans). A standardized 0-to-3 grading system was used to assess all targets, and was defined as follows: 0 = physiological [¹8F]FDG-uptake; 1 = minimally heightened [¹8F]FDG-uptake (< mediastinum), 2 = clearly increased [¹8F]FDG-uptake (≥ mediastinum and < liver), 3 = very marked [¹8F]FDG-uptake (≥ liver). The ten or thirteen targets per patient were assessed independently by two experienced nuclear medicine physicians (SB, RA) who were blinded. The TVS was calculated as the sum of all target scores.

Statistical analysis

For the semi-quantitative analysis, the mean, median, standard deviation and range were calculated for every TBR and subject (Supplementary table A). We performed the Mann-Whitney U-test to assess the difference between the long COVID group and control group for each target and applied Bonferroni correction for multiple testing [24]. We considered a p-value < 0.05 to be statistically significant.

For the TVS analysis, the interclass correlation (ICC) was determined to assess intraobserver similarity. A threshold of ICC < 0.75 was agreed upon to analyze the two observers separately. A separate Mann-Whitney U test was performed for all subjects using ten targets (maximum number of subjects) and subjects with thirteen targets (maximum number of targets). We considered a p-value < 0.05 to be statistically significant. We used Excel (Version 2109; Microsoft, Albuquerque, NM, USA) for data collection and Matlab (version R2019b; MathWorks, Natick, MA, USA) to perform the statistical tests.

RESULTS

Patient characteristics

13 patients were included in the long COVID group and 25 patients were included in the control group (follow-up after melanoma n=10, disproved suspicion of malignancy n=8, follow-up after mammary carcinoma n=2, follow-up after colon carcinoma n=2, other indications n=3). The long COVID group was on average significantly younger than the control group (47.2 \pm 13.09 versus 58 \pm 15.62, respectively, p = 0.017) and consisted of less males (38.5% versus 46.2%, respectively, p = 0.010). Table 1 summarizes the baseline characteristics of both groups.

[18F]FDG PET/CT parameters

We found no significant differences between the long COVID and control group with regards to pre-PET glycaemia (5.33 \pm 1.31 versus 5.96 \pm 1.91 mmol/L, p = 0.23), administered [18 F]FDG activity (123.87 \pm 34.35 versus 132.93 \pm 38.46 MBq, p = 0.58) and interval time between [18 F]FDG injection and image acquisition (51.38 \pm 8.49 [range 41-74] versus 48.52 \pm 5.96 [range 40-68] minutes, p = 0.44) (Table 1).

Clinical data

Long COVID patients in this study reported symptoms of fatigue, dyspnea, concentration problems, myalgia, asthenia, and low mood. The severity of the COVID-19 infection ranged from mild to severe. Symptoms during infection included fatigue, dyspnea, cough, fever, myalgia, and loss of taste or smell. The time interval between COVID-19 infection and [18 F]FDG-PET/CT scan was 9.0 \pm 4.4 months. None of the 13 long COVID patients were admitted to the hospital for the COVID-19 infection.

TBR [18F]FDG-PET/CT analysis

Table 2 shows the results of the semi-quantitative analysis of all targets. No targets differed significantly between the long COVID group compared to the control group. Increased [18 F]FDG-uptake of the parotid glands was observed in 6/13 long COVID patients and 6/26 control patients (TBR $_{parotid}$ gland left = 1.34 versus 1.02, respectively, p = 5.52 and TBR $_{parotid}$ gland right = 1.37 versus 1.01, respectively, p = 3.35). We also observed a higher [18 F]FDG-uptake in the liver in the long COVID group than in the control group (TBR $_{liver}$ = 1.47 versus 1.34, respectively, p = 0.18).

Table 1. Baseline subject characteristics.

	Long COVID (n=13)	Controls (n=25)	p-value
Gender (male, %)	5 (38.5%)	11 (44%)	0.016
Age (mean, std, yr)	47.2 (13.09)	57.3 (15.5)	0.024
BMI status (mean, std, kg/m²)	24.11 (4.09)	24.62 (3.89)	0.89
Pre-PET glycaemia (mmol/L)	5.33 (1.31)	5.96 (1.91)	0.23
Administered [18F]FDG activity (MBq)	123.87 (34.35)	132.93 (38.46)	0.58
interval time between [18F]FDG injection and image acquisition (min)	51.38 (8.49)	48.52 (5.96)	0.44
Symptoms			
Fatigue	13	0	
Pain	6	0	
Dyspnoea	4	0	
Loss of strength	3	0	

Table 1. Baseline subject characteristics. (continued)

	Long COVID (n=13)	Controls (n=25)	p-value	
Comorbidities (n)				
No	2	4		
Diabetes	1	5		
Hypertension	2	2		
Chronic respiratory disease	3	4		
Concomitant medications (n)				
None	5	9		
Beta-blockers	0	4		
Calcium antagonists	0	3		
Sartans	0	1		
ACE inhibitors	1	2		
Diuretics	0	1		
Oral anticoagulants	1	2		
Antiplatelet drugs	0	1		
Hypoglycaemic drugs	1	3		
Corticosteroids	2	3		
Statins	1	4		
NSAIDs	3	3		
Benzodiazepines	1	2		
Proton pump inhibitors	4	5		
Bronchodilators	2	2		

BMI = body mass index; ACE = angiotensin-converting enzyme; NSAIDs = non-steroidal anti-inflammatory drugs.

Table 2. Results of semi-quantitative analysis in the long COVID group and control group.

	TBR mean (std)						
	Long COVID (n=13)	Controls (n=25)	p-value				
a. carotis communis sinistra (mean, std)	1.06 (0.16)	0.99 (0.25)	4.97				
a. carotis communis dextra	1.04 (0.18)	1.03 (0.18)	21.07				
a. subclavia sinistra	0.91 (0.16)	0.94 (0.15)	11.50				
a. subclavia dextra	0.92 (0.18)	0.98 (0.22)	5.24				
a. axillaris sinistra	0.88 (0.29)	0.92 (0.12)	16.00				
a. axillaris dextra	0.79 (0.30)	0.94 (0.15)	0.87				
a. vertebralis sinistra	0.90 (0.17)	0.85 (0.15)	8.54				
a. vertebralis dextra	0.86 (0.18)	0.87 (0.23)	24.00				
Ascending aorta	1.10 (0.08)	1.06 (0.06)	8.35				
Aortic arch	1.07 (0.08)	1.06 (0.11)	17.09				
Pulmonary arteries	1.09 (0.11)	1.08 (0.08)	6.76				
Descending aorta	1.06 (0.07)	1.07 (0.09)	23.12				
Abdominal aorta	1.10 (0.19)	1.09 (0.12)	16.00				
Glandula parotis sinistra	1.34 (0.75)	1.02 (0.41)	5.52				
Glandula parotis dextra	1.37 (0.78)	1.01 (0.43)	3.35				
a. iliaca externa sinistra	1.03 (0.24)	1.04 (0.19)	13.41				
a. iliaca externa dextra	0.95 (0.22)	1.05 (0.16)	3.35				
a. femoralis sinistra	1.04 (0.25)	0.93 (0.19)	9.75				
a. femoralis dextra	1.00 (0.20)	0.98 (0.26)	18.20				
a. tibialis sinistra	1.02 (0.29)	0.93 (0.15)	13.50				
a. tibialis dextra	0.99 (0.29)	0.96 (0.18)	11.69				
Liver	1.47 (0.12)	1.34 (0.11)	0.18				
m. brachioradialis sinistra	0.49 (0.14)	0.48 (0.23)	14.59				
m. brachioradialis dextra	0.49 (0.16)	0.47 (0.11)	18.20				

TBR = target to background ratio.

TVS [18F]FDG-PET/CT analysis

Moderate agreement was obtained between the two observers (ICC = 0.65, p < 0.001), meaning we performed separate analyses for the two observers (figure 2). We found a mean TVS of 3.00 ± 2.42 (observer 1) and 4.46 ± 2.07 (observer 2) in the long COVID group versus 3.60 ± 2.45 (observer 1) and 5.12 ± 2.62 (observer 2) in the control group in the analysis of ten targets (long COVID group n = 13, control group n = 25), as is shown in table 3. No observer

reported a significant difference between the two groups (p=0.53 and p=0.52, respectively). We found a mean TVS of 8 ± 4.42 (observer 1) and 7.08 ± 3.66 (observer 2) in the long COVID group versus 9.56 ± 2.24 (observer 1) and 6.78 ± 3.35 (observer 2) in the control group in the analysis of thirteen targets (long COVID group n = 13, control group n = 9), as is shown in table 4. This yielded no significant differences for both observers (p = 0.37 and p = 0.92).

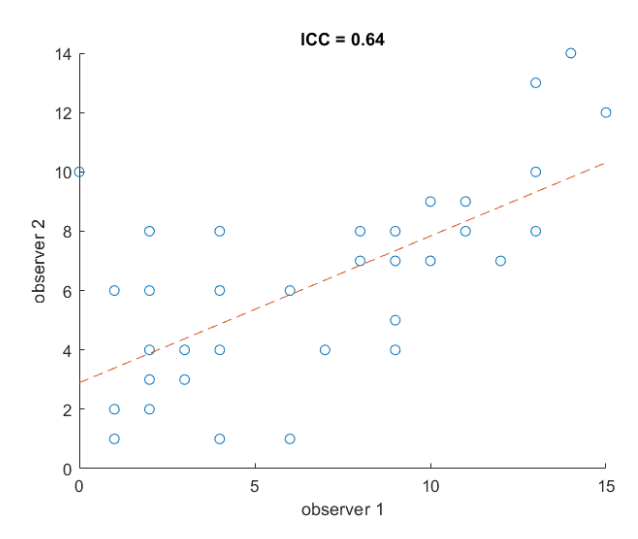


Figure 2. Scatterplot of TVS between the two observers. TVS = total vascular score, ICC = intraclass correlation coefficient.

Table 3. Total Vascular Score (TVS) in the long COVID group (n = 13) and control group (n = 26), 10 targets.

	TVS mean (std)						
	Observer 1	Observer 2					
TVS long COVID group	3 (2.42)	4.46 (2.07)					
TVS control group	3.60 (2.45)	5.12 (2.62)					
p-value	0.53	0.52					

Table 4. Total Vascular Score (TVS) in the long COVID group (n = 13) and control group (n = 9), 13 targets.

	TVS mean (std)						
	Observer 1	Observer 2					
TVS long COVID	8.00 (4.42)	7.08 (3.66)					
TVS control group	9.56 (2.24)	6.78 (3.35)					
p-value	0.37	0.47					

DISCUSSION

In this proof of concept study, we investigated the potential added value of [18F]FDG-PET/CT for long COVID patients with persistent symptoms. No significant differences were found between the long COVID group and the control group in the semi-qualitative analysis and TVS. However, although several long COVID patients showed higher uptake in one or more of these targets, we were unable to identify a general pattern.

In a similar study performed by Sollini et al., a significant difference was found between the long COVID group and the control group in several targets, including the right femoral artery, the ascending aorta, aortic arch and the descending aorta [16]. However, no correction for multiple testing was performed and if applied, no significant differences would have been found. In the current study, the Bonferroni correction for multiple testing was used to prevent false positive findings [25]. If no Bonferroni correction had been applied, we would have found significant differences in the liver and the right axillary arteries between the long COVID group and control group (Supplementary table A), which illustrates the similarity of results between Sollini et al. and the current study.

However, it should be noted that long COVID presentation could be heterogeneous in nature, as other rheumatic diseases such as PMR also show high heterogeneity across patients on [18F]FDG-PET/CT scans [26,27]. Furthermore, similar studies also found heterogeneous differences between long COVID patients and controls [28,29].

The liver has been reported as COVID-19 target organ [30,31] and recent studies suggest that the liver might be still inflamed in long COVID [29,32]. This possibly explains the higher liver uptake in the long COVID group compared to the control group.

The results of this study should be considered alongside certain limitations. Firstly, the study population consisted of 13 long COVID patients, limiting the power of the study. The control group could not be matched for age and sex to the long COVID group due to limitations in our database. Due to the large heterogeneity of [18F]FDG-uptake within both groups, the TBR distributions overlapped between the two groups. This was an important cause for the high p-values we found in the semi-qualitative and TVS analyses.

Another limitation is that the image reconstruction was not EARL compliant since EARL specifications were not yet applied at the time of acquisition, which might have resulted in increased SUV variability [33]. Moreover, the time interval between [18F]FDG injection and image acquisition was lower than 60 minutes in both groups due to logistic reasons, which deviates from the EANM recommendation for LVV and PMR, which Sollini *et al.* did

adhere to [16,22]. This may have had an impact on the results, although no guidelines on the recommended time interval between [18F]FDG injection and image acquisition have been published for long COVID patients and there were no significant differences in interval time between the two groups.

Moreover, the scanning window (whole-body imaging versus torso imaging) should be consistent for all subjects in order to be able to assess all locations [34]. Future studies should also consider specifying and quantifying the location of pain per patient.

It should also be noted that all measurements were manually performed and thus prone to errors [33]. Nonetheless, the nuclear medicine physicians (SB and RA) had a minimum of 5 years of experience and measurements were performed carefully, minimizing the number of random errors.

Little is known about long COVID and patients' management is still inconsistent due to lack of clinical practice guidelines. Furthermore, [18F]FDG-PET/CT data in long COVID patients was limited. Although our retrospective proof of concept study concerns only a small study population, we believe that our findings exhibit the complexity of the disease and add to the knowledge of the application of [18F]FDG-PET/CT in long COVID.

In summary, we found no quantitative difference in the TBR or TVS between long COVID patients and controls. Based on our results, we are unable to prove that [18F]FDG-PET/CT scans are of added value for long COVID patients with symptoms of myalgia or joint pain, reminiscent of vasculitis and PMR. To gain more insight in the underlying mechanisms of long COVID, prospective cohort studies are necessary.

REFERENCES

- 1. Shi Y, Wang G, Cai X, Deng J, Zheng L, Zhu H, et al. An overview of COVID-19. 2020;21(5):343-60.
- Wang D, Hu B, Hu C, Zhu F, Liu X, Zhang J, et al. Clinical Characteristics of 138 Hospitalized Patients with 2019 Novel Coronavirus-Infected Pneumonia in Wuhan, China. JAMA - J Am Med Assoc. 2020;323(11):1061–9.
- 3. Yue H, Bai X, Wang J, Yu Q, Liu W, Pu J, et al. Clinical characteristics of coronavirus disease 2019 in Gansu province, China. Ann Cardiothorac Surg. 2020;9(4):1404–12.
- Iqbal A, Iqbal K, Arshad Ali S, Azim D, Farid E, Baig MD, et al. The COVID-19 Sequelae: A Cross-Sectional Evaluation of Post-recovery Symptoms and the Need for Rehabilitation of COVID-19 Survivors. Cureus. 2021;2(2).
- Wu Z, McGoogan JM. Characteristics of and Important Lessons from the Coronavirus Disease 2019 (COVID-19) Outbreak in China: Summary of a Report of 72314 Cases from the Chinese Center for Disease Control and Prevention. JAMA - J Am Med Assoc. 2020;323(13):1239–42.
- Raveendran A V, Jayadevan R, Sashidharan S. Since January 2020 Elsevier has created a COVID-19 resource centre with free information in English and Mandarin on the novel coronavirus COVID- 19. The COVID-19 resource centre is hosted on Elsevier Connect, the company's public news and information. 2020;(January).
- Taquet M, Dercon Q, Luciano S, Geddes JR, Husain M, Harrison PJ. Incidence, co-occurrence, and evolution of long-COVID features: A 6-month retrospective cohort study of 273,618 survivors of COVID-19. PLoS Med [Internet]. 2021;18(9):1–22. Available from: http://dx.doi.org/10.1371/journal. pmed.1003773
- Davis HE, Assaf GS, McCorkell L, Wei H, Low RJ, Re'em Y, et al. Characterizing long COVID in an international cohort: 7 months of symptoms and their impact. eClinicalMedicine. 2021;38.
- Shaw B, Daskareh M, Gholamrezanezhad A. The lingering manifestations of COVID-19 during and after convalescence: update on long-term pulmonary consequences of coronavirus disease 2019 (COVID-19). Radiol Medica [Internet]. 2021;126(1):40–6. Available from: https://doi.org/10.1007/ s11547-020-01295-8
- Carfi A, Bernabei R, Landi F. Persistent Symptoms in Patients After Acute COVID-19. N Engl J Med. 2020;324(6):603–5.
- Siddiqi HK, Libby P, Ridker PM. Since January 2020 Elsevier has created a COVID-19 resource centre with free information in English and Mandarin on the novel coronavirus COVID-19. The COVID-19 resource centre is hosted on Elsevier Connect, the company's public news and information. Trends. 2020;31(January):1–5.
- Zacharias H, Dubey S, Koduri G, Cruz DD. Since January 2020 Elsevier has created a COVID-19 resource centre with free information in English and Mandarin on the novel coronavirus COVID-19. The COVID-19 resource centre is hosted on Elsevier Connect, the company's public news and information. 2020;(January).
- Derksen VFAM, Kissel T, Lamers-Karnebeek FBG, Van Der Bijl AE, Venhuizen AC, Huizinga TWJ, et al. Onset of rheumatoid arthritis after COVID-19: Coincidence or connected? Ann Rheum Dis. 2021;80(8):1096–8.
- Viner R, Whittaker E. Kawasaki-like disease: emerging complication during the COVID-19 pandemic. 2020;(January).
- 15. Jamar F, Buscombe J, Chiti A, Christian PE, Delbeke D, Donohoe KJ, et al. EANM/SNMMI guideline for 18F-FDG use in inflammation and infection. J Nucl Med. 2013;54(4):647–58.

- Sollini M, Ciccarelli M, Cecconi M, Aghemo A, Morelli P, Gelardi F, et al. Vasculitis changes in COVID-19 survivors with persistent symptoms: an [(18)F]FDG-PET/CT study. Eur J Nucl Med Mol Imaging. 2020/10/31. 2021;48(5):1460–6.
- Sollini M, Morbelli S, Ciccarelli M, Cecconi M, Aghemo A, Morelli P, et al. Long COVID hallmarks on [18F]FDG-PET/CT: a case-control study. Eur J Nucl Med Mol Imaging. 2021/03/08. 2021;48(10):3187–97.
- Rodríguez-Alfonso B, Ruiz Solís S, Silva-Hernández L, Pintos Pascual I, Aguado Ibáñez S, Salas Antón C. (18)F-FDG-PET/CT in SARS-CoV-2 infection and its sequelae. Rev Esp Med Nucl Imagen Mol (Engl Ed). 2021/08/04. 2021;40(5):299–309.
- Pan T, Einstein SA, Kappadath SC, Grogg KS, Lois Gomez C, Alessio AM, et al. Performance evaluation of the 5-Ring GE Discovery MI PET/CT system using the national electrical manufacturers association NU 2-2012 Standard. Med Phys. 2019;46(7):3025–33.
- Keyes Jr J. SUV: standard uptake or silly useless value? J Nucl Med [Internet]. 1995;36(10):1836–
 Available from: http://www.osti.gov/scitech/biblio/478317
- Kinahan PE, Fletcher JW. Positron emission tomography-computed tomography standardized uptake values in clinical practice and assessing response to therapy. Semin Ultrasound, CT MRI. 2010;31(6):496–505.
- 22. Slart RHJA, Slart RHJA, Glaudemans AWJM, Chareonthaitawee P, Treglia G, Besson FL, et al. FDG-PET/CT(A) imaging in large vessel vasculitis and polymyalgia rheumatica: joint procedural recommendation of the EANM, SNMMI, and the PET Interest Group (PIG), and endorsed by the ASNC. Eur J Nucl Med Mol Imaging. 2018;45(7):1250–69.
- Boellaard R, Krak NC, Hoekstra OS, Lammertsma A a, Jaskowiak CJ, Bianco J a, et al. Effects of Noise, Image Resolution, and ROI Definition on the Accuracy of Standard Uptake Values: A Simulation Study. J Nucl Med [Internet]. 2002;45(3):670–8. Available from: http://www.ncbi.nlm. nih.gov/pubmed/15750154%5Cnhttp://www.ncbi.nlm.nih.gov/pubmed/15347719
- 24. Sedgwick P. Multiple significance tests: The Bonferroni correction. BMJ. 2012;344(7841):1–2.
- 25. Curtin F, Schulz P. Multiple correlations and Bonferroni's correction. Biol Psychiatry. 1998;44(8):775–7.
- Rehak Z, Sprlakova-Pukova A, Kazda T, Fojtik Z, Vargova L, Nemec P. (18)F-FDG PET/CT in polymyalgia rheumatica-a pictorial review. Br J Radiol. 2017/05/17. 2017;90(1076):20170198.
- Rehak Z, Vasina J, Nemec P, Fojtik Z, Koukalova R, Bortlicek Z, et al. Various forms of (18)F-FDG PET and PET/CT findings in patients with polymyalgia rheumatica. Biomed Pap Med Fac Univ Palacky Olomouc Czech Repub. 2015/05/27. 2015;159(4):629–36.
- Rodríguez-Alfonso B, Ruiz Solís S, Silva-Hernández L, Pintos Pascual I, Aguado Ibáñez S, Salas Antón C. (18)F-FDG-PET/CT in SARS-CoV-2 infection and its sequelae. Rev Esp Med Nucl Imagen Mol. 2021/07/28. 2021;40(5):299–309.
- Sollini M, Morbelli S, Ciccarelli M, Cecconi M, Aghemo A, Morelli P, et al. Long COVID hallmarks on [18F]FDG-PET/CT: a case-control study. Eur J Nucl Med Mol Imaging. 2021/03/08. 2021;48(10):3187–97.
- Maiese A, Manetti AC, La Russa R, Di Paolo M, Turillazzi E, Frati P, et al. Autopsy findings in COVID-19-related deaths: a literature review. Forensic Sci Med Pathol. 2020/10/08. 2021;17(2):279–96.
- 31. Libby P, Lüscher T. COVID-19 is, in the end, an endothelial disease. Eur Hear J. 2020/09/04. 2020;41(32):3038–44.

- 32. Bai Y, Xu J, Chen L, Fu C, Kang Y, Zhang W, et al. Inflammatory response in lungs and extrapulmonary sites detected by [(18)F] fluorodeoxyglucose PET/CT in convalescing COVID-19 patients tested negative for coronavirus. Eur J Nucl Med Mol Imaging. 2021/01/10. 2021;48(8):2531–42.
- 33. Kaalep A, Burggraaff CN, Pieplenbosch S, Verwer EE, Sera T, Zijlstra J, et al. Quantitative implications of the updated EARL 2019 PET-CT performance standards. EJNMMI Phys. 2019;6(1):1–16.
- Lensen KJDF, Van Sijl AM, Voskuyl AE, Van Der Laken CJ, Heymans MW, Comans EFI, et al. Variability in quantitative analysis of atherosclerotic plaque inflammation using 18F-FDG PET/ CT. PLoS One. 2017;12(8):1–14.



CHAPTER 4

[18F]FDG administered activity reduction capabilities of a 32-cm axial field-of-view solid-state digital bismuth germanium oxide PET/CT system while maintaining EARL compliance

Authors

A. van de Burgt, P. Dibbets-Schneider, F. Kotasidis, L.F. de Geus-Oei, D.D.D. Rietbergen and F.H.P. van Velden

Published

Physica Medica, 2025; 131: 104935, DOI: 10.1016/j.ejmp.2025.104935

Supplementary materials

https://doi.org/10.1016/j.ejmp.2025.104935

ABSTRACT

Purpose

To assess the lower [18F]FDG limit in administered activity and/or scan time reduction capabilities of a digital-BGO 32-cm axial field-of-view PET system while being compliant with current and updated EANM Research Ltd Fluorine-18 accreditation specifications (EARL, and EARL,).

Methods

EARL $_1$ and EARL $_2$ compliance of the digital-BGO system (Omni Legend 32 cm) was tested for several reconstructions, including those that apply precision deep learning-based image enhancement (PDL) as postprocessing, using the calibration QC and NEMA IEC phantom measurements. The image quality QC scan was repeated every hour for 7 hours, with each subsequent hour representing a lower administered activity, and reconstructed for various times per bed position, i.e. 30, 60, 120, 180, and 300 seconds. For each of the image quality QC images, coefficient of variation (COV) of the background compartment, and mean, maximum and peak activity concentration recovery coefficients (RC $_{\rm mean}$, RC $_{\rm max}$ and RC $_{\rm peak}$) of differently-sized spheres were calculated and compared to current and updated EARL accreditation specifications.

Results

When we apply 1 min per bed position for PET acquisition, [18F]FDG administration can be reduced by a factor of ~4 for EARL₁, by a factor of ~8 for EARL₂ (2 mm voxels) and by a factor of ~4 for EARL₂ (4 mm voxels) using both standard reconstructions and PDL post-processing compared to current EANM recommendations for [18F]FDG administration (7 MBq·min·bed⁻¹·kg⁻¹).

Conclusions

Reduction in [18 F]FDG administered activity is possible by at least a factor 4 for 1 min/bed with the Omni Legend 32 cm PET/CT while maintaining EARL, and EARL, compliance.

Keywords

Administered activity reduction; scan time reduction; PET/CT; EARL ¹⁸F accreditation; phantom study; [¹⁸F]FDG

INTRODUCTION

Positron emission tomography/computed tomography (PET/CT) imaging is a powerful tool that enables whole body non-invasive visualization and quantification of biological processes at the molecular level [1]. Continuous advancements in PET/CT technology have led to improved image quality and increased sensitivity, thereby potentially enhancing diagnostic accuracy which may lead to better patient outcomes [2]. Recently, a digital PET/ CT with bismuth germanium oxide scintillating crystals coupled to silicon photomultipliers (SiPM) over an extended 32 cm axial field-of-view (FOV) was introduced (Omni Legend; GE HealthCare, Milwaukee, USA). This novel non-time-of-flight PET/CT system demonstrates high count rates (peak noise-equivalent count rates: ~500 kcps) and a superior sensitivity (45-49 cps/kBq) according to the National Electric Manufacturer's Association (NEMA) NU2-2018 standard [3], while maintaining a spatial resolution comparable to other current SiPM-based time-of-flight PET/CT systems [4-6]. Moreover, it incorporates precision deep learning-based image enhancement (PDL) that aims to provide improved feature sharpness and convergence comparable to hardware-based time-of-flight reconstruction [7]. The enhanced sensitivity of the system provides possibilities to reduce both scan duration and/or the administered activity of radiopharmaceuticals. Shorter scan durations may enhance patient comfort, increase patient throughput and decrease the risk of patient motion. Lowering the administered activity offers opportunities for cost savings and reduces the risks associated with radiation exposure for both staff and patients [5]. Kennedy et al. briefly highlighted the potential to reduce administered activity and scan time of the Omni legend PET/CT system for various radiotracers and injected activities [5], but a thorough investigation into the administered activity and/or scan time reduction capabilities of this new system has not yet been conducted. This study aims to assess the lower limit in administered activity of 2-deoxy-2-[18F]fluoro-D-glucose ([18F]FDG) and/ or scan time reduction capabilities for the Omni Legend PET/CT while being compliant with current and updated European Association of Nuclear Medicine (EANM) Research Ltd Fluorine-18 accreditation specifications (EARL, and EARL,).

MATERIAL AND METHODS

 EARL_1 and EARL_2 compliance of the Omni Legend system was tested using calibration QC and NEMA IEC phantom measurements [8-11].

Phantom studies

All PET acquisitions covered two bed positions with a 47% bed overlap and were performed on an EARL ¹⁸F standards 1 and 2 accredited PET/CT system (Omni Legend 32 cm, GE Healthcare, Milwaukee, USA) [8, 9]. Prior to each PET scan, a low-dose CT scan (120 kVp. 52 mAs, with dose modulation) was acquired for attenuation correction purposes.

For the calibration QC scan, a cylindrical uniformity phantom with a diameter of 20 cm and a length of 30 cm was filled with distilled water and 82.2 MBq of [¹⁸F]FDG, and placed in the centre of the FOV. A PET scan was acquired in list-mode for 5 min per bed position.

For assessing the system-specific patient [18F]FDG activity using image quality QC scans, a NEMA IEC body phantom, equipped with six fillable spheres varying in diameter (10, 13, 17, 22, 28, and 37 mm) and a lung insert, was filled with distilled water, and 2.39 kBq/mL (uniform background compartment) and 22.6 kBq/mL (spheres) of [18F]FDG, simulating a sphere to background ratio of ~10:1. The spheres of the phantom were positioned in the centre of the FOV. A PET scan was acquired in list-mode for 10 min per bed position (T0), and repeated every hour for 7 hours (T0+1h to T0+7h), with each subsequent hour representing a lower activity. Boellaard et al described the entire procedure for assessing system-specific patient [18F]FDG activity preparations for quantitative [18F]FDG PET/CT studies [10].

More details for preparation and acquisition requirements of EARL fluor-18 accreditation can be found in the EARL standard operating procedures [11].

PET reconstructions

The list-mode data of the PET scan of the calibration QC were histogrammed into sinograms of 300 seconds per bed position, while the list-mode data of each PET scan (T0 till T0+7h) of the image quality QC were histogrammed into sinograms of 30, 60, 120, 180, and 300 seconds per bed position. The 300 seconds per bed position of T0 was used to validate the image quality of the reconstructions to be $EARL_1$ or $EARL_2$ compliant. The following five reconstructions were performed:

 EARL, images were reconstructed using a 3D maximum likelihood ordered subset expectation maximization reconstruction (3D OSEM) (VUEPointHD (VPHD)) with 4 iterations and 12 subsets, followed by a 7 mm full-width-at-half-maximum (FWHM) Gaussian filter and a 192x192 matrix, resulting in a voxel size of $3.65 \times 3.65 \times 2.07$ mm³ (1).

- EARL₂ 2 mm images were reconstructed using a Bayesian penalised likelihood reconstruction (BPL; Q.Clear) with a β parameter of 1500 and a 384x384 matrix, resulting in 1.82 x 1.82 x 2.07 mm³ voxels (2), and repeated with PDL post-processing using a 'low' level of contrast-enhancement (3).
- EARL₂ 4 mm images were reconstructed using BPL with a β parameter of 1200 and a 192 x 192 matrix, resulting in 3.65 x 3.65 x 2.07 mm³ voxels (4), and repeated with the 'low' level of PDL post-processing (5).

All reconstructions were performed with corrections for attenuation, scatter, normalization, decay, and dead time. For each of the image quality QC images, coefficient of variation (COV) of the background compartment, and mean, maximum and peak activity concentration recovery coefficients (RC_{mean} , RC_{max} and RC_{peak}) of differently-sized spheres were calculated and compared to current and updated EARL accreditation specifications [8, 10, 12].

Data analysis

For each PET image of the calibration QC, the average volumetric standardized uptake value (SUV) bias, which cannot exceed 10%, is calculated by:

$$SUV_{bias}(\%) = \left(\frac{C_{measured}}{C_{calculated}} - 1\right) \times 100\%$$
 (1)

In this equation $C_{\mbox{\scriptsize measured}}$ represents the activity concentration measured from images and $C_{\text{calculated}}$ is the true activity concentration calculated from injection data. The SUV_{bias} was generated using the manual tool implemented in IDL (version 8.4; Harris Geospatial Solutions, Bloomfield, USA) by Boellaard et al [8, 12]. Maximum, peak and mean SUV recovery coefficients (RC $_{max}$, RC $_{mean}$ and RC $_{neak}$) were computed for all spheres on each reconstructed PET image quality QC images using an in-house-developed algorithm in MATLAB (version 2018b; MathWorks, Massachusetts, USA), cross-validated with the aforementioned manual tool implemented in IDL by Boellaard et al [8, 12], with a deviation of <1%. In short, this in-house-developed algorithm in MATLAB, using the known geometry of the NEMA IEC body phantom, locates the centroids of the spheres from the PET image and draws volumes of interest (VOIs) on the six spheres together with 3 cm rectangular VOIs (n=9) at predetermined locations (relative to the sphere location and depending on the sphere orientation and position) in the background compartment of the phantom (Figure 1), onto each reconstructed PET image. To limit the effects of partial voxels, using the known sphere diameter, a raster of sample points is created every 0.1 mm and the values are interpolate in these 0.1 locations, thereby creating a finer sampling than the original voxels. For each sphere, the max and peak values are obtained (for the calculation of RC_{max} and RC_{peak}) from the original PET images, and a VOI is created by a 50% background-corrected isocontour method to derive the mean value for the calculation of RC_{mean} . The RC values are calculated by:

$$RC = \frac{S_{measured}}{S_{calculated}} \tag{2}$$

In this equation $S_{measured}$ represents the max, peak or mean activity concentration measured from the VOIs of each sphere and $S_{calculated}$ is the true activity concentration calculated from injection data for the spheres. The obtained RC values should comply to the EARL₁ (RC_{max} and RC_{mean}) and EARL₂ (also includes RC_{peak}) accreditation specifications [11]. In addition, the coefficient of variation (COV), determined by dividing the standard deviation by the mean of the pixel values within a VOI, was initially computed for each individual 3 cm rectangular VOIs placed in the background compartment (n=9). Subsequently, the final COV parameter was obtained by averaging these 9 COV values. It was essential that the resulting average COV remained below 15% [10].

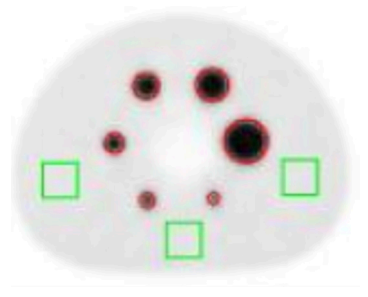


Figure 1. Visualization of the template of the NEMA IEC body phantom geometry used by the in-house-developed algorithm, showing the volumes-of-interest (VOIs) of the six spheres identified on the PET image (red circles) and the rectangular background VOIs (3 cm, n=9, green squares) in axial view.

RESULTS

EARL, and EARL, compliance

The calibration QC revealed a median SUV bias of 1.16% (range: 0.40—1.55%). RC_{max} , RC_{mean} and (when applicable) RC_{peak} of all tested reconstructions were $EARL_1$ or $EARL_2$ compliant (Figure 2 and Supplemental file S1).

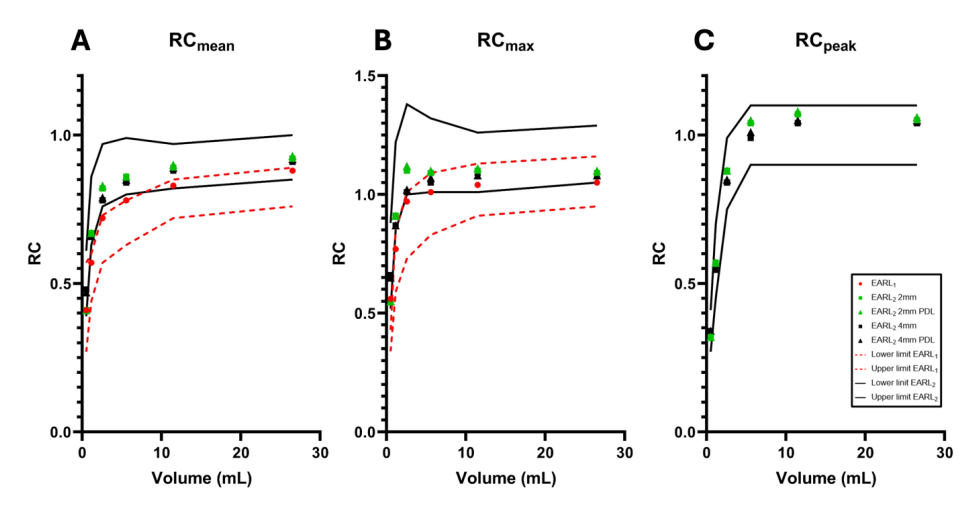


Figure 2. Max (A), mean (B) and peak (C; only EARL₂) recovery coefficients (RC) as a function of volume (mL), derived from the image quality QC scan acquired at T0, using 300 seconds per bed position. PDL: precision deep learning image enhancement.

Administered activity and/or scan time reduction capabilities

When we apply 1 min per bed position for PET acquisition, [¹⁸F]FDG administration can be reduced by a factor of ~4 for EARL₁, by a factor of ~8 for EARL₂ (2 mm) and by a factor of ~4 for EARL₂ (4 mm) using both standard reconstructions (Figure 3A) and PDL post-processing (Figure 3B) compared to current EANM recommendations for FDG administration (7 MBq·min·bed⁻¹·kg⁻¹ of [¹⁸F]FDG for a 75 kg patient [9]). This indicates a decrease in MBq/kg for the used reconstructions to 1.75 MBq/kg, 0.88MBq/kg and 1.75 MBq/kg, respectively. EARL₂ reconstructions (2 mm and 4 mm voxels) both with and without PDL allowed similar reductions in administered activity, with lower COV values for with PDL (maximum COV difference: 5.2% for 2 mm and 16.5% for 4 mm). Due to the higher beta value applied for EARL₂ 2 mm, EARL₂ 4 mm voxel size has generally higher COVs than 2 mm, contrary to the expectation of smaller voxels exhibiting higher noise and COV (maximum COV difference: 32.4% with PDL and 45.5% without PDL).

_			Time per bed position (s)													
Α	Activity			EARL	1			EARL ₂ 2mm				EARL ₂ 4mm				
No PDL	(MBq/kg)	30	60	120	180	300	30	60	120	180	300	30	60	120	180	300
T0	4	12.6	9.7	7.9	6.2	3.9	9.6	6.7	4.9	3.6	2.6	11.3	8.5	5.9	4.1	3.2
T0 + 1h	2.73	17.1	12.4	8.6	6.8	4.1	10.2	7.7	4.4	3.6	2.7	13.4	8.6	5.7	4.3	3.5
T0 + 2h	1.87	19.2	13.6	11.1	7.6	5.7	10.6	8.9	6.2	5.3	3.8	15.4	11.0	7.7	5.9	4.3
T0 + 3h	1.29	24.1	17.4	12.6	9.9	8.0	17.6	10.3	7.1	5.8	5.1	24.2	13.9	9.2	6.9	5.7
T0 + 4h	0.88	25.3	18.2	12.7	11.0	8.8	18.3	12.6	8.0	6.5	5.0	30.5	16.8	9.6	7.9	5.7
T0 + 5h	0.56	30.2	20.3	19.2	16.3	10.9	25.0	15.4	12.8	10.0	7.0	44.4	21.3	16.7	12.6	8.9
T0 + 6h	0.41	32.7	27.3	20.7	16.5	13.1	28.8	21.7	11.6	9.8	8.2	58.3	37.9	18.8	12.8	10.0
T0 + 7h	0.28	36.5	30.5	20.5	16.8	15.1	40.7	24.3	15.1	11.7	9.9	86.2	52.9	23.3	15.7	12.3
	l		Γ		A	ctivity				Time	per be	d positi	on (s)			
				В	(M	Bq/kg)		EA	RL ₂ 2m	ım			EA	RL ₂ 4n	nm	
				PDL			30	60	120	180	300	30	60	120	180	300
			-	TO	_	4	8.7	6.2	4.0	2.9	2.2	7.8	6.3	4.5	3,2	2.4
				T0 + 1h		2.73		7.0	3.4	2.9	2.5	12.4	5.9	4.1	3.0	2.5
	15 All reco						8.3		3.4	2.9	2.5			4.1	3.0	
	ents comply ation speci			T0 + 2h		1.87	8.3	7.5	5.6	4.6	3.0	13.6	7.7	5.6	4.5	3.0
COV≤	15 One or	more		T0 + 3h		1.29	14.4	8.5	6.0	5.0	4.4	18.0	10.1	6.1	4.8	4.2
	fall outside ation speci		ns	T0 + 4h		0.88	14.3	10.2	6.8	5.6	4.2	22.8	13.4	6.5	5.2	4.1
	for SUV mean, maximum and/or peak activity		n	T0 + 5h		0.56	20.5	12.2	10.9	8.6	6.2	34.0	15.2	12.8	9.3	6.4
	ration reco			T0 +6h		0.41	23.5	17.8	9.0	9.1	7.3	49.9	29.5	13.2	10.0	7.4
coefficie			-	T0 + 7h		0.28	37.3	19.1	11.9	11.2	8.5	69.7	40.0	16.3	10.6	8.5

Figure 3. EARL $_1$ and EARL $_2$ (2 mm and 4 mm) compliance illustrating coefficient of variation (COV) at various [18 F]FDG activity dosages and scan durations for reconstructions without (A) and with (B) precision deep learning image enhancement (PDL). SUV: standardized uptake value.

DISCUSSION

This phantom study provides an initial insight into the applicable lower limit in [18 F]FDG administered activity and/or scan time reduction while being EARL $_1$ and EARL $_2$ Fluorine-18 compliant for the Omni Legend PET/CT system. Despite the larger voxel size, EARL $_2$ (4 mm) COV data were higher overall than EARL $_2$ (2 mm), which may be attributed to the higher beta value used in the 2 mm BPL reconstruction. Moreover, using the same method to assess reduction in administered activity, van Sluis et al. reported factors of reductions in administered activity at 1 min/bed of $^{\sim}8$ (EARL $_1$), $^{\sim}4$ (EARL $_2$, 4 mm) and 1 (EARL $_2$, 2 mm), where our results gave factors $^{\sim}4$, $^{\sim}8$ and $^{\sim}4$, respectively [13]. This difference can be

explained by their use of a different scanner and reconstruction algorithms. Furthermore, our data show comparable findings for EARL₂ 2 mm on the Omni Legend system compared to Kennedy et al. (0.88 for our study compared to 1 MBq·min·bed⁻¹·kg⁻¹ for Kennedy et al), yet scan times and reduction in administered activity are less thoroughly covered in their study [5]. Note that each institution is advised to explore different reconstruction parameters of their scanner to ensure EARL compliance with our indicated reductions in administered activity.

Our study has limitations. First, the NEMA IEC body phantom only simulates a 75 kg patient. Preferably, the validation should be replicated using phantoms simulating various patient sizes [14]. Second, we used one strategy to assess the reduction in administered activity, however, alternative methods are available to assess reduction in administered activity [15-18]. Third, this phantom does not reflect real-world conditions. Ideally, for future work we recommend that a clinical study should be performed to validate the image quality, the potential role of deep learning-enhanced post-processing and quantitative accuracy using [18F]FDG PET data of patients scanned at the chosen lower regime in administered activity and/or reduced scan times. Note that the identified lower limits of [18F]FDG administered activity only apply to the Omni Legend 32 cm PET/CT and that new studies should be performed to investigate the lower limits of [18F]FDG administered activity for other PET systems.

In conclusion, we demonstrate in this phantom study that a reduction in [18 F]FDG administered activity is possible by at least a factor 4 for 1 min/bed with the Omni Legend 32 cm PET/CT while maintaining EARL $_1$ and EARL $_2$ compliance. A clinical study should be performed to validate these findings.

REFERENCES

- von Schulthess GK, Steinert HC, Hany TF. Integrated PET/CT: current applications and future directions. Radiology. 2006:238:405-22.
- 2. Singh M. A review of digital PET-CT technology: comparing performance parameters in SiPM integrated digital PET-CT systems. Radiography (Lond). 2024;30:13-20.
- Association NEM, Association NEM. NEMA standards publication NU 2–2018: performance measurements of Positron emission tomographs. National Electrical Manufacturers Association. 2018.
- Smith RL, Bartley L, O'Callaghan C, Haberska L, Marshall C. NEMA NU 2-2018 evaluation and image quality optimization of a new generation digital 32-cm axial field-of-view Omni Legend PET-CT using a genetic evolutionary algorithm. Biomedi Phys Eng Express. 2024;10:025032.
- Kennedy JA, Palchan-Hazan T, Maronnier Q, Caselles O, Courbon F, Levy M, et al. An extended bore length solid-state digital-BGO PET/CT system: design, preliminary experience, and performance characteristics. Eur J Nucl Medi Mol Imaging. 2024;51:954-64.
- Yamagishi S, Miwa K, Kamitaki S, Anraku K, Sato S, Yamao T, et al. Performance Characteristics of a New-Generation Digital Bismuth Germanium Oxide PET/CT System, Omni Legend 32, According to NEMA NU 2-2018 Standards. J Nucl Med. 2023;64:1990-7.
- Mehranian A, Wollenweber SD, Walker MD, Bradley KM, Fielding PA, Huellner M, et al. Deep learning—based time-of-flight (ToF) image enhancement of non-ToF PET scans. Eur J Nucl Med Mol Imaging. 2022;49:3740-9.
- Kaalep A, Sera T, Rijnsdorp S, Yaqub M, Talsma A, Lodge MA, et al. Feasibility of state of the art PET/CT systems performance harmonisation. Eur J Nucl Med Mol Imaging. 2018;45:1344-61.
- Boellaard R, Delgado-Bolton R, Oyen WJ, Giammarile F, Tatsch K, Eschner W, et al. FDG PET/ CT: EANM procedure guidelines for tumour imaging: version 2.0. Eur J Nucl Med Mol imaging. 2015;42:328-54.
- Boellaard R, Willemsen A, Arends B, Visser E. EARL procedure for assessing PET/CT system specific patient FDG activity preparations for quantitative FDG PET/CT studies. Last Accessed Sept [Internet]. 2014 2018.
- Manual for EARL FDG-PET/CT Accreditation: Version 4.2. Vienna, Austria: EANM Research Ltd.;.March 2017.
- 12. Boellaard R. Quantitative oncology molecular analysis suite: ACCURATE. J Nucl Med. 2018.
- 13. Van Sluis J, De Jong J, Schaar J, Noordzij W, Van Snick P, Dierckx R, et al. Performance characteristics of the digital biograph vision PET/CT system. J Nucl Med. 2019;60:1031-6.
- 14. Peters SM, van der Werf NR, Segbers M, van Velden FH, Wierts R, Blokland KA, et al. Towards standardization of absolute SPECT/CT quantification: a multi-center and multi-vendor phantom study. EJNMMI Phys. 2019;6:1-14.
- de Groot EH, Post N, Boellaard R, Wagenaar NR, Willemsen AT, van Dalen JA. Optimized dose regimen for whole-body FDG-PET imaging. EJNMMI Res. 2013;3:1-11.
- Wickham F, McMeekin H, Burniston M, McCool D, Pencharz D, Skillen A, et al. Patient-specific optimisation of administered activity and acquisition times for 18 F-FDG PET imaging. EJNMMI Res. 2017;7:1-11.

- 17. Prieto E, García-Velloso MJ, Rodríguez-Fraile M, Morán V, García-García B, Guillén F, et al. Significant dose reduction is feasible in FDG PET/CT protocols without compromising diagnostic quality. Phys Med. 2018;46:134-9.
- Katsari K, Penna D, Arena V, Polverari G, Ianniello A, Italiano D, et al. Artificial intelligence for reduced dose 18F-FDG PET examinations: a real-world deployment through a standardized framework and business case assessment. EJNMMI Phys. 2021;8:1-15.



PART 2

Novel clinical applications of quantitative SPECT/CT



CHAPTER 5

Experimental validation of absolute SPECT/ CT quantification for response monitoring in patients with coronary artery disease

Authors

A. van de Burgt, P. Dibbets-Schneider, C.H. Slump, A.J.H.A. Scholte, D.E. Atsma, L.F. de Geus-Oei and F.H.P. van Velden

Published

EJNMMI physics, 2021; 8(1): 48, DOI: 10.1186/s40658-021-00393-4

Supplementary materials

https://doi.org/10.1186/s40658-021-00393-4

ABSTRACT

Background

Quantitative SPECT enables absolute quantification of uptake in perfusion defects. The aim of this experimental study is to assess quantitative accuracy and precision of a novel iterative reconstruction technique (Evolution; GE Healthcare) for the potential application of response monitoring using ^{99m}Tc-tetrofosmin SPECT/CT in patients with coronary artery disease (CAD).

Methods

Acquisitions of an anthropomorphic torso phantom with cardiac insert containing defects (with varying sizes), filled with ^{99m}Tc-pertechnetate, were performed on a SPECT/CT (Discovery 670 Pro, GE Healthcare). Subsequently, volumes-of-interest of the defects were manually drawn on CT to assess the recovery coefficient (RC). Bull's eye plots were composed to evaluate the uptake per segment. Finally, ^{99m}Tc-tetrofosmin SPECT/CT scans of 10 CAD patients were used to illustrate clinical application.

Results

The phantom study indicated that Evolution showed convergence after 7 iterations and 10 subsets. The average repeatability deviation of all configurations was 2.91% and 3.15% (%SD mean) for filtered (Butterworth) and unfiltered data, respectively. The accuracy after post-filtering was lower compared to the unfiltered data with a mean(SD) RC of 0.63(0.05) and 0.70(0.07), respectively (p<0.05). More artificial defects were found on Bull's eye plots created with the unfiltered data compared to filtered data. Eight out of ten patients showed significant changes in uptake before and after treatment (p<0.05).

Conclusion

Quantification of ^{99m}Tc-tetrofosmin SPECT/CT seems feasible for CAD patients when 7 iterations (10 subsets), Butterworth post-filtering (cut off frequency 0.52in cycles/cm, order of 5) and manual CT-delineation are applied. However, future prospective patient studies are required for clinical application.

Keywords

^{99m}Tc-tetrofosmin, SPECT/CT, experimental validation, quantitative SPECT, coronary artery disease, phantom study

INTRODUCTION

Myocardial perfusion imaging is used to evaluate the presence and severity of coronary artery disease (CAD) [1, 2]. Myocardial perfusion scintigraphy (MPS) using single photon emission computed tomography (SPECT), typically obtained on a CZT camera, is the most extensively validated imaging modality for this purpose [3] and is routinely used to manage treatment strategies [2, 4]. Moreover, monitoring the response of CAD treatments with MPS may guide treatment decision making.

MPS is based on visual interpretation of relative myocardial perfusion and might underestimate the severity of ischemia due to global hypoperfusion [5]. Hence, it is worth investigating how quantitative SPECT may enable measurement of uptake in perfusion defects to improve evaluation of response to anti-ischemic therapies using myocardial perfusion scans.

Recent developments in iterative imaging reconstruction, such as Evolution (Q.Metrix package, GE Healthcare, Milwaukee, USA) available on a Xeleris workstation (version 4.0) [6], allows SPECT to provide absolute quantification. Evolution is an ordered subset expectation maximization algorithm that includes compensation for collimator—detector response, attenuation and scatter correction, and resolution recovery. Evolution has been validated for oncological trials using phantom studies for assessing early response to treatment in locally advanced breast cancer patients [7] and for the differentiation of normal bone and bone disease [8]. Nonetheless, to the best of our knowledge, no validation has been performed for cardiac studies.

Therefore, the aim of this experimental study is to assess quantitative accuracy and precision of Evolution, making use of phantom studies, supplemented with illustrative patient cases, for potential clinical application of response monitoring using ^{99m}Tc-tetrofosmin SPECT/CT in patients with CAD.

MATERIALS AND METHODOLOGY

Phantom studies

In an anthropomorphic torso phantom (model ECT/TOR/P, DATA Spectrum, Hillsborough, NC, USA) a static cardiac insert was used (Data spectrum cardiac phantom model ECT/CAR/UM, DATA Spectrum, Hillsborough, NC, USA; Figure 1), consisting of a left ventricle with separate compartments for blood pool (with a volume of 61 mL) and myocardium (with wall thickness of 10 mm and volume of 100 mL). The insert compartments were filled

with a solution of water and ^{99m}Tc-pertechnetate. Three fillable defects (small, 2.6 mL; medium, 5.6 mL; and large, 11.8 mL) were evaluated to simulate a myocardial perfusion defect. The defects were positioned in the anterior or inferior wall of the myocardium, or a combination of both. The cardiac insert was positioned in an anthropomorphic torso phantom containing lung, liver and spine inserts. The myocardium was filled with 64 kBq/mL. Moreover, the liver was filled with 15.9 kBq/mL according to a myocardium-to-liver ratio of 4:1. The myocardium-to-background ratio was approximately 12:1. In addition, the myocardium-to-blood pool ratio was 10:1 and the defect-to-myocardium ratio was 1:2, based on literature [9-11]. The lungs were filled with polystyrene spheres and water to achieve a representative physiologic tissue density.

A total of 36 measurements were acquired and evaluated: six configurations with six acquisitions. The first three single configurations are the described fillable defects measured separately on the mid anterior part of the myocardium, further referred to as small (S-configuration), medium (M-configuration) and large (L-configuration). The fourth and fifth configuration are two combinations of two defects and were positioned on the mid-inferior and mid-anterior part of the myocardium. These double defect configurations consist of two small defects (SS-configuration) and a combination of a small and medium defect (SM-configuration). Finally, the phantom was also scanned without defects, further referred to as the ground truth (GT-configuration). The measurements were repeated six times with a time per view that was adjusted per repetition to compensate for the radioactive decay and to have similar count statistics as the first experiment.

Data acquisition and reconstruction were based on the clinical protocol using one bed position according to the EANM guidelines [12]. All studies were performed with a SPECT/ CT dual head system (Discovery NM/CT 670 Pro, GE Healthcare, Milwaukee, Wisconsin, USA). The SPECT measurements are acquired using a low-energy, high-resolution (LEHR) collimator that was positioned in L mode, noncircular orbit, step-and shoot mode and 60 (2×30) views. The technetium energy window (photopeak) was set on 140.5 keV (window: $\pm 10\%$) for emission and on 120 keV (window: $\pm 5\%$) for scatter. The camera sensitivity was determined as recommended by the vendor [6] as described in more detail in Collarino et al. [7]. After the SPECT acquisition, a low-dose CT scan (120 kV, 20 mAs, pitch: 0.938, collimation: 16×1.25) was acquired for attenuation correction purposes.

All SPECT data were reconstructed using Evolution with compensation for collimator-detector response, resolution recovery, attenuation and scatter on a matrix of 64×64 voxels with 1.5 zoom, resulting in a voxel size of $5.89\times5.89\times5.89$ mm³. Moreover, the CT data were reconstructed using adaptive statistical iterative reconstruction (ASIR, GE healthcare) with a voxel size of $0.98\times0.98\times5.00$ mm³.

Based on the recommendations of the vendor no post-reconstruction filter should be applied for quantification [6]. However, a Butterworth filter (cut-off frequency of 0.52cycles/cm and an order of 5) was recommended by the vendor for clinical SPECT/CT cardiac studies without quantification. Therefore, SPECT data were reconstructed both with and without a Butterworth filter to investigate the impact of post-filtering on quantification. After reconstruction, the Q.Metrix package resampled both the CT and SPECT images to an equivalent and isotropic voxel size (1.47 \times 1.47 \times 1.47 mm³) that was used for delineation.

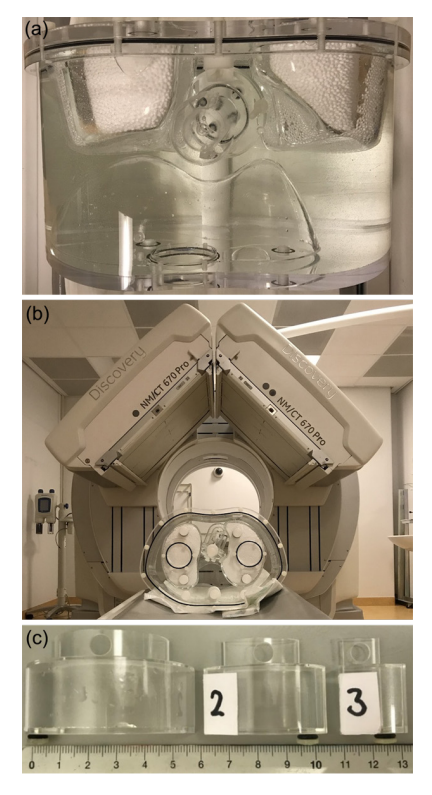


Figure 1. Axial view of an anthropomorphic torso phantom containing a cardiac insert, spine, lungs and liver (a). Positioning of the phantom on the SPECT/CT scanner (b). Three defects with various sizes and scale in cm (c).

Data Analysis

All SPECT/CT images were converted from counts to Bq/mL using Q.Metrix as detailed in the paper of Collarino *et al.* [7]. To determine the number of iterations that are required for Evolution to converge, volumes of interest (VOI) were drawn on CT images for the background, liver, small defect and myocardium compartments. Evolution was considered

to have converged when for each VOI the relative difference in the activity concentration of the iteration was less than 1% with respect to the previous iteration. In order to determine the noise level, the coefficient of variation (COV) in the background compartment was calculated by the standard deviation divided by the mean activity concentration.

Interobserver reliability of delineation on CT images was assessed by three physicians that draw VOIs on the small defect and the myocardium for the S-configuration. The interobserver reliability was computed by an intraclass correlation coefficient using a two-way mixed effects model for absolute agreement (ICC $_A$) (SPSS statistics; version 25; IBM Statistics, Armonk, USA). ICC scores range from 0 to 1, representing a level of agreement: \leq 0.40 poor to fair, 0.41–0.60 moderate, 0.61–0.80 substantial, 0.81–1.00 almost perfect [13].

Subsequently, recovery coefficients (RC), representing the ratio between the reconstructed activity concentration (in Bq/mL) and the true activity concentration as measured with a dose calibrator (VIK-202, Comecer, the Netherlands), were computed for VOIs drawn on CT images for the myocardium and defect compartments for all configurations. Here an RC of 1 indicates that injected activity concentration was in accordance with the measured activity concentration. Furthermore, for all six configurations separately, the precision was expressed in average repeatability deviation (RD) calculated by the standard deviation (SD) of the myocardium RCs as a percentage of the mean myocardium RC. Moreover, Bull's eye plots with 17 segments were generated using 4DM (INVIA-Ann Arbor, MI, USA) for the S- and GT-configurations.

Patient cases

Patient cases were evaluated retrospectively to illustrate the clinical applicability of the phantom study. For patients with CAD and ischemia without long-term treatment options, intramyocardial injection of autologous bone marrow cells (BMC) has emerged as an alternative treatment strategy at Leiden University Medical Center (LUMC) [14]. SPECT/CT data were composed before and after BMC injection. The collected patient data were anonymized and recorded in a database. Performance of this retrospective study was approved by the medical ethical review board and the requirement to obtain informed consent was waived.

Comparing the MPS at rest and after stress, areas of under-perfusion and resultant stress-induced ischemia were identified. According to a two-day protocol, as described in the EANM guidelines, patients under and over 100 kg received 500 and 750 MBq ^{99m}Tc-tetrofosmin, respectively, for both the stress and the rest examination [12]. All patients

underwent a pharmacologic adenosine stress examination. SPECT/CT was acquired 30-45 minutes post-injection after stress and 45-60 minutes post-injection during rest.

All stress and rest studies were converted into lean-body mass standardized uptake values (SUV_{LBM}) in g/mL and calculated as described in Kim et al. [15]. Reversibility Bull's eye plots were composed for the studies before and after BMC injection as used in clinical practice [12]. Subsequently, the difference in tracer uptake (SUV_{LBM}) prior to and after BMC injection was calculated by the reversibility Bull's eye plots after BMC injection minus before BMC injection.

Statistical Analysis

Statistical analysis was performed using SPSS statistics software and Excel (version 2017; Microsoft, Redmond, USA). A Shapiro-Wilk test was performed in order to evaluate the (log)normality of the data. Paired data for both the phantom and the patient study were statistically performed with the paired T-test or Wilcoxon Signed Rank test depending on the (log)normality. The statistical analyses of the non-paired data were performed with an independent T-test or Mann-Whitney U depending on the (log)normality. Continuous data were expressed as mean(SD).

RESULTS

Phantom study

Camera sensitivity, convergence and noise level

The camera sensitivity was 74.0 cps/sec/MBq. Evolution showed convergence for all investigated VOIs when at least 7 iterations (and 10 subsets) were applied (Figure 2). Moreover, an increasing noise level (COV) was shown with increasing number of iterations. With 7 or more iterations the filtered data showed a lower noise level compared to the unfiltered data. At 7 iterations the COV was 44.3% and 44.5%, with and without Butterworth post-filtering, respectively. For the remainder of the study, all data were reconstructed using 7 iterations and 10 subsets.

Interobserver variability

Almost perfect agreement between the observers was obtained when the small defect and myocardium were delineated manually on CT images (ICC_A: \geq 0.863 and \geq 0.839, respectively).

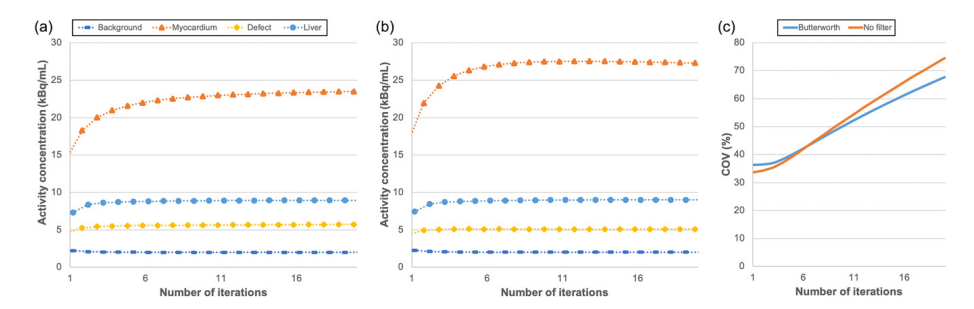


Figure 2. Effects of increasing the number of iterations for Evolution on the reconstructed activity concentrations of background, myocardium, small defect and liver compartments, obtained with (a) and without (b) Butterworth post-filtering, and on (c) COV derived from the background compartment.

Recovery coefficients for myocardium compartment

RC for the filtered data was significantly lower compared to the unfiltered data (p<0.05, Table 1). All mean RC were significantly smaller (up to 0.3 in mean RC) for the filtered data compared to the unfiltered data. However, SD values were similar with and without filtering in all configurations. No significant difference was shown between filtered RD and unfiltered RD (p>0.05). The largest RD (5.53 and 5.41 with and without Butterworth filtering, respectively) was depicted for the GT configuration and the smallest RD (1.18 and 1.53 with and without Butterworth filtering, respectively) for the configuration with the two small defects.

Table 1. Mean recovery coefficient (RC), SD and repeatability (RD), obtained with and without Butterworth post-filtering, derived from the myocardium compartment for various configurations.

	No filter			Butterworth		
Configuration	RC	SD	RD	RC	SD	RD
S	0.67	0.02	3.51	0.64	0.02	2.72
М	0.63	0.01	1.59	0.61	0.01	1.41
L	0.62	0.03	4.91	0.59	0.03	4.35
SS	0.60	0.01	1.53	0.58	0.01	1.18
SM	0.63	0.01	1.96	0.61	0.01	2.26
GT	0.63	0.03	5.41	0.61	0.03	5.53
Mean			3.15			2.91

Recovery coefficients for defects

Filtered data showed a significantly lower mean(SD) RC over all defect volumes compared to the unfiltered data with 0.63(0.05) and 0.70(0.07), respectively (p<0.05; Figure 3). The variability between the acquisitions with the same configuration was, however, significantly (p<0.05) larger in the unfiltered data (maximum RD difference of 2.74% between filtered and unfiltered data). In addition, various similar patterns were seen in both graphs. First, the mean RC values in smaller defect volumes were lower compared to larger defect volumes with 0.65 and 0.72 for the unfiltered data and 0.64 and 0.71 for the filtered data, respectively (p<0.05). Second, smaller defect volumes yielded larger variations between the repetition measurements with maximum RD values of 12,4% and 10,4% for unfiltered and filtered data, respectively. Third, the apical defects showed significantly (p<0.05) lower RC values compared to the basal defects, with RC values of 0.32 and 0.60 for the unfiltered data and 0.32 and 0.53 for the filtered data. Finally, a large variation between the two small defects was found.

Bull's eye plots variability

There was significant difference (p<0.05) between the filtered and unfiltered uptake per segment for both the GT- and small SS-configuration (Figure 4). However, the filtered data showed more homogenous uptake in the myocardium. The unfiltered data showed a more heterogeneous pattern and showed more areas of less uptake that do not contain defects, and therefore the filtering was applied to the images in the remainder of this study. For the S-configuration, the smallest uptake (kBq/mL) was observed in the mid anterior segment, which contained the defect. Mean activity concentration per segment for this configuration with and without post-filtering is depicted in Supplemental Fig. S1.

Patient cases

As a result of the phantom study, 7 iterations (and 10 subsets) and Butterworth post-filtering was applied for the image reconstruction of ten patient cases recruited for BMC injection between February 2017 and May 2019. Patient characteristics are summarized in Table 2. The average global tracer uptake in the myocardium (in kBq/mL), depicted in Table 2, was within the same range as the average global tracer uptake applied to the myocardium in the phantom study (Figure 4; range: 14.9-43.1 and 35.0-38.5, respectively). Furthermore, the minimum segmental tracer uptake was in the same range as the tracer uptake applied to the defect in the phantom study (Table 2; range 6.5-33.5 kBq/mL and Figure 4; 25 kBq/mL, respectively). The median time between the SPECT/CT scans before and after BMC injection was 9 months. Association between the reversibility Bull's eye plots in SUV_{LBM} before and after BMC injection is provided in Table 3. Eight patients showed significant difference (p<0.05) in SUV_{LBM} between before and after the injection with a maximal improvement of 2.22 g/mL (patient no.7).

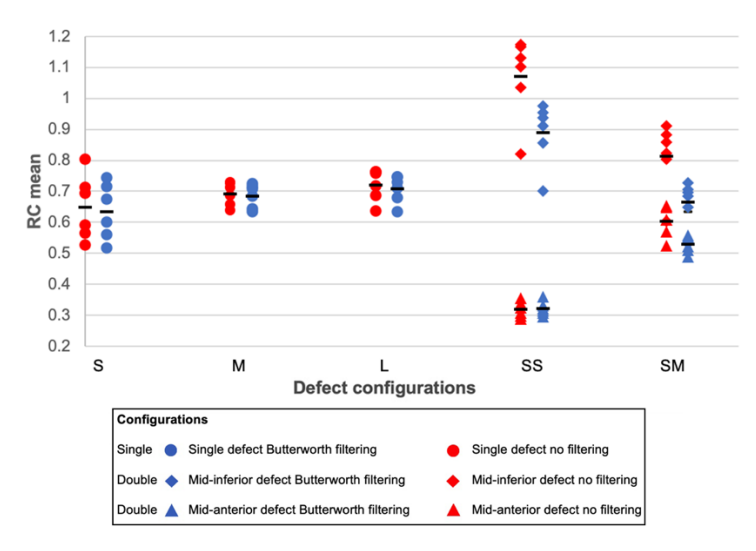


Figure 3. Recovery coefficients (RC) of single and two defects: small (S), 2.6 mL; medium (M), 5.6 mL; and large (L), 11.8 mL. The defect RC of Evolution with (blue) and without Butterworth post-filtering (red). Moreover, RC mean of the defect was illustrated separately for the SS and SM-configurations.

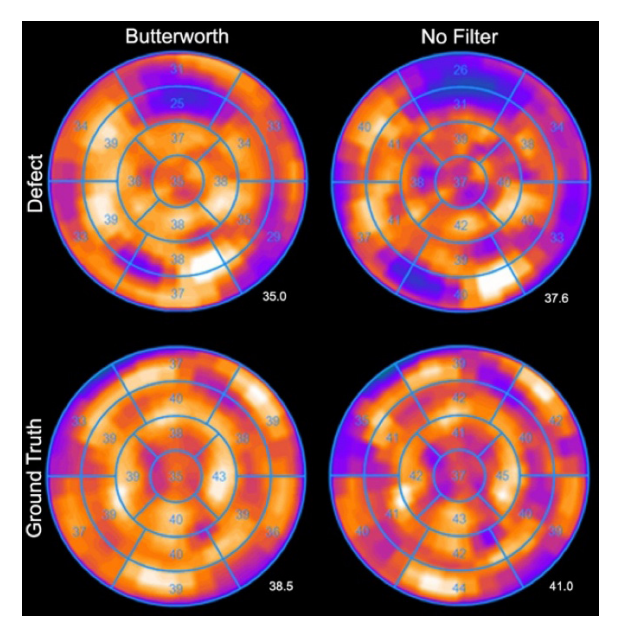


Figure 4. Bull's eye plots of Butterworth filtered data (left panel) and unfiltered data (right panel). The values are in kBq/mL and depict one acquisition of the S-configuration with the defect in the mid-anterior segment (top) and ground truth (bottom). The number right below the Bull's eye plot concerns the average global tracer uptake in kBq/mL.

Table 2. Patient characteristics (n=10). Table shows median and range.

Characteristic	Value
Gender	
Male	9
Female	1
Age (y)	69 (53-82)
Weight (kg)	82 (46-124)
Height (cm)	176 (160-187)
Time delay between BMC injection and imaging (mo.)	3 (1-13)
Activity received for MPS	
~500 MBq	8
~750 MBq	2
Average global tracer Uptake (kBq/mL)	
Before BMC injection rest	25.7 (14.9-33.1)
Before BMC injection stress	27.3 (19.3-37.5)
After BMC injection rest	25.5 (18.6-43.1)
After BMC injection stress	30.1 (19.5-41.2)
Minimum segmental tracer Uptake (kBq/mL)	
Before BMC injection rest	20.4 (7.2-27.8)
Before BMC injection stress	17.8 (6.5-29.1)
After BMC injection rest	19.3 (8.1-33.5)
After BMC injection stress	21.0 (8.4-27.8)
Medical History	
CABG	10
PCI	6
MI	4
ICD	1
BMC injection	2
PM	0
Medication	
Diuretics	3
Beta-blockers	10
Scanned Bed position	
Prone position	7
Supine position	3

Table 2. Patient characteristics (n=10). Table shows median and range. (continued)

Characteristic	Value
Ejection fraction (%)	
Rest Before BMC	55 (24->60)
Stress Before BMC	52 (21->60)
Rest After BMC	55 (25->60)
Stress After BMC	52 (21->60)

BMC: bone marrow cell; SPECT/CT single photon emission computed tomography/computed tomography; MPS: myocardial perfusion scintigraphy; CABG: coronary artery bypass grafting: PCI: percutaneous coronary intervention; MI: myocardial infarction; ICD: implantable cardioverter defibrillator; PM: pacemaker.

Table 3. Association between the relative mean difference (range), derived from reversibility Bull's eye plots, in SUV_{IBM} (g/mL) before and after BMC injection.

Patient			
no.	Pre treatment	Post treatment	p-value
1	0.60(0.10 – 1.25)	0.19(-0.26 - 0.64)	0.001
2	-0.55(-1.30 - 0.19)	0.19(-0.89 – 1.10)	0.001
3	-0.74(-1.52 – 0.12)	0.32(-0.70 – 0.91)	<0.001
4	0.75(0.04 – 1.59)	-0.42(-1.07 - 0.23)	<0.001
5	-1.11(-1.620.67)	-0.03(-0.68 - 0.45)	<0.001
6	0.48(-0.09 - 1.16)	0.17(-0.55 – 0.98)	0.093
7	-0.55(-1.13 – 0.14)	1.67(0.62 – 2.39)	<0.001
8	-0.44(-1.03 – 0.08)	-0.38(-0.67 –0.14)	0.586
9	-1.13(-1.690.66)	-0.30(-0.82 –0.38)	<0.001
10	2.06(0.98 – 2.53)	-0.54(-1.63 - 0.68)	<0.001

DISCUSSION

To the best of our knowledge, this is the first study that evaluated Evolution for cardiac applications. The experimental part of this study evaluated the accuracy and precision of Evolution by utilizing various phantom experiments. To illustrate the feasibility of clinical application, ten patients, before and after BMC treatment, were included retrospectively. 7 iterations (10 subsets) and Butterworth post-filtering (cut off frequency 0.52in cycles/cm, order of 5) were considered optimal for reconstruction based on convergence and noise level. Applying these settings, the average repeatability deviation (or precision) of all

acquisitions was 2.91%. Moreover, the accuracy of Evolution using larger defects resulted in higher RC values (ranging from 0.64 to 0.75) compared to smaller defects (RC ranging from 0.52 to 0.74). Bull's eye plots were generated to evaluate the uptake per segment.

RC values determined for both myocardium and defect were in general underestimated (i.e. <1), except for the SS-configuration (Table 1 and Figure 3). This underestimation is likely a result of partial volume effects. The spatial resolution of the system with a LEHR collimator is 7.4 mm full-width-at-half-maximum (FWHM) [16]. The resolution-modelling in Evolution has a positive effect on resolution, which resulted in an increment from 7.4 mm FWHM to 5.1-6.4 mm FWHM[16]. However, our results might differ since the resolution-modelling in Evolution is based on bone applications performed with LEHR collimators in H-mode and hence this provides only an indication of the improved spatial resolution for cardiac applications. Hypothetically, smaller defects are more affected by the spill-in effect of neighboring tissues, like the myocardium, resulting in higher recovery. However, the thickness of the myocardial wall (~10 mm), producing the spill out effect, might explain the lower RC values. Similar results were reported in a cardiac phantom study [17] and a bone phantom study using the same SPECT/CT camera [8]. In addition, modelling the collimator detector response might also clarify the decrease in quantitative accuracy, since this is acknowledged to introduce blurring in the final reconstruction of SPECT data [18]. Furthermore, the findings showed higher accuracy in larger defects (11.8 mL) compared to smaller defects (2.6 mL), possibly explained by these partial volume effects. However, both defect size and SUV_{IBM} uptake (relative and absolute) are of clinical interest for accurately assessing response to treatment in patients with CAD. Therefore, the investigation of the spill-in and spill-out due to partial volume effects remains of interest for future cardiac SPECT studies.

The observed inhomogeneity (artefacts) in the Bull's Eye plot might lead to difficulties in interpretation and may affect the quantitative treatment evaluation of MPS. Butterworth filtered data demonstrated a more homogeneous uptake compared to unfiltered data (Figure 4), despite the comparable noise levels (Figure 2C), and is therefore preferred. However, the recent quantification with Evolution was developed for the quantification of "hot spots" in mainly bone, lung and liver applications, while uniformity and contrast are more important to quantify defects (cold spots) for cardiac applications. A previously designed Evolution for (non-quantitative) cardiac applications combines the maximum a posteriori (MAP) algorithm [19] with the one-step-late (OSL) algorithm using a Green prior and median root prior (last iteration only) [20] to suppress formation of hot spots due to noise in the acquired projections. Therefore, it would be worthwhile to investigate a new variant of Evolution that combines quantification (compensation for collimator–detector response, attenuation and scatter correction, and resolution recovery) with MAP and OSL for quantitative cardiac applications.

This study contains some limitations. First, no dedicated dynamic cardiac phantom was used in this experimental study. Therefore, the effects of cardiac motion, a challenge among cardiac scanning, causing artefacts and distortions in image datasets, could not be investigated [21]. Second, only Evolution was used for quantitative SPECT, hence no performance comparison could be made with other quantification software packages such as SUV SPECT (Hermes Medical Solutions, Stockholm, Sweden). Third, the reported results are specific to one vendor and one implementation of iterative reconstruction.

Finally, the goal of the patient cases was to illustrate the clinical applicability of quantitative SPECT in the current MPS clinical workflow for response monitoring. This feasibility study showed that it was possible to apply the phantom settings to clinical patient data and generate Bull's eye plots in SUV_{LBM}. Significant differences in SUV_{LBM} on the scan prior to and after BMC injection were found in eight patients, indicating that BMC injection has had an effect that led to a change in tracer uptake. The other two patients showed no significant difference. This implies that no change in uptake occurred after BMC injection. However, larger sized prospective clinical trials should be executed for validation and implementation of this technique and in order to investigate the accuracy, clinical applicability and clinical value of quantitative SPECT for therapy response monitoring in patients with CAD.

CONCLUSION

Quantification of ^{99m}Tc related SPECT/CT for response monitoring in patients with CAD seems feasible when 7 iterations (10 subsets), Butterworth post-filtering and manual delineation on CT images are used. To show sufficient evidence for the use of Evolution in clinical practice for treatment response monitoring, validation should take place in a future prospective clinical trial, studying a large patient cohort. Quantitative SPECT, however, is promising and might extend the diagnostic potential of standard MPI.

REFERENCES

- Metz LD, Beattie M, Hom R, Redberg RF, Grady D, Fleischmann KE. The prognostic value of normal exercise myocardial perfusion imaging and exercise echocardiography: a meta-analysis. J Am Coll Cardiol. 2007;49:227-37.
- Dewey M, Siebes M, Kachelrieß M, Kofoed KF, Maurovich-Horvat P, Nikolaou K, et al. Clinical quantitative cardiac imaging for the assessment of myocardial ischaemia. Nature Reviews Cardiology. 2020:1-24.
- Jaarsma C, Leiner T, Bekkers SC, Crijns HJ, Wildberger JE, Nagel E, et al. Diagnostic performance
 of noninvasive myocardial perfusion imaging using single-photon emission computed
 tomography, cardiac magnetic resonance, and positron emission tomography imaging for
 the detection of obstructive coronary artery disease: a meta-analysis. J Am Coll Cardiol.
 2012;59:1719-28.
- Shaw LJ, Berman DS, Maron DJ, Mancini G, Hayes SW, Hartigan PM, et al. Optimal medical therapy with or without percutaneous coronary intervention to reduce ischemic burden. Circulation. 2008;117:1283-91.
- Berman DS, Kang X, Slomka PJ, Gerlach J, de Yang L, Hayes SW, et al. Underestimation of extent of ischemia by gated SPECT myocardial perfusion imaging in patients with left main coronary artery disease. J Nucl Cardiol. 2007;14:521-8.
- 6. GE Healthcare. NM Quantification Q.Metrix for SPECT/CT package (white paper). 2017.
- Collarino A, Pereira Arias-Bouda LM, Valdés Olmos RA, van der Tol P, Dibbets-Schneider P, de Geus-Oei LF, et al. Experimental validation of absolute SPECT/CT quantification for response monitoring in breast cancer. Med Phys. 2018;45:2143-53.
- Myint T, Ekjeen T, Chaichana A, Tipparoj R, Wiyaporn K. Factors affecting standardized uptake value of 99mTc-MDP bone SPECT/CT: A phantom study. J Phys Conf Ser. 2019;1248:012026.
- Kroiss AS, Nekolla SG, Dobrozemsky G, Grubinger T, Shulkin BL, Schwaiger M. CT-based SPECT attenuation correction and assessment of infarct size: results from a cardiac phantom study. Ann Nucl Med. 2017;31:764-72.
- Jang S, Jaszczak R, Tsui BM, Metz C, Gilland D, Turkington T, et al. ROC evaluation of SPECT myocardial lesion detectability with and without single iteration non-uniform Chang attenuation compensation using an anthropomorphic female phantom. IEEE Trans Nucl Sci. 1998;45:2080-8.
- O'Connor MK, Kemp B, Anstett F, Christian P, Ficaro EP, Frey E, et al. A multicenter evaluation of commercial attenuation compensation techniques in cardiac SPECT using phantom models. J Nucl Cardiol. 2002;9:361-76.
- Verberne HJ, Acampa W, Anagnostopoulos C, Ballinger J, Bengel F, De Bondt P, et al. EANM procedural guidelines for radionuclide myocardial perfusion imaging with SPECT and SPECT/CT: 2015 revision. Eur J Nucl Med Mol Imaging. 2015;42:1929-40. doi:10.1007/s00259-015-3139-x.
- 13. Landis JR, Koch GG. The measurement of observer agreement for categorical data. Biometrics. 1977:159-74.
- Van Ramshorst J, Bax JJ, Beeres SL, Dibbets-Schneider P, Roes SD, Stokkel MP, et al. Intramyocardial bone marrow cell injection for chronic myocardial ischemia: a randomized controlled trial. JAMA. 2009;301:1997-2004.
- Kim CK, Gupta NC, Chandramouli B, Alavi A. Standardized uptake values of FDG: body surface area correction is preferable to body weight correction. J Nucl Med. 1994;35:164-7.

- Peters SMB, van der Werf NR, Segbers M, van Velden FHP, Wierts R, Blokland KAK, et al. Towards standardization of absolute SPECT/CT quantification: a multi-center and multi-vendor phantom study. EJNMMI Phys. 2019;6:29. doi:10.1186/s40658-019-0268-5.
- Ismail FS, Mansor S. Impact of Resolution Recovery in Quantitative 99mTc SPECT/CT Cardiac Phantom Studies. J Med Imaging Radiat Sci. 2019. doi:https://doi.org/10.1016/j.jmir.2019.05.007.
- Frey EC, Humm JL, Ljungberg M. Accuracy and precision of radioactivity quantification in nuclear medicine images. Semin Nucl Med. 2012;42:208-18.
- 19. Bruyant PP. Analytic and iterative reconstruction algorithms in SPECT. J Nucl Med. 2002;43:1343-58.
- Green PJ. Bayesian reconstructions from emission tomography data using a modified EM algorithm. IEEE Trans Med Imaging. 1990;9:84-93.
- 21. Fitzgerald J, Danias PG. Effect of motion on cardiac SPECT imaging: Recognition and motion correction. J Nucl Cardiol. 2001;8:701-6. doi:10.1067/mnc.2001.118694.



CHAPTER 6

Comparison between prone SPECT-based semi-quantitative parameters and MBI-based semi-quantitative parameters in patients with Locally Advanced Breast Cancer

Authors

A. van de Burgt, F.H.P. van Velden, C.L.S. Corion, A. Collarino, R.A. Valdés Olmos, F. Smit, L.F. de Geus-Oei and L.M. Pereira Arias-Bouda

Published

Molecular Imaging and Biology, 2024;26(6):926-933. DOI: 10.1007/s11307-024-01959-1

Supplementary materials

https://doi.org/10.1007/s11307-024-01959-1

ABSTRACT

Purpose

This study evaluates the semi-quantitative single-photon emission computed tomography (SPECT) parameters of prone SPECT using [99mTc]Tc-sestamibi and compares them with Molecular Breast Imaging (MBI)-derived semi-quantitative parameters for the potential use of response prediction in women with locally advanced breast cancer (LABC).

Procedures

Patients with proven LABC with a tumor ≥ 2 cm on mammography and an indication for MBI using [99m Tc]Tc-sestamibi were prospectively enrolled. All patients underwent a prone SPECT/CT at 5 min (early exam) and an additional scan at 90 min (delayed exam) after injection of 600 MBq [99m Tc]Tc-sestamibi to compose wash-out rates (WOR). All patients underwent MBI after early SPECT/CT. Volumes of interest of the primary tumor were drawn semi-automatically on early and delayed SPECT images. Semi-quantitative analysis included maximum and mean standardized uptake values (SUV $_{max}$, SUV $_{mean}$), functional tumor volume (FTV $_{SPECT}$), total lesion mitochondrial uptake (TLMU), tumor-to-background ratios (TBR $_{max}$ and TBR $_{mean}$), WOR and coefficient of variation (COV $_{SPECT}$). Subsequently, the FTV $_{SPECT}$ TBR $_{SPECT}$ and COV $_{SPECT}$ were compared to FTV $_{MBI}$ TBR $_{MBI}$ and COV $_{MBI}$.

Results

Eighteen patients were included. Early SUV_{max} , and TBR_{max} showed significantly higher interquartile range (IQR) compared to SUV_{mean} and TBR_{mean} , respectively 2.22 (2.33) g/mL, 6.86 (8.69), 1.29 (1.39) g/mL and 3.99 (5.07) (median (IQR), p<0.05). WOR showed a large IQR (62.28), indicating that there is WOR variation among the LABC patients. FTV showed no difference between MBI and early SPECT semi-quantitative parameter (p=0.46).

Conclusions

In LABC patients it is feasible to obtain semi-quantitative parameters from prone SPECT/CT. The FTV derived from early prone SPECT/CT is comparable with MBI-based FTV. Studies with comprehensive clinical parameters are needed to establish the clinical relevance of these semi-quantitative parameters, including WOR, for response prediction before its use in clinical routine.

Keywords

[99mTc]Tc-sestamibi; Locally advanced breast cancer; Response prediction; Quantitative SPECT; SPECT/CT; Molecular Breast Imaging

INTRODUCTION

Molecular Breast Imaging (MBI), also previously referred to as breast specific gamma imaging (BSGI), provides a non-invasive *in vivo* characterization of breast lesions and is proven valuable for breast cancer detection, with sensitivity comparable to Magnetic Resonance Imaging (MRI) [1]. MBI holds a fundamental position when there is a contraindication for MRI or in situations when mammography and ultrasound have limited accuracy, such as in dense breasts, with free silicone (after silicone mastopathy) [2].

The radiopharmaceutical used for MBI is [99mTc]Tc-methoxyisobutylisonitrile [99mTc]Tc-sestamibi), which has been used in nuclear breast imaging for diagnosing breast cancer for over 20 years [3, 4]. [99mTc]Tc-sestamibi has special characteristics, since it is a transport substrate for P-glycoprotein (Pgp) [5], encoded by the multidrug resistance gene that functions as energy-dependent efflux-pump for many drugs [6]. Therefore, reduced [99mTc]Tc-sestamibi uptake in tumor cells might indicate Pgp over-expression, enabling upfront prediction of chemosensitivity. Determination of [99mTc]Tc-sestamibi uptake during neoadjuvant chemotherapy (NAC) seems helpful in predicting non-responsiveness to NAC [7]. Therefore, quantification of [99mTc]Tc-sestamibi accumulation might facilitate early *invivo* assessment of tumor chemoresistance and may guide treatment decision making.

Intra-tumor heterogeneity holds potential implications for tumor progression, treatment response, and therapeutic resistance [8]. Semi-quantitative [99mTc]Tc-sestamibi parameters, as coefficient of variation (COV) and wash-out rates (WOR) [7, 9], are associated with this intra-tumoral heterogeneity [10, 11]. However, recent studies on semi-quantitative [99mTc]Tc-sestamibi parameters revealed drawbacks in accurately assessing tumor uptake with planar MBI [12-14]. Single-photon emission computed tomography combined with computed tomography (SPECT/CT) might be helpful to overcome these drawbacks. It combines three-dimensional (3D) (whole-body) imaging with functional and anatomical information, compensating for tissue attenuation and scattering using low-dose CT and provides semi-quantification using [99mTc]Tc-sestamibi [7, 15, 16]. To our knowledge, there are no clinical studies investigating the use of semi-quantitative SPECT parameters using [99mTc]Tc-sestamibi in locally advanced breast cancer (LABC) patients. This prospective feasibility study aimed to evaluate the semi-quantitative parameters of prone SPECT/CT using [99mTc]Tc-sestamibi and to compare them with MBI-derived semi-quantitative parameters for the potential use of response prediction in LABC patients.

METHODS

Study design and Patients

The Institutional Review Board approved this prospective monocenter study (trial code: NL60403.058.17). Between August 2017 and April 2019, all consecutive patients with pathologically proven LABC with a tumor ≥ 2 cm on mammography and ultrasound [16] and a clinical indication for local staging with MBI using [99m Tc]Tc-sestamibi [2] were included according to standard clinical procedures for pre-operative staging and to rule out multifocality. Although the SNMMI/EANM guideline [2] was published after our data collection, our study adhered to this. Patients who were pregnant or had undergone prior breast surgery, chemotherapy, or radiation therapy were excluded.

Data collection

SPECT/CT acquisition

Camera sensitivity was determined according to the vendor's recommendations [15] as detailed in Collarino et al. [16]. Five minutes after injection with 600 MBg [99mTc]Tcsestamibi an early SPECT/CT was acquired. A second (delayed) SPECT/CT was acquired 90 min p.i. to compose the WOR [7]. The SPECT/CT scans were performed with a dualhead SPECT/CT gamma camera (Discovery NM/CT 670 Pro, GE Healthcare, Milwaukee, Wisconsin, USA). The patient was positioned in prone position (face down and arms up) using a supporting device for hanging breasts (hanging breasts mode) utilizing a single bed position. SPECT measurements were obtained with a low-energy, high-resolution (LEHR) collimator in noncircular orbit using step-and-shoot mode, over 360° (180° per head) and a 3° angular step with an acquisition time per frame/angle of 20 s (25 min in total). A 128 x128 matrix size without zoom was applied and resulting in a voxel size of 4.42 ×4.42 ×4.42 mm³. The technetium energy window (photopeak) was set at 140.5 keV (window ±10%) for emission and 120 keV (window ±5%) for scatter. Consecutively, a lowdose CT was acquired for attenuation correction purposes with the patient breathing normally. The acquisition parameters include a tube voltage of 100 kV, a pitch of 1.375, a collimation of 20 mm and auto tube current modulation of 100 mA (30-150 mA).

All SPECT data underwent reconstruction using Evolution with Q.Metrix available on a Xeleris workstation version 4.DR (GE Healthcare, Milwaukee, USA) with an ordered subset expectation maximization (OSEM) algorithm that incorporates compensation for collimator-detector response, resolution recovery, attenuation, and scatter, using 9 iterations and 10 subsets [16]. The reconstructed voxel size of the SPECT images was 2.21 \times 2.21 \times 2.21 mm³. Additionally, CT data were reconstructed using an adaptive statistical iterative reconstruction (ASIR, GE Healthcare) algorithm with a voxel size of 2.21 \times 2.21 mm³.

MBI acquisition

MBI was acquired directly after the early SPECT/CT scan according to standard procedure of our center [17]. Patients, while being seated, underwent five MBI (Dilon Diagnostics 6800, Pittsburgh, PA, USA) acquisitions (craniocaudal and mediolateral oblique of both breasts and lateral of the breast with tumor) of one frame with an acquisition time of 480 seconds (8 minutes) and a matrix size of 80×80 , resulting in planer images with pixels of 3.20×3.20 mm.

Image analysis

SPECT/CT semi-quantitative parameters

SPECT/CT images were converted from counts to Bq/mL using Q.Metrix as previously detailed [16]. Volume of interest (VOI) of the primary tumors were semi-automatically delineated using a 42% threshold iso-contour method, followed by manual assessment by researcher (AB) to ascertain visual conformity [16]. Furthermore, approximately 3 cm diameter VOIs were manually drawn in the contralateral healthy breast and were used to estimate background activity. These VOIs were automatically projected to the co-registered SPECT images. Subsequently, the body-weighted mean, minimum and maximum standardized uptake values (SUV $_{mean}$, SUV $_{max}$; in g/mL), standard deviation (SD) of the mean SUV (in g/mL) and functional tumor volume (FTV; in mL) were measured. Furthermore, the total lesion mitochondrial uptake (TLMU = FTV × SUV $_{mean, tumor}$), tumor-to-background ratio's (TBR $_{max}$ = $\frac{SUV}{SUV}_{mean, tumor}$ and TBR $_{mean}$ = $\frac{SUV}{SUV}_{mean, tumor}$) and the washout rate (wor = $\frac{TBR_{early} - TBR_{late}}{TBR_{early}} \times 100\%$) were composed [16, 18]. Next to these parameters, the coefficient of variation (Cov $_{SPECT}$ = $\frac{SDSUV}{SUV}_{mean, tumor}$ × 100%) within the tumor was calculated to quantify a degree of tumor heterogeneity.

MBI semi-quantitative parameters

Quantification of [99mTc]Tc-sestamibi uptake on MBI images was performed in Picture Archiving and Communication System (PACS; Sectra IDS7, Linköping, Sweden). Manual tumor delineations were performed on the MBI data by an experienced nuclear medicine physician (LP). An estimation of the FTV_{MBI} was acquired by performing manual tumor diameter delineations in three perpendicular axes (a,b,c) yielding: FTV_{MBI} = $\frac{4}{3} \times \pi \times a \times \frac{1}{2} \times b \times \frac{1}{2} \times c \times \frac{1}{2}$. The number of counts was obtained in three directions (cranial-caudal, mediolaterale-oblique and lateral) and the average was calculated. The counts in the background were determined by drawing a 3 cm diameter circle in the contralateral breast on the craniocaudal and mediolateral oblique projections.

The TBR on MBI was calculated in two ways. First, the TBR (TBR_{max}) was calculated by dividing the maximum pixel value in the tumor by the highest mean pixel value of the background, in line with the SPECT TBR calculations. Secondly, the TBR (TBR_{ave}) was

calculated by dividing the average maximum pixel value of the tumor by the average pixel value of the background [9].

There are currently no standardized clinical protocols for calculating COV_{MBI} . Therefore, COV_{MBI} was calculated in three ways in line with literature. The COV_{max} was calculated by dividing the highest SD in the tumor by the highest mean value in the tumor, multiplied by 100%. Secondly the COV_{ave} was calculated by dividing the average SD in the tumor (SD_{ave}) by the average of the mean value in the tumor multiplied by 100%. Moreover, the COV_{norm} was calculated based on literature by (SD_{ave})/[(mean pixel value of tumor)/(average value of the background)] [10, 11].

Statistical analysis

A Shapiro-Wilk test was performed to evaluate the normality of the data. Non-paired data were analyzed with either an independent T test or Mann-Whitney U test, and continuous data were presented as mean (SD) or median (interquartile range), depending on normality. Paired data analysis used either the paired T-test or Wilcoxon Signed Rank test, also depending on normality. Box plots were used to visualize the distribution of the SPECT-based semi-quantitative parameters and the MBI-based semi-quantitative parameters. Scatter plots and the Spearman's Rank correlation coefficient were used to explore their relation ranging from strong negative consistent relationship (-1), no consistent relationship (0) to strong positive consistent relationship (+1). Statistical analysis was conducted using GraphPad Prism (version 9.3.1; GraphPad Software, San Diego, California, USA) and Excel (version 2023; Microsoft, Redmond, USA).

RESULTS

Patient characteristics

This observational prospective study initially included 18 patients. Written informed consent was obtained from all participants. Patients' characteristics are shown in Table 1.

Semi-quantitative parameters

SPECT

The semi-quantitative parameters of early and delayed SPECT acquisitions were calculated to assess the wash-out of [99m Tc]Tc-sestamibi (Figure 1 and Supplementary Table S1). The delayed acquisition was not performed for one patient due to technical difficulties. Early SUV_{max}, and TBR_{max} showed significantly higher interquartile range (IQR) compared to SUV_{mean} and TBR_{mean}, respectively 2.33(2.33) g/mL, 6.86(8.69), 1.29(1.39) g/mL and 3.99 (5.07) (median(IQR), p<0.05). Note that WOR showed a large IQR (62.28),

indicating that there is WOR variation among the LABC patients, see Figure 1 and Supplementary Figure S1.

MBI

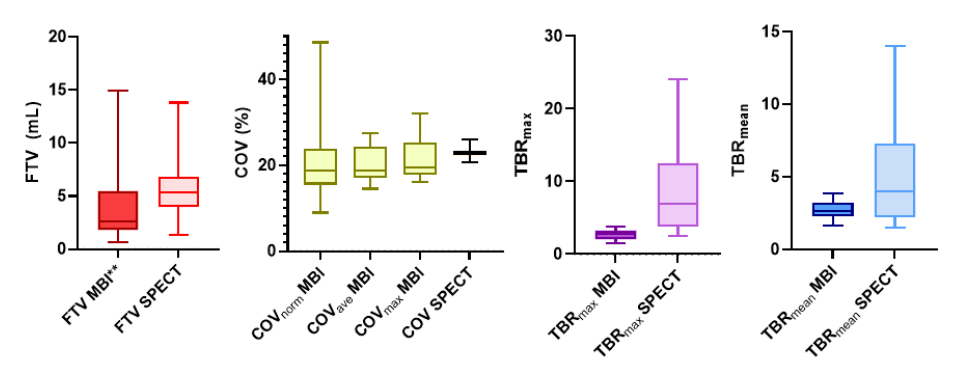
The MBI semi-quantitative parameters are presented in Figure 1 and Supplementary Table S2. The FTV $_{\rm MBI}$ calculation was not possible for four patients because either the tumor was not completely within the field-of-view (located close to the chest wall) or the tumor had diffuse growth, making realistic volume dilations unfeasible. There was no significant difference between TBR $_{\rm max}$ and TBR $_{\rm mean}$ ($p \ge 0.05$). The COV $_{\rm ave}$ showed the smallest IQR of 7.39% compared to COV $_{\rm max}$ and COV $_{\rm norm}$, respectively, 7.60% and 8.28% and was compared with COV $_{\rm SPECT}$ in the remainder of the study.

Table 1. Patients' characteristics

Variable	N=18
Age (Y)	56.2 (10.3)
Tumor type	
NST	12
Lobular	6
Grade	
1	1
2	14
3	3
Size (mm)	24.8 (8.3)
Hormone receptor	
ER	16
PR	15
HER-2	0
TN	2

 $\label{eq:special} \textit{Age and size are presented in Mean (SD)}. \textit{ NST= no special type; ER=estrogen receptor; PR=progesterone receptor; HER-2=human epidermal growth factor receptor 2; TN=triple negative}$

MBI and SPECT semi-quantitative parameters



SPECT only semi-quantitative parameters

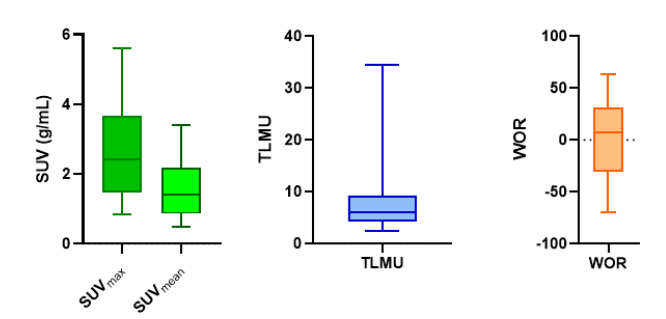


Figure 1. Semi-quantitative parameters SPECT and molecular breast imaging (MBI). The boxplots display the median (central line), 25th and 75th interquartile range (edges of the box), and the whiskers extending to the smallest and largest value for each semi-quantitative parameter. All patients underwent a prone SPECT/CT at 5 min (N=18, early exam) and an additional scan at 90 min (N=17*, delayed exam) after injection of 600 MBq [^{99m}Tc]Tc-sestamibi to compose wash-out rates (WOR). MBI was acquired directly after the early SPECT/CT to directly compare the semi-quantitative parameters of both modalities. WOR varied significantly among patients as reflected by the large interquartile range. SPECT=single photon emission computed tomography; SUV=standardized uptake value; FTV=functional tumor volume; TLMU=total lesion mitochondrial uptake; TBR=tumor to background ratio. COV=coefficient of variation within the tumor.

^{*}The delayed acquisition was not performed for one patient due to technical difficulties.

^{**}FTV_{MBI} data of four patients were excluded because the tumor was not completely within the field-of-view (located close to the chest wall) or the tumor showed diffuse growth, making realistic volume dilations unfeasible.

Comparison SPECT and MBI

Figure 2 shows comparable high focal [99mTc]Tc-sestamibi tumor uptake in MBI and SPECT/CT images of two LABC patients. The two cases illustrate one patient with a positive WOR and one patient with a negative WOR, demonstrating a visual decrease and increase in uptake over time, respectively.

Various semi-quantitative parameters of the SPECT (early acquisition) and MBI are illustrated in Figure 3. FTV_{MBI} data of four patients were excluded as explained previously. The TBR_{max} and TBR_{mean} revealed a significant difference (p<0.05) between MBI and SPECT. TBR_{mean} showed a smaller median difference compared to TBR_{max} respectively 1.34 and 4.12. The whiskers of the box plots for TBR_{SPECT} (mean and max) were significantly larger (p<0.05) than those for TBR_{MRI}, indicating greater variability of measurements for SPECT compared to MBI (Figure 1). Spearsman's correlation coefficient revealed a significant positive (r=0.7, p<0.05) consistent relation between MBI and SPECT, indicating that TBR_{SPECT} values were consistently higher compared to TBR_{MRI} (Figure 3). FTV_{SPECT} did not show a significant (p=0.46) difference compared to FTV_{MRI} The median difference between FTV_{SPECT} and FTV_{MBI} was 2.80 mL and the scatter plot indicated a diagonal trend, suggesting that the two methods provide comparable measurements. One patient showed a FTV higher than 10 mL compared to the others (approximately 5 mL). COV_{SPECT} were significantly larger (p<0.05) compared to COV_{MBI ave} and the variability in COV was significantly higher (p<0.05) for MBI compared to SPECT (Figures 1 and 3). However, visually, the values are comparable between the two techniques (Figure 3). Spearman's rank correlation from FTV and COV between MBI and SPECT was not significant ($p \ge 0.05$).

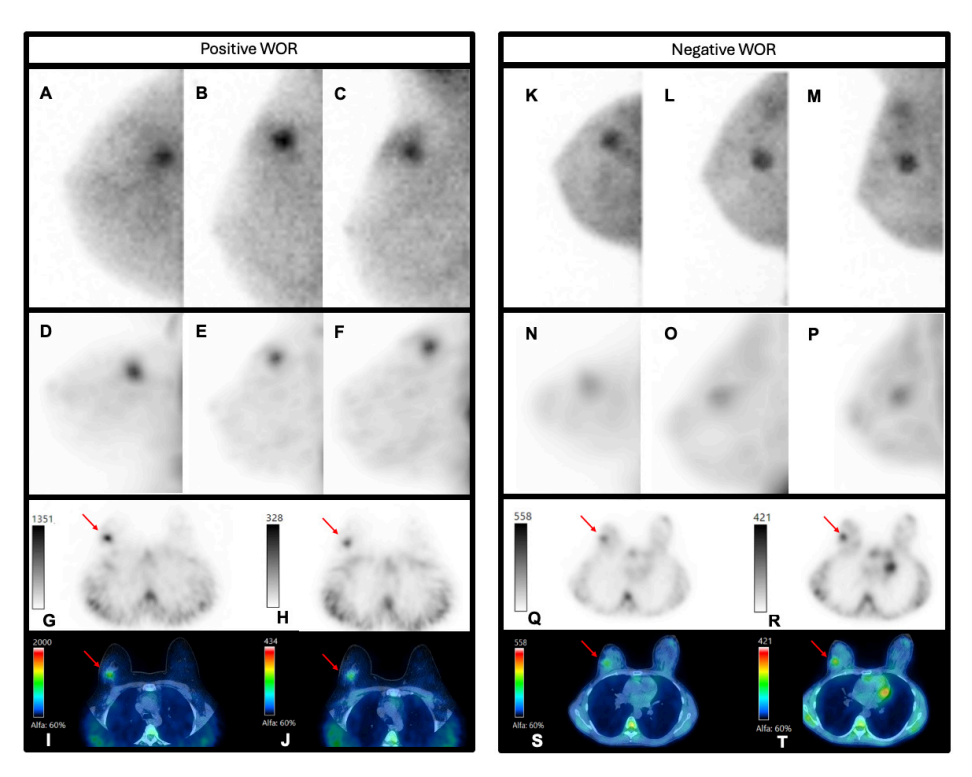


Figure 2. Molecular breast imaging (MBI) and single-photon emission computed tomography combined with computed tomography (SPECT/CT) images of two patients The first patient (A to G) is a 45-year-old woman with invasive ductal carcinoma grade 3, estrogen receptor-negative, progesterone receptor-negative, and HER2-negative (triple-negative), MBI and SPECT/CT show high focal [99mTc]Tc-sestamibi uptake of a 2 cm in diameter tumor located in the lateral upper quadrant of the right breast (red arrow) with visual lower uptake on delayed SPECT/CT and wash-out rate (WOR) of 18. The second patient (K to T) is a 43-year-old woman with invasive ductal carcinoma grade 3, estrogen receptor-positive, progesterone receptor-positive, and HER2-negative, MBI and SPECT/CT show moderate focal [99mTc]Tc-sestamibi uptake of a 2 cm in diameter tumor located in the lateral upper quadrant of the right breast (red arrow) and visual increased uptake on the delayed images (WOR -33). MBI right craniocaudal view (A and K), MBI right lateral oblique view (B and L), MBI right mediolateral view (C and M), SPECT maximum intensity projection (MIP) right craniocaudal view (D and N), SPECT MIP right lateral oblique view (E and O), SPECT MIP right mediolateral view (F and P), axial SPECT of early (G and Q), and delayed (H and R) acquisition, fused axial SPECT/CT images of early (I and S) and delayed (J and T) acquisition.

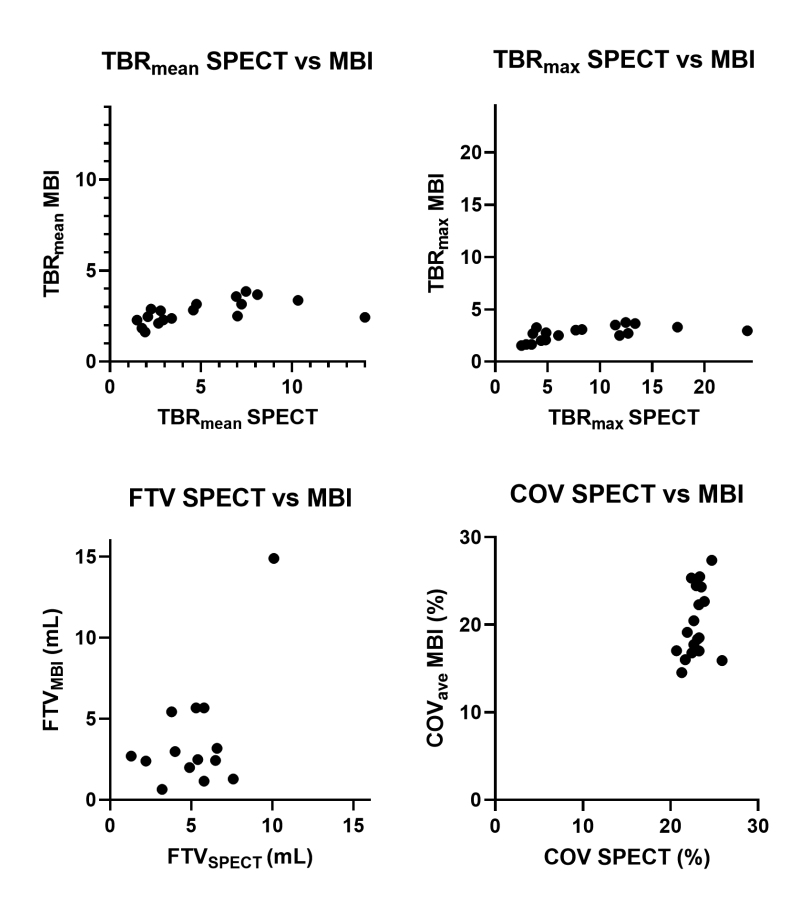


Figure 3. Scatter plots of SPECT versus MBI semi-quantitative parameters (N=18). FTV=functional tumor volume; MBI=molecular breast imaging; SPECT=single photon emission computed tomography; COV=covariant of variation within the tumor; TBR=tumor to background ratio. Note that FTV_{MBI} data of four patients were excluded because the tumor was not completely within the field-of-view (located close to the chest wall) or the tumor showed diffuse growth, making realistic volume dilations unfeasible.

DISCUSSION

To our knowledge, this is the first feasibility study evaluating the semi-quantitative parameters of prone SPECT/CT using [99m Tc]Tc-sestamibi and comparing them with MBI-based semi-quantitative parameters in 18 patients with LABC. This study presents the first step towards a possible application of semi-quantitative parameters of prone SPECT/CT in LABC patients for prediction of response to NAC. Various semi-quantitative parameters were composed for early and delayed SPECT acquisitions (5 min p.i and 90 min p.i.) and MBI. No significant difference was observed between MBI and early SPECT semi-quantitative parameter FTV (p=0.46). TBR $_{mean}$ and TBR $_{max}$ were significantly higher for SPECT compared to MBI and showed greater variability between the measurements (p<0.05).

Early SUV and TBR_{SPECT} values were higher compared to late SUV and TBR_{SPECT} , which probably is related to the clearance of [[99mTc]Tc-sestamibi via transmembrane transporter proteins (like P-gp and the multidrug resistance protein (MRP)). In this regard, [99mTc]Tc-sestamibi WOR is a promising predictive parameter for tumor non-responsiveness to NAC, as it reflects tumor multidrug resistance. Sciuto et al. reported high sensitivity and specificity for prediction of chemoresistance when applying a cut off WOR of 45% [19]. We were able to compose WOR derived from early and delayed SPECT/CT for potential future use in therapy response prediction.

The difference between $FTV_{\text{\tiny MRI}}$ and $FTV_{\text{\tiny MRI}}$ might be explained by the $FTV_{\text{\tiny MRI}}$ calculations assuming a spherical tumor, while in clinical practice, tumors exhibit various shapes. $\mathsf{FTV}_{\mathsf{MRI}}$ data of four patients were excluded because the tumor was not completely within the field-of-view (located close to the chest wall) or the tumor showed diffuse growth, making realistic volume dilations unfeasible. These encountered limitations of MBI confirm the existence of challenges in achieving accurate tumor volume measurements when using MBI [12-14]. The increased variation between MBI and SPECT in tumors with higher average $\mathsf{TBR}_{\mathsf{max}}$ and $\mathsf{TBR}_{\mathsf{mean}}$ values might be attributed to the absence of attenuation and scatter correction in MBI compared to SPECT. Photon counts within tumor's VOI are affected by surrounding tissue (axilla e.g.), tumor specifications, breast properties, and imaging settings [14]. Consequently, the same tumor may appear differently across different views or detectors, resulting in variations in VOI measurements, which might affect the TBR calculations. Moreover, the lower $\mathsf{TBR}_{\mathsf{MBI}}$ values are likely due to the higher septal penetration occurring by virtue of the 'near' contact imaging of the breast compared to the SPECT imaging. Therefore, the strengths of SPECT over MBI lie in its capacity for 3D imaging, especially for tumors located close to the chest wall and the clinical available SPECT attenuation and scatter correction, potentially composing more precise semi-quantitative parameters.

This study contains limitations. First, the limited number of subjects constitutes a major limitation and hence our results should be interpreted carefully. Although our study concerns only a small study population, we believe that our findings exhibit the complexity of assessing semi-quantitative SPECT/CT parameters and contribute to the knowledge of the application of [99mTc]Tc-sestamibi for response prediction in LABC. A dynamic study should be conducted to evaluate which model best suits [99mTc]Tc-sestamibi quantification and to relate the obtained pharmacokinetic measures to semi-quantitative measures obtained at different time intervals, hence examining their validity in this context. Second, the 42% threshold iso-contouring was utilized for the SPECT measurements based on a phantom study [16] since no protocols were available specifying the settings for quantitative SPECT with [99mTc]Tc-sestamibi for LABC. Visual evaluation was conducted for the contouring, with manual adjustments if necessary, making delineations observerdependent and thus affecting their reproducibility. Although Collarino et al showed in a phantom study that absolute SPECT/CT quantification of breast studies using [99mTc]Tcsestamibi seems feasible (<17% deviation) when 42% threshold iso-contouring is used for delineation of tumors (≥17 mm diameter) for various TBR_{max} (ranging from 9.6 to 3.3) [16], it is not clear how this 42% threshold iso-contouring would affect other semi-quantitative parameters in patients, such as FTV. Therefore, further investigation is necessary to determine which iso-contouring methods are most relevant and reproducible for clinically relevant semi-quantitative parameters in patients before applying quantitative SPECT for LABC in clinical settings. Third, outcome measures, such as pathologically confirmed therapy response, were not incorporated in this study. Before implementing response monitoring based on semi-quantitative SPECT with [99mTc]Tc-sestamibi in clinical practice, the clinical relevance of SPECT-derived semi-quantitative parameters needs to be assessed in a future large prospective clinical trial, including histopathological response to NAC as primary outcome measure and gold standard. For this, the practice SPECT quantification guidelines [20], which were not available during our data collection but which overall principles align with our study, could be considered. Furthermore, before classifying a change in a semi-quantitative parameter as a response, it is crucial to assess its test-retest variability. Additionally, it is worthwhile investigating for which tumor molecular subtypes these parameters are more consistent.

CONCLUSION

Obtaining semi-quantitative parameters of prone SPECT/CT using [99m Tc]Tc-sestamibi in women with LABC was feasible using 42% iso-contouring. No significant difference was observed between MBI and early SPECT semi-quantitative parameter FTV (p=0.46). TBR $_{mean}$ and TBR $_{max}$ were significantly higher for SPECT compared to MBI and showed greater variability between the measurements (p<0.05). Studies with comprehensive clinical outcome parameters are needed to establish the clinical relevance of these semi-quantitative parameters, including WOR, for response prediction, before it can be implemented in standard clinical care.

REFERENCES

- Vaz SC, Oliveira C, Teixeira R, Arias-Bouda LMP, Cardoso MJ, de Geus-Oei L-F. The current role of nuclear medicine in breast cancer. The British journal of radiology. 2023;96:20221153.
- Hruska CB, Corion C, de Geus-Oei L-F, Adrada BE, Fowler AM, Hunt KN, et al. SNMMI procedure standard/EANM practice guideline for molecular breast imaging with dedicated γ-cameras. Journal of Nuclear Medicine Technology. 2022;50:103-10.
- Urbano N, Scimeca M, Tancredi V, Bonanno E, Schillaci O. 99mTC-sestamibi breast imaging: Current status, new ideas and future perspectives. Seminars in Cancer Biology. 2022;84:302-9.
- Perrone E, Collarino A, Pereira Arias-Bouda LM, den Hartog W, Garganese G, Van der Hage JA, et al. Molecular imaging to guide breast cancer surgery. Clinical and Translational Imaging. 2023:1-11.
- Piwnica-Worms D, Chiu ML, Budding M, Kronauge JF, Kramer RA, Croop JM. Functional imaging of multidrug-resistant P-glycoprotein with an organotechnetium complex. Cancer research. 1993:53:977-84.
- 6. Gottesman MM, Fojo T, Bates SE. Multidrug resistance in cancer: role of ATP-dependent transporters. Nature reviews cancer. 2002;2:48-58.
- Collarino A, de Koster EJ, Olmos RAV, de Geus-Oei L-F, Arias-Bouda LMP. Is technetium-99m sestamibi imaging able to predict pathologic nonresponse to neoadjuvant chemotherapy in breast cancer? A meta-analysis evaluating current use and shortcomings. Clinical breast cancer. 2018:18:9-18
- O'Connor JP, Rose CJ, Waterton JC, Carano RA, Parker GJ, Jackson A. Imaging intratumor heterogeneity: role in therapy response, resistance, and clinical outcome. Clinical Cancer Research. 2015;21:249-57.
- Mitchell D, Hruska CB, Boughey JC, Wahner-Roedler DL, Jones KN, Tortorelli C, et al. 99mTcsestamibi using a direct conversion molecular breast imaging system to assess tumor response to neoadjuvant chemotherapy in women with locally advanced breast cancer. Clinical nuclear medicine. 2013;38:949-56.
- Yoon H-J, Kim Y, Kim BS. Intratumoral metabolic heterogeneity predicts invasive components in breast ductal carcinoma in situ. European radiology. 2015;25:3648-58.
- Yoo J, Yoon H-J, Kim BS. Prognostic value of primary tumor SUV max on F-18 FDG PET/CT compared with semi-quantitative tumor uptake on Tc-99m sestamibi breast-specific gamma imaging in invasive ductal breast cancer. Annals of nuclear medicine. 2017;31:19-28.
- Covington MF, Parent EE, Dibble EH, Rauch GM, Fowler AM. Advances and future directions in molecular breast imaging. Journal of Nuclear Medicine. 2022;63:17-21.
- 13. Lopez BP, Kappadath SC. Monte Carlo-derived 99mTc uptake quantification with commercial planar MBI: Tumor and breast activity concentrations. Medical physics. 2023;50:4388-98.
- Lopez BP, Kappadath SC. Monte Carlo-derived 99mTc uptake quantification with commercial planar MBI: Absolute tumor activity. Medical physics. 2023;50:2985-97.
- 15. GE Healthcare. NM Quantification Q.Metrix for SPECT/CT package (white paper). 2017.
- Collarino A, Pereira Arias-Bouda LM, Valdés Olmos RA, van der Tol P, Dibbets-Schneider P, de Geus-Oei LF, et al. Experimental validation of absolute SPECT/CT quantification for response monitoring in breast cancer. Med Phys. 2018;45:2143-53.

- Collarino A, Valdés Olmos RA, van Berkel LG, Neijenhuis PA, Wijers LM, Smit F, et al. The clinical impact of molecular breast imaging in women with proven invasive breast cancer scheduled for breast-conserving surgery. Breast cancer research and treatment. 2018;169:513-22.
- 18. Fathinul Fikri A, Chong E, Syafrina A. The utility of the standardized uptake value, metabolic tumor volume and total lesion glycolysis as predictive markers of recurrent breast cancer. Egyptian Journal of Radiology and Nuclear Medicine. 2021;52:1-12.
- Sciuto R, Pasqualoni R, Bergomi S, Petrilli G, Vici P, Belli F, et al. Prognostic value of 99mTcsestamibi washout in predicting response of locally advanced breast cancer to neoadjuvant chemotherapy. Journal of Nuclear Medicine. 2002;43:745-51.
- Dickson JC, Armstrong IS, Gabiña PM, Denis-Bacelar AM, Krizsan AK, Gear JM, et al. EANM practice guideline for quantitative SPECT-CT. European journal of nuclear medicine and molecular imaging. 2023;50:980-95.



CHAPTER 7

Summary, General Discussion and Future Perspectives

SUMMARY

Quantitative positron emission tomography (PET) and Single Photon Emission Computed Tomography (SPECT) have made significant advancements in recent decades and are now incorporated into several clinical guidelines. However, there is considerable potential for their broader application across other indications, indicating that current capabilities are underutilized. A key barrier is the lack of robust evidence, underscoring the need for further research to validate their expanded applications, which could enable personalized treatment plans and improve outcomes across a broader range of diseases.

The aim of this thesis was to deepen the understanding of quantitative PET and SPECT in clinical settings, explore their potential beyond current applications, and establish a foundation for their broader implementation in clinical practice.

Part 1: Novel clinical applications of quantitative PET/CT

Rubidium-82 PET/computed tomography ([82Rb]Cl PET/CT) is increasingly being used for cardiac perfusion imaging. The flow tracer 82Rb accumulates in the myocardial cells, has a short physical half-life (75 s) and a high first-pass extraction in the kidneys that also enables renal perfusion quantification, but is not yet used for this application in clinical practice. Chapter 2 investigated the application of a one-tissue compartment model for measuring renal hemodynamics using dynamic [82 Rb]Cl PET/CT imaging, and whether dynamic PET/CT is sensitive to detect differences in renal hemodynamics in stress compared to rest. Our study demonstrated that obtaining renal K, and renal blood flow (RBF) values using [82Rb]CI PET/CT was feasible using a one-tissue compartment model. Applying iso-contouring as the PET-based volumes of interest (VOI) of the kidney and using abdominal aorta (AA) as an image-derived input functions (IDIFs) is suggested for consideration in further studies. Dynamic [82Rb]CI PET/CT imaging showed significant differences in renal hemodynamics in rest compared to pharmacological stress using adenosine. This indicates that dynamic [82Rb]CI PET/CT has potential to detect differences in renal hemodynamics in stress conditions compared to the resting state, and might be useful as a novel diagnostic tool for assessing renal perfusion.

Since the end of 2019, the coronavirus disease 2019 (COVID-19) virus has infected millions of people, of whom a significant group suffers from sequelae from COVID-19, termed long COVID. As more and more patients emerge with long COVID who have symptoms of fatigue, myalgia and joint pain, we must examine potential biomarkers to find quantifiable parameters to define the underlying mechanisms and enable response monitoring. **Chapter 3** assessed the potential added value of non-metabolizable glucose analogue 2-[18F]fluoro-2-deoxy-D-glucose ([18F]FDG)-PET/CT for long COVID patients. Two analyses were performed: semi-

quantitative analysis using target-to-background ratios (TBRs) in 24 targets and total vascular score (TVS) assessed by two independent nuclear medicine physicians. The targets included nine research targets described in the European Association for Nuclear Medicine (EANM) recommendations for [18F]FDG-PET/CT imaging in large vessel vasculitis and polymyalgia rheumatica: the carotid, subclavia, axillary, vertebral, and pulmonary arteries, the ascending, descending, and abdominal aorta, and the aortic arch. Additional targets consisted of the parotid glands, external iliac arteries, femoral arteries, tibial arteries, the liver and the brachioradialis muscle. Thirteen patients were included in the long COVID group and 25 patients were included in the control group. No significant differences (P < 0.05) were found between the long COVID group and the control group in the TBR or TVS assessment. As we found no quantitative difference in the TBR or TVS between long COVID patients and controls, we are unable to prove that [18F]FDG is of added value for long COVID patients with symptoms of myalgia or joint pain. Given that a similar study showed contradicting results, this suggests that more research is needed to understand the underlying mechanisms of long COVID. Nevertheless, these studies, even with negative results, contribute to the growing knowledge of [18F]FDG-PET/CT's application in long COVID.

Chapter 4 assessed the lower [18F]FDG limit in administered activity and/or scan time reduction capabilities of a digital bismuth germanium oxide 32-cm axial field-of-view PET system while being compliant with current and updated EANM Research Ltd Fluorine-18 accreditation specifications (EARL, and EARL,, respectively). EARL, and EARL, compliance of the digital-BGO system (Omni Legend 32 cm) was tested for several reconstructions, including those that apply precision deep learning-based image enhancement (PDL) as postprocessing, using the calibration QC and National Electric Manufacturer's Association (NEMA) IEC phantom measurements. When we applied 1 min per bed position for PET acquisition, [18F]FDG administration can be reduced by a factor of ~4 for EARL,, by a factor of ~8 for EARL, (2 mm voxels) and by a factor of ~4 for EARL, (4 mm voxels) using both standard reconstructions and PDL post-processing compared to current EANM recommendations for [18F]FDG administration (7 MBg/min/bed-1.kg-1). With this study we provided an initial insight into the applicable lower limit in [18F]FDG administered activity and/or scan time reduction while being EARL, and EARL, Fluorine-18 compliant for the Omni Legend PET/CT system. This might allow for a higher patient throughput and/ or lower radiopharmaceutical activity, reducing costs and radiation exposure for both patients and staff, while potentially expanding the applications of (quantitative) PET.

Part 2: Novel clinical applications of quantitative SPECT/CT

Myocardial perfusion scintigraphy is based on visual interpretation of relative myocardial perfusion and might underestimate the severity of ischemia due to global hypoperfusion (triple vessel disease). Hence, quantitative SPECT may enable measurement of myocardial

uptake to improve evaluation of response to anti-ischemic therapies using myocardial perfusion scans, Chapter 5 investigated the quantitative accuracy and precision of a novel iterative reconstruction technique (Evolution; GE Healthcare) for the potential application of response monitoring using [99mTc]Tc-tetrofosmin SPECT/CT in patients with coronary artery disease (CAD). Our phantom study showed that seven iterations (10 subsets) and Butterworth post-filtering (cut off frequency 0.52in cycles/cm, order of 5) were considered optimal for reconstruction based on convergence and noise level. Applying these settings, the average repeatability deviation (or precision) of all acquisitions was 2.91%. Moreover, the accuracy of Evolution using larger defects resulted in higher recovery coefficients (ranging from 0.64 to 0.75) compared to smaller defects (recovery coefficients ranging from 0.52 to 0.74). To illustrate the feasibility of clinical application, ten patients, before and after intramyocardial injection of autologous bone marrow cells, were included retrospectively. Eight out of ten patients showed significant changes in uptake before and after treatment (p < 0.05). This was the first study to evaluate Evolution for cardiac applications demonstrating promising results for the application of quantitative SPECT in patients with CAD.

Molecular Breast Imaging (MBI) is a non-invasive technique for in vivo characterization of breast lesions. It uses the radiopharmaceutical [99mTc]Tc-sestamibi, a P-glycoprotein (Pgp) substrate, enabling potential prediction of chemoresistance based on uptake levels. Reduced uptake may indicate Pgp overexpression, aiding in prediction of response to neoadjuvant chemotherapy (NAC). Hence, quantification of [99mTc]Tc-sestamibi accumulation might help quiding treatment decisions. However, recent studies highlight limitations of planar MBI in accurately quantifying tumor uptake, suggesting that SPECT/ CT may help overcome these shortcomings. Moreover, prone hanging breast SPECT is a technique in which the patient is positioned face-down (prone) during image acquisition to reduce attenuation and motion artifacts. Chapter 6 evaluated the semiquantitative SPECT parameters of prone hanging breast SPECT using [99mTc]Tc-sestamibi and compared them with MBI-derived semi-quantitative parameters for the potential use of response prediction in women with locally advanced breast cancer (LABC). Eighteen patients with proven LABC with a tumor≥2 cm diameter on mammography and an indication for MBI using [99mTc]Tc-sestamibi were prospectively enrolled. Various semi-quantitative parameters were composed for early and delayed SPECT acquisitions (5 min p.i and 90 min p.i.) and MBI. No significant difference was observed between MBI and early SPECT semi-quantitative parameter functional tumor volume (FTV) (p = 0.46). $\mathsf{TBR}_{\mathsf{mean}}$ and $\mathsf{TBR}_{\mathsf{max}}$ were significantly higher for SPECT compared to MBI and showed greater variability between the measurements (p<0.05). Moreover, wash-out rates (WOR) showed a large interquartile range (IQR) (62.28), indicating that there is WOR variation among the LABC patients. Also, the FTV derived from early prone hanging breast SPECT/

И

CT is comparable with MBI-based FTV (p = 0.46). This was the first feasibility study evaluating the semi-quantitative parameters of prone hanging breast SPECT/CT using [99m Tc]Tc-sestamibi and comparing them with MBI-based semi-quantitative parameters in 18 patients with LABC. This study presented the first step towards a possible application of semi-quantitative parameters of prone hanging breast SPECT/CT in LABC patients for prediction of response to NAC.

In conclusion, while extensive technological capabilities for quantitative PET and SPECT exist, their broader clinical implementation is hindered by the slow accumulation of sufficient clinical evidence for new clinical applications. Although effective in established areas (e.g. quantification of myocardial perfusion, patient stratification (theranostics), therapy response prediction), further research is essential to validate their expanded clinical use. Closing the evidence gap will enable these technologies to guide more personalized treatments and improve clinical outcomes. This thesis contributes by exploring novel quantitative PET and SPECT applications in the fields of infectiology, nephrology, oncology and cardiology, but much work remains. Further research is required to optimize quantitative SPECT and PET, thereby enabling a broader patient population to benefit from their full clinical potential.

GENERAL DISCUSSION AND FUTURE PERSPECTIVES

The shift towards quantitative evaluation in nuclear medicine represents a significant advancement in diagnostic imaging, offering objective and reproducible data that enhance diagnostic accuracy and might improve patient management. Quantitative PET and SPECT imaging provide valuable insights into physiological and metabolic processes, including the monitoring of disease progression or the determination of therapeutic response. Rapid improvements in nuclear medicine innovations, as advancements in hardware and software, are paving the way for broader adoption of quantitative imaging in routine clinical practice. Moreover, improved temporal resolution in dynamic acquisition makes quantification possible and helps facilitate its adoption in clinical practice. The existing capabilities of quantitative PET and SPECT remain underutilized, as they have not been widely implemented beyond standard fields due to insufficient or inadequate evidence.

This thesis investigates the potential of quantitative PET and SPECT beyond their current applications, focusing on indications where they are not yet applied in clinical practice. This may serve as a foundation for broader integration of quantitative PET and SPECT into clinical practice and eventually contribute to improved patient outcomes through more objective, standardized and less observer dependent diagnostic and therapeutic strategies.

Quantitative dynamic PET for assessing renal perfusion

Chapter 2 applies kinetic modeling to explore the potential use of dynamic [82Rb]CI PET/CT for assessing renal perfusion. While these techniques are well-established for myocardial perfusion, their application to renal studies remains largely uninvestigated. Despite available software for cardiac imaging, adapting it for renal imaging requires special modifications related to anatomical and physiological differences that are specific for the kidney. In Chapter 2, we demonstrated the feasibility of using dynamic [82Rb]CI PET/CT for determining renal hemodynamics during different physiological conditions (e.g. rest and exposure to vasodilatation by adenosine). Future, larger studies are needed to refine renal dynamic PET protocols including acquisition and processing methods (e.g. VOI delineation), as well as to determine reference values and values in specific patient groups (e.g. high stage chronic kidney disease (CKD), renal artery stenosis). Despite their vital role in overall health, the kidneys are often overlooked in research. As a result, renal diseases are frequently diagnosed at a relatively late stage, contributing to significant morbidity, mortality, and substantial healthcare and societal costs. This underscores the urgent need for greater awareness and further development of diagnostic imaging tools, such as quantitative dynamic PET/CT, that can support earlier detection and intervention in renal disease.

Dynamic PET quantifies renal perfusion by tracking radiotracer distribution over time, enabling the assessment of tracer kinetics in different renal compartments. Among available PET tracers, [¹⁵O]H₂O, [¹³N]ammonia and [¹8F]Flurpiridaz enable measurement of tissue perfusion due to their high extraction fractions and favorable kinetics. However, [¹⁵O]H₂O and [¹³N]ammonia require an on-site cyclotron for production and their use remains largely preclinical with limited clinical validation to date [1, 2]. [¹8F]Flurpiridaz is a novel [¹8F]-labeled PET tracer for myocardial perfusion imaging (MPI), recently approved by the FDA for clinical use. Its relatively long half-life allows production as a unit dose at a regional cyclotron. To the best of our knowledge, no studies have reported its use in renal perfusion imaging [3, 4]. The generator-produced tracer [8²Rb]Cl offers greater accessibility and logistical advantages, making it a practical option for renal perfusion imaging, although its lower extraction and short half-life may limit quantitative accuracy.

Other imaging modalities have notable limitations. Ultrasound Doppler provides only qualitative or semi-quantitative flow data, while contrast-enhanced CT and Magnetic Resonance Imaging (MRI) may be limited by nephrotoxicity or low temporal resolution. In contrast, dynamic PET yields absolute perfusion values in milliliters per minute per gram of tissue. This might be advantageous in complex clinical areas such as high stage CKD, renovascular stenosis and monitoring transplant viability. Nonetheless, its ability to provide reproducible quantification across renal compartments positions dynamic PET as a promising tool, potentially bridging the gap between functional imaging and personalized nephrological care.

(Semi)quantitative PET in long COVID

The emergence of new diseases like COVID in 2019 highlights the need for (imaging) biomarkers to identify quantifiable parameters that define underlying mechanisms, assess disease activity, and monitor treatment response. We were unable to demonstrate that [18F]FDG offers added value for long COVID patients with symptoms of myalgia or joint pain (**Chapter 3**). However, no guidelines for interpretation, acquisition and processing exist for [18F]FDG-PET/CT in long COVID patients, aside from the recommendations that come closest to addressing this issue, as outlined in **Chapter 3**.

Long COVID is a complex post-viral condition involving persistent symptoms, inflammation, and immune dysregulation. [18F]FDG-PET/CT offers significant value in early detection of infection and inflammation by identifying subtle metabolic abnormalities, with superior sensitivity to anatomical imaging techniques like chest X-ray, CT, and MRI. Furthermore, [18F]FDG-PET/CT allows semi-quantitative assessment of inflammation and recovery, using standardized uptake values [5]. In long COVID, quantitative PET holds significant potential to substantially improve patient stratification, reveal key pathophysiological mechanisms,

such as neuroinflammation or pulmonary inflammation, and enable effective monitoring of treatment [5, 6]. However, several challenges remain, including the lack of validated disease-specific thresholds and the considerable clinical and biological heterogeneity of long COVID. Patients show a wide spectrum of symptoms affecting multiple organ systems, with underlying mechanisms varying from persistent inflammation and immune dysregulation to microvascular injury and autonomic dysfunction. This variability complicates the interpretation of medical imaging (also PET) findings and underscores the need for tailored (quantitative) imaging protocols to accurately capture the pathological variations within the long COVID population.

Moreover, emerging evidence suggests that brain [¹⁸F]FDG-PET provides valuable insights into the neurological effects of long COVID, since it has revealed a characteristic hypometabolic pattern in the brain in a substantial proportion of individuals with long COVID, suggesting the involvement of specific neural networks. As such, it may serve to objectively confirm brain involvement and support differential diagnosis against neurodegenerative, inflammatory, or psychiatric conditions [6]. (Semi)quantitative analysis enhances visual assessment, especially for less experienced readers, by utilizing an age-matched control database and a PET system with comparable (i.e. harmonized) performance characteristics, thus providing more reliable and objective results [7].

Further research and standardization are needed before PET/CT becomes part of routine clinical use in long COVID patients. Furthermore, the standardization of (semi)quantitative analysis and the application of VOI delineation methods (e.g. semi-automatic, manual, or CT-based) are essential. To ensure the successful implementation of quantitative nuclear imaging in new applications and indications, it is essential for researchers and clinicians to collaborate multidisciplinary in identifying appropriate methodologies. Establishing and sharing standardized approaches through publications and guidelines will be crucial in advancing the field and improving the comparability and reliability of future studies.

Other clinical quantitative PET applications

In PET imaging, quantification methods can be broadly categorized into semi-quantitative and absolute quantification. Semi-quantitative analysis involves comparing relative metabolic activity between regions of interest, often using SUVs, whereas absolute quantification measures the exact concentration of a radiotracer in a specific tissue. A commonly used example of semi-quantitative analysis in clinical practice is the Deauville scoring system for assessing treatment response in Hodgkin lymphoma and certain types of non-Hodgkin lymphoma [6]. This method involves visually comparing the [18F]FDG uptake in residual tumor lesions to that in reference regions such as the mediastinum and liver on PET scans. The score is based on relative uptake rather than absolute quantitative values like the SUV, making it a practical and reproducible tool for clinicians to monitor treatment response.

In addition to the chapters in this thesis addressing two novel applications of (semi) quantitative PET, various other directions are currently discussed in the literature, holding significant potential for further exploration. For instance, (semi)quantitative evaluation may aid in differentiating between physiological and pathological uptake [8-12], distinguishing benign from malignant diseases [12-15], enhancing therapy response monitoring in oncology [16-20], and sarcoidosis [21, 22], and improving radiotherapy planning by refining target delineation [23]. Its utility extends beyond the current scope of this thesis, offering opportunities in diagnostics and treatment across various medical disciplines.

Reduction tracer administration in PET

Recent advancements in nuclear medicine, particularly in hardware (e.g. digital detectors), and software (post-processing and reconstruction algorithms, e.g. including those that use artificial intelligence (AI)), have created opportunities for optimizing tracer administration in clinical PET/CT imaging. These innovations ensure the necessity of finding a balance between high-quality imaging and minimizing radiation exposure. However, literature on tracer reduction strategies for new scanners is limited, necessitating further evaluation by each institution to identify and validate the options available for their specific scanners. **Chapter 4** describes the possibilities in tracer administration reduction per bed position at our institution, allowing for the selection of the protocol/dosing schedule to be adopted in clinical practice.

Frequent scanning may be necessary for recurrence detection and therapy response monitoring. In these situations, it is essential to minimize the radiation dose as much as possible. Furthermore, reducing tracer administration and/or scan time could enable new applications for (quantitative) PET. This includes achieving a low enough dose to facilitate imaging in pregnant women [24, 25], and in the pediatric population [26], as well as enabling faster imaging for intensive care patients [27]. In addition to the potential indications, [18F]FDG-PET is used to non-invasively assess the metabolic activity of brown adipose tissue [28, 29], providing insight into its role in thermogenesis and energy expenditure, relevant for metabolic disorders like obesity and diabetes. This is typically done in healthy volunteers, where the level of radiation exposure deemed acceptable by a Medical Ethics Review Committee is limited, which makes the use of a lower administered activity particularly advantageous.

Efforts in recent years have focused on optimizing attenuation correction (AC) in nuclear medicine to reduce radiation exposure. All reconstruction can be applied to convert a low-dose CT scan into improved image quality or by using ultra-low-dose CT with tin filters for AC [30]. Additionally, innovations that eliminate the need for CT, such as utilizing the low-level inherent radiation from PET crystals [31, 32], employing synthetic CT data [33], and

reconstructing AC images from the PET emission data using Maximum Likelihood Attenuation and Activity [34], are currently being investigated. These AC innovations, combined with the high sensitivity of modern scanners, allow for rapid imaging at doses low enough to support PET screening in high-risk populations (e.g. cancer, Alzheimer's disease) [35].

Clinical applications for quantitative SPECT

Quantitative SPECT is an emerging imaging technology, however, as with any new technology, its success depends on whether routine clinical applications can be identified. Key opportunities include the potential use of quantitative SPECT for response prediction in oncology (e.g. breast cancer, **chapter 6**), pre- and post-treatment dosimetry [36-38], improving personalized radiopharmaceutical therapy. Furthermore, in cardiac imaging, quantitative SPECT holds potential for perfusion analysis (**chapter 5**) and amyloidosis [39]. While there is a growing trend towards using PET over SPECT for MPI, SPECT remains a cost-effective and widely accessible option, as most healthcare facilities are equipped with SPECT rather than PET. This widespread availability, coupled with lower operational costs, makes SPECT a practical choice in many clinical settings, particularly in resource-limited environments.

As highlighted in the literature, quantitative SPECT is expected to play a significant role in several routine clinical applications, such as assessing liver remnant function [40-42] and diagnosing neurodegenerative disorders [43, 44]. It also enhances lesion assessment for osteoarthritis and arthroplasty using bone-seeking tracers [45, 46]. Moreover, (quantitative) SPECT can use dual-isotope imaging where two tracers are injected at the same time and acquired simultaneously by the SPECT system. This allows clinicians to assess multiple physiological processes, such as myocardial perfusion and imaging of cardiac sympathetic innervation, in a single scan, rather than requiring separate imaging sessions. This consolidation into one hospital visit minimizes patient discomfort and accelerates clinical decision-making, ultimately leading to faster initiation of appropriate treatment strategies [47].

Recent advancements, including the development of digital multi-detector cadmium-zinc-telluride (CZT) ring-shaped SPECT/CT systems, have eliminated the need for camera rotation, thereby improving both imaging speed and resolution. These innovations enable dynamic three-dimensional (3D) assessments, the generation of time-activity curves, and the quantification of coronary flows, similar to the capabilities traditionally associated with cardiac PET [48]. Moreover, the extraction of quantitative parameters in additional applications, such as dynamic 3D renography [49], has also become feasible. These advancements hold the potential to provide comprehensive quantitative SPECT imaging in settings where PET technology and the necessary infrastructure are not available.

FUTURE PERSPECTIVES

Standardization of quantitative PET and SPECT

There is substantial diversity in scanners and regional preferences globally, which complicates direct comparisons between studies. As a result, data often differ across institutions, making validation and implementation more challenging. Standardization and harmonization of quantification protocols are critical to ensure consistent and reproducible results across different institutions.

Quantitative parameters in PET and SPECT are significantly influenced by various technical factors, such as differences in equipment, acquisition protocols, reconstruction settings, and processing software. These variations make it challenging to establish standardized threshold values for discriminating between true and false positives or distinguishing between healthy and diseased states. In response to this challenge, the European Association of Nuclear Medicine (EANM) launched the EANM Research Ltd. (EARL) initiative (also used in **chapter 4**), aiming to harmonize quantification in nuclear medicine imaging. Currently, EARL primarily focuses on oncology PET studies. To support the standardization of both PET and SPECT, EARL has already published guidelines for acquisition protocols, interpretation, and reporting of quantitative imaging. Future accreditation programs, such as those offered by EARL, may play a crucial role in further standardizing quantitative PET and SPECT across different medical centers, thereby enhancing the reliability of future research and facilitating multicenter studies.

Long-axis field-of-view PET: Advancements in Imaging Technology

Long-axis field-of-view (LAFOV) PET scanners allow whole-body imaging with high sensitivity, providing high resolution temporal and spatial information across multiple organ systems simultaneously. The LAFOV PET provides advantages such as reduced radiation exposure, enhanced image quality, shorter acquisition times, and the ability to effectively image tracers with low radioactivity.

Earlier in this chapter, the possibilities for reducing tracer administration in PET with standard oncology tracers, such as [18F]FDG, for sensitive scanners were discussed, and this also applies to the "ultra-sensitive" LAFOV PET/CT. However, for tracers like [89Zr]-labelled monoclonal antibodies used in immunoPET, short-axis FOV (SAFOV) systems face challenges due to the long half-life (78.4 h) and non-usable emissions, limiting injected activity for radiation dosimetry. LAFOV systems overcome these limitations with higher sensitivity, enabling faster acquisitions, reducing motion risks, and enhancing tumor-to-background contrast [50]. This is particularly beneficial for [89Zr]-labelled tracers targeting immune-related biomarkers (e.g. VEGF, PD-L1, HER2, or CD8 expression), as it aids in predicting responses to immunomodulatory treatments.

As described in **chapter 2**, imaging with [82Rb]Cl, which has a short half-life of 75 s, is suitable for clinical cardiac perfusion imaging. However, acquiring late-phase images of the Na+/K+ ATPase function using [82Rb]Cl, suggested as a potential biomarker for prostate and breast cancer, is challenging with SAFOV scanners [50]. The high sensitivity and timing resolution of LAFOV PET systems are expected to tackle this issue and enhance imaging of short half-life tracers as [82Rb]Cl. This advancement may broaden its clinical indications, including potential use in renal perfusion imaging.

Conventional PET offers dynamic imaging over a limited FOV, while LAFOV PET enables dynamic assessment across larger areas. A key benefit is the ability to perform dynamic scanning of individual body regions, including visualization of the major vessels, which enables consistent extraction of an IDIF, thereby eliminating the need for arterial blood sampling. Nevertheless, venous sampling remains necessary for metabolite analysis. For drug development, the use of such a LAFOV scanner is particularly advantageous.

The high sensitivity and timing resolution of LAFOV scanners enable the acquisition of dynamic data, allowing for the extraction of high-quality lesion and arterial blood time-activity curves [51, 52]. These curves can be used to calculate parameters with potentially greater biological significance and specificity than commonly used static measures like the SUV [53]. This capability could significantly enhance the clinical evaluation of systemic diseases. However, challenges remain including the high costs and resource demands due to long scan times and substantial computational power required to process large datasets. Expanding dynamic PET datasets and multicenter studies are crucial for advancing quantitative imaging, for example in developing prediction tools that support clinical decision-making.

Respiratory motion significantly hinders the PET evaluation of lesions in the lower thorax. The high sensitivity of the LAFOV PET scanners, however, facilitates the application of breath-holding during shorter acquisition periods. Cui et al. (2024) showed that a 30-second acquisition and breath-hold make PET/CT both clinically feasible and more accurate [54]. This methodology effectively reduces background lung uptake and significantly improves both lesion registration and quantification, particularly in the lower thoracic region. Such advancements highlight the potential of this approach in overcoming challenges associated with respiratory motion during PET imaging.

Conclusion

Technologically, extensive capabilities are already in place, yet the broader clinical implementation of quantitative PET and SPECT is limited by the slow process of gathering sufficient evidence to support their use in new clinical applications. This slow accumulation of robust clinical data hinders the widespread adoption of quantitative PET and SPECT, limiting the number of patients who can benefit from their potential advantages.

While quantitative PET and SPECT have proven effective in established areas, future research is critical to validate their expanded applications. Overcoming the evidence gap will enable these technologies to guide more tailored treatment strategies and improve clinical outcomes for a broader range of diseases. This thesis makes a modest contribution by exploring several novel applications of quantitative PET and SPECT, highlighting their potential for broader implementation, but there is still a long way to go. By continuing to advance research in this field, these powerful diagnostic tools can be further optimized, ensuring that more patients benefit from their capabilities.

REFERENCES

- Alpert NM, Rabito CA, Correia DJA, Babich JW, Littman BH, Tompkins RG, et al. Mapping of local renal blood flow with PET and H215O. Journal of Nuclear Medicine. 2002:43:470-5.
- Werner RA, Pomper MG, Buck AK, Rowe SP, Higuchi T. SPECT and PET radiotracers in renal imaging. Seminars in Nuclear Medicine: Elsevier; 2022. p. 406-18.
- Packard RRS, deKemp RA, Knuuti J, Moody JB, Renaud JM, Saraste A, et al. Quantitative approaches to 18F-flurpiridaz positron emission tomography image analysis. Journal of Nuclear Cardiology. 2025;45.
- Maddahi J. 18F flurpiridaz PET MPI: Imaging characteristics and clinical trials. Journal of Nuclear Cardiology. 2025;45.
- Eibschutz LS, Rabiee B, Asadollahi S, Gupta A, Assadi M, Alavi A, et al. FDG-PET/CT of COVID-19 and other lung infections. Seminars in nuclear medicine: Elsevier; 2022. p. 61-70.
- Verger A, Barthel H, Tolboom N, Fraioli F, Cecchin D, Albert NL, et al. 2-[18F]-FDG PET for imaging brain involvement in patients with long COVID: perspective of the EANM Neuroimaging Committee. European Journal of Nuclear Medicine and Molecular Imaging. 2022;49:3599-606.
- Mairal E, Doyen M, Rivasseau-Jonveaux T, Malaplate C, Guedj E, Verger A. Clinical impact of digital and conventional PET control databases for semi-quantitative analysis of brain 18 F-FDG digital PET scans. EJNMMI research. 2020;10:1-10.
- 8. Cho YS, Moon SH, Choi JY, Choe YS, Kim B-T, Lee K-H. Clinical significance of incidental 18F-FDG uptake in the pyriform sinus detected by PET/CT. Clinical nuclear medicine. 2016;41:e82-e6.
- Hyun SH, Choi JY, Lee K-H, Choe YS, Kim B-T. Incidental focal 18F-FDG uptake in the pituitary gland: clinical significance and differential diagnostic criteria. Journal of Nuclear Medicine. 2011:52:547-50.
- Davison JM, Ozonoff A, Imsande HM, Grillone GA, Subramaniam RM. Squamous cell carcinoma of the palatine tonsils: FDG standardized uptake value ratio as a biomarker to differentiate tonsillar carcinoma from physiologic uptake. Radiology. 2010;255:578-85.
- Ju H, Zhou J, Pan Y, Lv J, Zhang Y. Evaluation of pituitary uptake incidentally identified on 18F-FDG PET/CT scan. Oncotarget. 2017;8:55544.
- 12. Pencharz D, Nathan M, Wagner TL. Evidence-based management of incidental focal uptake of fluorodeoxyglucose on PET-CT. The British journal of radiology. 2018;91:20170774.
- Tessonnier L, Sebag F, Palazzo F, Colavolpe C, De Micco C, Mancini J, et al. Does 18 F-FDG PET/ CT add diagnostic accuracy in incidentally identified non-secreting adrenal tumours? European journal of nuclear medicine and molecular imaging. 2008;35:2018-25.
- Treglia G, Taralli S, Salsano M, Muoio B, Sadeghi R, Giovanella L. Prevalence and malignancy risk of focal colorectal incidental uptake detected by 18F-FDG-PET or PET/CT: a meta-analysis. Radiology and oncology. 2014;48:99.
- 15. Van Hoeij F, Keijsers R, Loffeld B, Dun G, Stadhouders P, Weusten B. Incidental colonic focal FDG uptake on PET/CT: can the maximum standardized uptake value (SUV max) guide us in the timing of colonoscopy? European journal of nuclear medicine and molecular imaging. 2015;42:66-71.
- Young H, Baum R, Cremerius U, Herholz K, Hoekstra O, Lammertsma A, et al. Measurement of clinical and subclinical tumour response using [18F]-fluorodeoxyglucose and positron emission tomography: review and 1999 EORTC recommendations. European journal of cancer. 1999;35:1773-82.

- Wahl RL, Jacene H, Kasamon Y, Lodge MA. From RECIST to PERCIST: evolving considerations for PET response criteria in solid tumors. Journal of nuclear medicine. 2009;50:122S-50S.
- Lopci E, Hicks RJ, Dimitrakopoulou-Strauss A, Dercle L, Iravani A, Seban RD, et al. Joint EANM/ SNMMI/ANZSNM practice guidelines/procedure standards on recommended use of [18F] FDG PET/CT imaging during immunomodulatory treatments in patients with solid tumors version 1.0. European journal of nuclear medicine and molecular imaging. 2022;49:2323-41.
- 19. Fanti S, Goffin K, Hadaschik BA, Herrmann K, Maurer T, MacLennan S, et al. Consensus statements on PSMA PET/CT response assessment criteria in prostate cancer. European journal of nuclear medicine and molecular imaging. 2021;48:469-76.
- Riedl CC, Pinker K, Ulaner GA, Ong LT, Baltzer P, Jochelson MS, et al. Comparison of FDG-PET/ CT and contrast-enhanced CT for monitoring therapy response in patients with metastatic breast cancer. European journal of nuclear medicine and molecular imaging. 2017;44:1428-37.
- 21. Vender RJ, Aldahham H, Gupta R. The role of PET in the management of sarcoidosis. Current Opinion in Pulmonary Medicine. 2022;28:485-91.
- 22. Agrawal T, Saleh Y, Sukkari MH, Alnabelsi TS, Khan M, Kassi M, et al. Diagnosis of cardiac sarcoidosis: a primer for non-imagers. Heart failure reviews. 2022;27:1223-33.
- Kong F-M, Ten Haken RK, Schipper M, Frey KA, Hayman J, Gross M, et al. Effect of midtreatment PET/CT-adapted radiation therapy with concurrent chemotherapy in patients with locally advanced non–small-cell lung cancer: A phase 2 clinical trial. JAMA oncology. 2017;3:1358-65.
- Korsholm K, Aleksyniene R, Albrecht-Beste E, Vadstrup ES, Andersen FL, Fischer BM. Staging of breast cancer in pregnancy with ultralow dose [18F]-FDG-PET/CT. European Journal of Nuclear Medicine and Molecular Imaging. 2023;50:1534-5.
- Smith CL, Yaqub M, Wellenberg RH, Knip JJ, Boellaard R, Zwezerijnen GJ. Ultra-low foetal radiation exposure in 18F-FDG PET/CT imaging with a long axial field-of-view PET/CT system. EJNMMI Phys. 2024;11:45.
- Mingels C, Spencer BA, Nalbant H, Omidvari N, Rokni M, Rominger A, et al. Dose Reduction in Pediatric Oncology Patients with Delayed Total-Body [18F] FDG PET/CT. Journal of Nuclear Medicine. 2024.
- Abikhzer G, Treglia G, Pelletier-Galarneau M, Buscombe J, Chiti A, Dibble EH, et al. EANM/SNMMI guideline/procedure standard for [18F] FDG hybrid PET use in infection and inflammation in adults v2. 0. European journal of nuclear medicine and molecular imaging. 2024:1-29.
- 28. Ter Voert EE, Svirydenka H, Müller J, Becker AS, Balaz M, Efthymiou V, et al. Low-dose 18 F-FDG TOF-PET/MR for accurate quantification of brown adipose tissue in healthy volunteers. EJNMMI research. 2020;10:1-10.
- Chen KY, Cypess AM, Laughlin MR, Haft CR, Hu HH, Bredella MA, et al. Brown Adipose Reporting Criteria in Imaging STudies (BARCIST 1.0): recommendations for standardized FDG-PET/CT experiments in humans. Cell metabolism. 2016;24:210-22.
- Mostafapour S, Greuter M, van Snick JH, Brouwers AH, Dierckx RA, van Sluis J, et al. Ultra-low dose CT scanning for PET/CT. Medical physics. 2024;51:139-55.
- Teimoorisichani M, Panin V, Rothfuss H, Sari H, Rominger A, Conti M. A CT-less approach to quantitative PET imaging using the LSO intrinsic radiation for long-axial FOV PET scanners. Medical physics. 2022;49:309-23.
- Sari H, Teimoorisichani M, Mingels C, Alberts I, Panin V, Bharkhada D, et al. Quantitative evaluation of a deep learning-based framework to generate whole-body attenuation maps using LSO background radiation in long axial FOV PET scanners. European journal of nuclear medicine and molecular imaging. 2022;49:4490-502.

- Montgomery ME, Andersen FL, d'Este SH, Overbeck N, Cramon PK, Law I, et al. Attenuation correction of long axial field-of-view positron emission tomography using synthetic computed tomography derived from the emission data: application to low-count studies and multiple tracers. Diagnostics. 2023;13:3661.
- Boellaard R, Hofman M, Hoekstra O, Lammertsma A. Accurate PET/MR quantification using time of flight MLAA image reconstruction. Molecular imaging and biology. 2014;16:469-77.
- 35. Slart RH, Tsoumpas C, Glaudemans AW, Noordzij W, Willemsen AT, Borra RJ, et al. Long axial field of view PET scanners: a road map to implementation and new possibilities. European journal of nuclear medicine and molecular imaging. 2021;48:4236-45.
- 36. Garin E, Tselikas L, Guiu B, Chalaye J, Edeline J, de Baere T, et al. Personalised versus standard dosimetry approach of selective internal radiation therapy in patients with locally advanced hepatocellular carcinoma (DOSISPHERE-01): a randomised, multicentre, open-label phase 2 trial. The lancet Gastroenterology & hepatology. 2021;6:17-29.
- Brosch-Lenz J, Delker A, Völter F, Unterrainer LM, Kaiser L, Bartenstein P, et al. Toward singletime-point image-based dosimetry of 177Lu-PSMA-617 therapy. Journal of Nuclear Medicine. 2023;64:767-74.
- Rosar F, Wenner F, Khreish F, Dewes S, Wagenpfeil G, Hoffmann MA, et al. Early molecular imaging response assessment based on determination of total viable tumor burden in [68 Ga] Ga-PSMA-11 PET/CT independently predicts overall survival in [177 Lu] Lu-PSMA-617 radioligand therapy. European Journal of Nuclear Medicine and Molecular Imaging. 2022:1-11.
- 39. Scully PR, Morris E, Patel KP, Treibel TA, Burniston M, Klotz E, et al. DPD quantification in cardiac amyloidosis: a novel imaging biomarker. Cardiovascular Imaging. 2020;13:1353-63.
- 40. Arntz PJ, Deroose CM, Marcus C, Sturesson C, Panaro F, Erdmann J, et al. Joint EANM/SNMMI/ IHPBA procedure guideline for [99mTc] Tc-mebrofenin hepatobiliary scintigraphy SPECT/CT in the quantitative assessment of the future liver remnant function. Hpb. 2023;25:1131-44.
- 41. Van Der Velden S, Braat MN, Labeur TA, Scholten MV, Van Delden OM, Bennink RJ, et al. A pilot study on hepatobiliary scintigraphy to monitor regional liver function in 90Y radioembolization. Journal of Nuclear Medicine. 2019;60:1430-6.
- 42. Olthof PB, Coelen RJ, Bennink RJ, Heger M, Lam MF, Besselink MG, et al. 99mTc-mebrofenin hepatobiliary scintigraphy predicts liver failure following major liver resection for perihilar cholangiocarcinoma. HPB. 2017;19:850-8.
- 43. Albert NL, Unterrainer M, Diemling M, Xiong G, Bartenstein P, Koch W, et al. Implementation of the European multicentre database of healthy controls for [123 I] FP-CIT SPECT increases diagnostic accuracy in patients with clinically uncertain parkinsonian syndromes. European journal of nuclear medicine and molecular imaging. 2016;43:1315-22.
- 44. Toriihara A, Daisaki H, Yamaguchi A, Kobayashi M, Furukawa S, Yoshida K, et al. Semiquantitative analysis using standardized uptake value in 123I-FP-CIT SPECT/CT. Clinical Imaging. 2018;52:57-61.
- 45. Kim J, Lee H-H, Kang Y, Kim T, Lee S, So Y, et al. Maximum standardised uptake value of quantitative bone SPECT/CT in patients with medial compartment osteoarthritis of the knee. Clinical radiology. 2017;72:580-9.
- Dickson JC, Armstrong IS, Gabiña PM, Denis-Bacelar AM, Krizsan AK, Gear JM, et al. EANM practice guideline for quantitative SPECT-CT. European journal of nuclear medicine and molecular imaging. 2023;50:980-95.
- 47. Blaire T, Bailliez A, Ben Bouallegue F, Bellevre D, Agostini D, Manrique A. First assessment of simultaneous dual isotope (123 I/99m Tc) cardiac SPECT on two different CZT cameras: A phantom study. Journal of Nuclear Cardiology. 2018;25:1692-704.

- 48. Gelbart E, Krakovich A, Sherm Y, Rabin G, Ratner H, Scheinowitz M, et al. Validation of advanced hybrid SPECT/CT system using dynamic anthropomorphic cardiac phantom. Annals of Nuclear Medicine. 2024;38:919-26.
- Hesse M, Dupont F, Mourad N, Babczenko P, Beaurin G, Xhema D, et al. Kidney dynamic SPECT acquisition on a CZT swiveling-detector ring camera: an in vivo pilot study. BMC medical imaging. 2024;24:94.
- 50. Cook GJ, Alberts IL, Wagner T, Fischer BM, Nazir MS, Lilburn D. The impact of long axial field of view (LAFOV) PET on oncologic imaging. European Journal of Radiology. 2024:111873.
- 51. Pan B, Marsden PK, Reader AJ. Kinetic model-informed deep learning for multiplexed PET image separation. EJNMMI Phys. 2024;11:56.
- 52. Rahmim A, Lodge MA, Karakatsanis NA, Panin VY, Zhou Y, McMillan A, et al. Dynamic whole-body PET imaging: principles, potentials and applications. European journal of nuclear medicine and molecular imaging. 2019;46:501-18.
- Gu F, Wu Q. Quantitation of dynamic total-body PET imaging: recent developments and future perspectives. European Journal of Nuclear Medicine and Molecular Imaging. 2023;50:3538-57.
- 54. Cui Y, Jia J, Yan Q, He X, Yuan K, Li Z, et al. The impact of deep-inspiration breath-hold total-body PET/CT imaging on thoracic 18F-FDG avid lesions compared with free-breathing. European Journal of Radiology. 2024:111549.



CHAPTER 8

Nederlandse Samenvatting (Dutch Summary)

Kwantitatieve positronemissietomografie (PET) en enkelvoudige fotonemissietomografie (SPECT) hebben de afgelopen decennia aanzienlijke vooruitgang geboekt en zijn inmiddels opgenomen in diverse klinische richtlijnen. Momenteel wordt kwantitatieve SPECT en PET voor een beperkt aantal ziektebeelden gebruikt terwijl het breder in de klinische praktijk toegepast zou kunnen worden. Dit wijst erop dat de huidige mogelijkheden nog niet volledig worden benut. Een belangrijke belemmering is het gebrek aan robuust bewijs, wat de noodzaak benadrukt voor verder onderzoek om de bredere klinische toepassing te valideren. Dit kan gepersonaliseerde behandelplannen mogelijk maken en de uitkomsten verbeteren bij een grotere verscheidenheid aan ziekten.

Het doel van dit proefschrift was om meer inzicht te krijgen in kwantitatieve PET en SPECT in klinische contexten, het potentieel ervan buiten de huidige toepassingen te verkennen en een basis te leggen voor bredere implementatie in de klinische praktijk.

Deel 1: Nieuwe klinische toepassingen van kwantitatieve PET/CT

Rubidium-82 PET/computertomografie ([82Rb]CI PET/CT) wordt steeds vaker gebruikt voor de beeldvorming van cardiale perfusie. De flow-tracer 82Rb hoopt zich op in de myocardcellen, heeft een korte fysieke halfwaardetijd (75 s) en een hoge extractie tijdens de eerste doorgang door de nieren, wat renale perfusie kwantificatie mogelijk maakt. Deze toepassing wordt echter nog niet klinisch benut. Hoofdstuk 2 onderzocht het gebruik van een één-compartimentenmodel voor het meten van renale hemodynamiek met behulp van dynamische [82Rb]Cl PET/CT en of dynamische PET/CT gevoelig is voor het detecteren van verschillen in renale hemodynamiek tussen rust en stress. Onze studie toonde aan dat het verkrijgen van renale K,- en renale bloedstroomwaarden (RBF) met [82Rb]CI PET/CT haalbaar was met een één-compartimentenmodel. Het gebruik van iso-contouring voor PET-gebaseerde intekeningen (VOI) van de nieren en de abdominale aorta (AA) als beeldafgeleide inputfunctie (IDIF) wordt aanbevolen voor vervolgstudies. Dynamische [82Rb]CI PET/CT liet significante verschillen zien in renale hemodynamiek tussen rust en farmacologische stress met adenosine. Dit suggereert dat deze methode potentie heeft als een nieuw diagnostisch instrument voor het evalueren van de nierperfusie.

Sinds eind 2019 heeft het virus dat de ziekte COVID-19 veroorzaakt miljoenen mensen besmet, van wie een aanzienlijke groep kampt met restklachten als gevolg van COVID-19, ook wel long COVID genoemd. Steeds meer patiënten presenteren zich met langdurige COVID en symptomen zoals vermoeidheid, spierpijn en gewrichtspijn. Daarom is het belangrijk om mogelijke biomarkers te onderzoeken, zodat we kwantificeerbare parameters kunnen vinden om de onderliggende mechanismen te definiëren en de respons te kunnen monitoren. **Hoofdstuk 3** evalueerde de mogelijke meerwaarde

van 2-[18F]fluoro-2-deoxy-D-glucose ([18F]FDG)-PET/CT, een glucose-analoog dat niet metaboliseert, bij patiënten met long COVID. Twee analyses werden uitgevoerd: semi-kwantitatieve analyse via doel-tot-achtergrond ratio's (TBRs) in 24 doelgebieden en de totale vasculaire score (TVS), beoordeeld door twee onafhankelijke nucleair geneeskundigen. De doelgebieden omvatten negen structuren zoals aanbevolen door de Europese Vereniging voor Nucleaire Geneeskunde (EANM) voor [18F]FDG-PET/CT bij grote vaten vasculitis en polymyalgia rheumatica zoals: de arteria carotis, arteria subclavia, arteria axillaris, arteria vertebralis en arteria pulmonalis, de aorta ascendens en aorta descendens, en de aortaboog. Aanvullende doelgebieden bestonden uit de glandula parotis, arteria iliaca externa, arteria femorales, arteria tibiales, de lever en de musculus brachioradialis. In onze studie werden dertien patiënten met long COVID en 25 controlepatiënten geïncludeerd. Er werden geen significante verschillen (P < 0,05) gevonden tussen de groepen wat betreft TBR of TVS. Aangezien er geen kwantitatieve verschillen werden gevonden, kunnen we op basis van onze resultaten niet aantonen dat [18F]FDG toegevoegde waarde heeft bij long COVID-patiënten met spier- of gewrichtspijn. De bevindingen uit eerdere studies, die niet altiid eenduidig zijn, benadrukken de waarde van aanvullend onderzoek. Gezien de beperkte beschikbare kennis over deze relatief nieuwe aandoening, dragen onze bevindingen, zelfs met negatieve resultaten, bij aan de groeiende kennis over de toepassing van [18F]FDG-PET/CT bij long COVID.

Hoofdstuk 4 evalueerde de minimale toegediende [18F]FDG-activiteit en/ of de mogelijkheden tot verkorting van de scantijd bij gebruik van een digitaal bismutgermaniumoxide (BGO) PET-systeem met een axiaal gezichtsveld van 32 cm. Daarnaast moest voldaan worden aan de huidige en vernieuwde accreditatiespecificaties van de EANM Research Ltd voor Fluor-18 (respectievelijk EARL, en EARL₂). EARL is een dochterorganisatie van de EANM die zich richt op het bevorderen van standaardisatie en kwaliteitsborging in de nucleaire geneeskunde. De EARL,- en EARL,-conformiteit van het digitale BGO-systeem (Omni Legend 32 cm) werd getest voor meerdere reconstructiemethoden, waaronder ook die met deep learning-gebaseerde beeldverbetering (zgn. PDL) als nabewerking, op basis van kalibratiekwaliteitscontroles (QC) en metingen met het National Electric Manufacturer's Association (NEMA) IEC fantoom. Bij toepassing van een acquisitietijd van 1 minuut per bedpositie kon de [18F] FDG-toediening met een factor van ongeveer 4 worden gereduceerd voor EARL, met een factor van ongeveer 8 voor EARL, (met 2 mm voxels), en met een factor van ongeveer 4 voor EARL, (met 4 mm voxels), zowel bij standaardreconstructies als bij PDL-nabewerking, vergeleken met de huidige aanbevelingen van de EANM voor [18F]FDG-toediening (7 MBq·min·bed⁻¹·kg⁻¹). Met deze studie werd een eerste inzicht verkregen in de toepasbare ondergrens voor de [18F]FDG-activiteit en/of verkorte scantijd, met behoud van EARL,- en EARL₂-conformiteit voor het Omni Legend PET/CT-systeem. Dit zou kunnen leiden tot een

hogere patiënten doorstroming en/of toediening van een lagere radiotracer activiteit, wat kosten en stralingsbelasting voor zowel patiënten als personeel kan verminderen, en tegelijkertijd de toepassingsmogelijkheden van (kwantitatieve) PET kan uitbreiden.

Deel 2: Nieuwe klinische toepassingen van kwantitatieve SPECT/CT

Myocardperfusiescintigrafie is gebaseerd op de visuele beoordeling van de relatieve doorbloeding van het hartspierweefsel en kan de ernst van ischemie onderschatten wanneer er sprake is van een verminderde doorbloeding in het hele hart (3-vastlijden). Kwantitatieve SPECT kan mogelijk op een kwantitatieve manier de opname van [99mTc] Tc-tetrofosmine in het myocard meten, om zo de evaluatie van de respons op antiischemische therapieën met behulp van myocardperfusiescans te verbeteren.

Hoofdstuk 5 onderzocht de kwantitatieve nauwkeurigheid en precisie van een nieuwe iteratieve reconstructietechniek (Evolution; GE Healthcare) voor de mogelijke toepassing bij responsmonitoring met [99mTc]Tc-tetrofosmine SPECT/CT bij patiënten met coronaire hartziekte (CAD). Uit onze fantoomstudie bleek dat zeven iteraties (10 subsets) en Butterworth-nabewerking (cut off frequentie 0,52 cycli/cm, orde 5) optimaal waren voor reconstructie op basis van convergentie en ruisniveau. Bij toepassing van deze instellingen was de gemiddelde precisie van alle acquisities 2,91%. Bovendien leidde de nauwkeurigheid van Evolution bij grotere defecten tot hogere recovery coefficient (RC)-waarden (variërend van 0,64 tot 0,75) in vergelijking met kleinere defecten (RC variërend van 0,52 tot 0,74). Om de klinische toepasbaarheid te illustreren, werden tien patiënten retrospectief geïncludeerd, vóór en na intramyocardiale injectie van autologe beenmergcellen. Bij acht van de tien patiënten werd een significante verandering in opname vastgesteld vóór en na behandeling (p < 0,05). Dit was de eerste studie die Evolution evalueerde voor cardiale toepassingen en veelbelovende resultaten toonde voor het gebruik van kwantitatieve SPECT bij patiënten met CAD.

Moleculaire Borstbeeldvorming (MBI) is een niet-invasieve beeldvormende techniek voor de *in vivo* karakterisering van borstlaesies. Hierbij wordt gebruikgemaakt van het radiofarmacon [99mTc]Tc-sestamibi, een substraat van P-glycoproteïne (Pgp), waarmee mogelijk chemoresistentie kan worden voorspeld op basis van de hoogte van de traceropname. Een verminderde traceropname kan wijzen op overexpressie van Pgp, wat de tumorespons op neoadjuvante chemotherapie zou kunnen voorspellen. De kwantificering van de [99mTc]Tc-sestamibi-stapeling zou dan ook kunnen helpen bij het nemen van behandelbeslissingen. Recente studies wijzen echter op beperkingen van planaire MBI bij het nauwkeurig kwantificeren van opname van de tracer in de tumor, waarbij SPECT/CT mogelijk uitkomst biedt. Daarnaast is er de techniek van *prone hanging breast* SPECT, waarbij de patiënt tijdens de beeldvorming in buikligging met hangende

borsten wordt gepositioneerd om verzwakkings- en bewegingsartefacten te verminderen. Hoofdstuk 6 evalueerde de semi-kwantitatieve SPECT-parameters van prone hanging breast SPECT met [99mTc]Tc-sestamibi en vergeleek deze met MBI-afgeleide semikwantitatieve parameters voor mogelijke toepassing bij responsvoorspelling bij vrouwen met lokaal gevorderde borstkanker (LABC). Achttien patiënten met bewezen LABC met een tumor ≥2 cm diameter op mammografie en een indicatie voor MBI met [99mTc]Tcsestamibi werden prospectief geïncludeerd. Verschillende semi-kwantitatieve parameters werden berekend voor vroege en verlate SPECT-acquisities (5 min en 90 min postinjectie) en voor MBI. Er werd geen significant verschil gevonden tussen MBI en vroege SPECT voor de semi-kwantitatieve parameter functioneel tumorvolume (FTV) (p = 0.46). TBR_{mean} en TBR_{max} waren significant hoger bij SPECT in vergelijking met MBI en toonden grotere variabiliteit tussen metingen (p < 0,05). Daarnaast toonden de wash-out rates (WOR) een grote interkwartielbereik (IQR = 62.28), wat duidt op variatie in WOR tussen LABC-patiënten. Ook bleek de FTV afgeleid van vroege prone hanging breast SPECT/ CT vergelijkbaar met die van MBI (p = 0,46). Dit was de eerste haalbaarheidsstudie die de semi-kwantitatieve parameters van prone hanging breast SPECT/CT met [99mTc]Tcsestamibi onderzocht en vergeleek met MBI-parameters bij 18 patiënten met LABC. Deze studie vormde de eerste stap richting een mogelijke toepassing van semi-kwantitatieve prone hanging breast SPECT/CT-parameters bij LABC-patiënten om de respons op neoadjuvante chemotherapie te voorspellen.

Concluderend kan worden gesteld dat er uitgebreide technologische mogelijkheden bestaan die kwantitatieve PET- en SPECT-beeldvorming mogelijk maken. De brede implementatie in de klinische praktijk wordt echter belemmerd door het trage tempo waarin robuust klinisch bewijs wordt gegenereerd. Hoewel deze technieken effectief zijn binnen reeds gevestigde klinische toepassingen (zoals de kwantificatie van myocardperfusie, patiëntstratificatie (t.b.v. theranostics) en voorspelling van therapierespons), is verder onderzoek essentieel om hun bredere klinische inzet te valideren. Meer klinisch bewijs voor nieuwe toepassingen van kwantitatieve SPECT en PET zal het mogelijk maken om met deze technologieën meer gepersonaliseerde behandelingen te ondersteunen en de klinische uitkomsten te verbeteren. Dit proefschrift levert een bijdrage door nieuwe toepassingen van kwantitatieve PET en SPECT te onderzoeken binnen de infectiologie, nefrologie, oncologie en cardiologie, maar er is nog veel werk te verrichten. Aanvullend onderzoek is noodzakelijk om kwantitatieve SPECT- en PET-technieken verder te verbeteren, zodat hun klinische potentie kan worden benut en beschikbaar gemaakt kan worden voor grotere groepen patiënten.



APPENDICES

Curriculum vitae
List of publications
Dankwoord

Œ

CURRICULUM VITAE



Alina van de Burgt was born on the 6th of June 1993 in Arnhem, the Netherlands. In 2011 she graduated from high school at Dorenweerd college Doorwerth. She started with a bachelor's degree in Technical Medicine, earning her undergraduate degree in 2015. Subsequently, she followed a master's program in Technical Medicine (Medical Imaging and Interventions) at the University of Twente in Enschede. After the first year of her master's program, she participated in the Wu Xing study tour (China) with the research topic *The mutual influence of modern and traditional Chinese medicine*. Subsequently, she completed an extracurricular semester in Biomedical Engineering at Hanvang

University (Seoul, South Korea).

During the second year of her master's program, she completed four 10-week internships in the departments of Vascular Surgery (Rijnstate, Arnhem), Orthopedics (Amsterdam UMC), Breast Oncology & Surgery (Guy's Hospital, London), and Siemens Healthineers (The Hague). She also conducted her clinical graduation project in the Radiology department, section Nuclear Medicine, at Leiden UMC. Following the publication of her graduation research, she undertook further investigations driven by personal interest, ultimately resulting in this thesis.

In 2019, she started a new role as a technical physician in the Nuclear Medicine department at Alrijne Hospital. She was responsible for the implementation of technologies and research in clinical practice. In 2021, she began a two-year clinical fellowship in cardiac imaging at Alrijne Hospital. Within this fellowship, she focused on clinical reporting of cardiac scans (MRI, PET, SPECT, and CT) and the optimization of clinical workflows. In February 2024, she joined the Radiology and Nuclear Medicine department at Erasmus MC Rotterdam as a technical physician. She has been responsible for implementing new techniques in clinical practice, as well as conducting scientific research and optimizing protocols.

LIST OF PUBLICATIONS

- van de Burgt, A., Dibbets-Schneider, P., Kotasidis, F., de Geus-Oei, L. F., Rietbergen, D. D., & van Velden, F. H. (2025). [18F]FDG administered activity reduction capabilities of a 32-cm axial field-of-view solid-state digital bismuth germanium oxide PET/CT system while maintaining EARL compliance. *Physica Medica*, *131*, 104935.
- van de Burgt, A., van Velden, F. H., Corion, C. L., Collarino, A., Valdés Olmos, R. A., Smit, F., de Geus-Oei, L. F & Pereira Arias-Bouda, L. M. (2024). Comparison Between Prone SPECT-Based Semi-Quantitative Parameters and MBI-Based Semi-Quantitative Parameters in Patients with Locally Advanced Breast Cancer. *Molecular Imaging and Biology*, 26(6), 926-933.
- Polomski, E. A., Kapiteijn, E. W., Heemelaar, J. C., van der Kolk, A. V., Kalisvaart, T. M., van de Burgt, A., Dibbets-Schneider, P., van Velden, F. H., Seijkens, T. T. P., Stöger, L., Jukema, J. W., de Geus-Oei, L. F., & Antoni, M. L. (2024). Arterial inflammation on [18F]FDG PET/CT in melanoma patients treated with and without immune checkpoint inhibitors: CHECK-FLAME I. *Atherosclerosis*, *398*, 118595.
- Leerling, A. T., Cañete, A. N., Smit, F., Hamdy, N. A., van de Burgt, A., Appelman-Dijkstra, N. M., Dekkers, O.M., & Winter, E. M. (2024). Pamidronate for pain in adult chronic nonbacterial osteitis: protocol of a randomized, double-blind, placebo-controlled trial. *JBMR Plus*, 8(10), ziae114.
- van de Burgt, A., van Velden, F. H., Kwakkenbos, K., Smit, F., de Geus-Oei, L. F., & Dekkers, I. A. (2024). Dynamic rubidium-82 PET/CT as a novel tool for quantifying hemodynamic differences in renal blood flow using a one-tissue compartment model. *Medical Physics*. 51(6), 4069-4080.
- van de Burgt, A., Hezemans, R. E., Smit, F., Bénard, M. R., & Jansen, J. A. (2024). Sodium fluoride PET/CT with arthrography for cartilage evaluation of the knee. *Radiology Case Reports*, *19*(5), 1855-1858.
- Leerling, A. T., Smit, F., Späth, Z., Cañete, A. N., de Geus-Oei, L. F., van de Burgt, A., Dekkers, O.M, van der Bruggen, W., Appelman-Dijkstra, N.M., Vriens D., & Winter, E. M. (2024). ¹⁸F-Sodium fluoride PET-CT visualizes disease activity in chronic nonbacterial osteitis in adults. *JBMR Plus*, 8(2), ziad007.

- Chen, L. L.*, van de Burgt, A.*, Smit, F., Audhoe, R. S., de Boer, S. M., van Velden, F. H., & de Geus-Oei, L. F. (2023). Investigating the potential added value of [18F]FDG-PET/CT in long COVID patients with persistent symptoms: a proof of concept study. *Nuclear Medicine Communications*, 44(6), 495-501.

 *shared first authorship
- Hezemans, R.E., **van de Burgt, A.**, Smit, F., & Pereira Arias-Bouda, L.M. (2022). Comparing [18F]FACBC and [18F]FES as high potential non-FDG PET tracers in ILC: Don't forget about the forgotten tracer FACBC! *TvNG*. *44*(2), 2884-2887.
- van de Burgt, A., Dibbets-Schneider, P., Slump, C. H., Scholte, A. J., Atsma, D. E., de Geus-Oei, L. F., & van Velden, F. H. (2021). Experimental validation of absolute SPECT/CT quantification for response monitoring in patients with coronary artery disease. *EJNMMI Physics*, 8(1), 48.
- **van de Burgt, A.**, Smit, F., & Anten, S. (2021). Rubidium-82 PET/CT in COVID-19. *Radiology Case Reports*, *16*(11), 3478-3480.

DANKWOORD

Dit proefschrift is tot stand gekomen dankzij waardevolle samenwerkingen en de vele fijne momenten die daarbij kwamen kijken. Daarom wil ik graag een aantal mensen speciaal bedanken.

Prof. dr. L.F. de Geus-Oei, beste Lioe-Fee, zelf wist ik aanvankelijk niet zeker of ik wilde promoveren, maar door jouw vermogen om altijd in mogelijkheden te denken en anderen te inspireren hetzelfde te doen, heb ik die stap gezet. Heel veel dank voor alle kansen, motivatie en de betrokken begeleiding die je mij in deze periode hebt gegeven.

Dr. F.H.P. van Velden, beste Floris, ontzettend bedankt voor je bevlogen begeleiding en enthousiasme, die samen met jouw positiviteit en integriteit aanstekelijk werken en mij altijd hebben aangemoedigd in mijn onderzoek. Daarnaast vond ik het ontzettend leuk om met jou onze passie voor de stad Amsterdam te delen, inclusief alle leuke evenementen die daar te vinden zijn.

Dr. I. A. Dekkers, beste Ilona, voor jouw fellowship was je regelmatig in het Alrijne, waar we elkaar vonden en al snel projecten met studenten hadden opgezet. Ik waardeer onze samenwerking, met als bijzonder hoogtepunt onze ISMRM-congrestrip naar Londen, dankjewel!

Veel dank aan alle studiepatiënten voor hun deelname en het beschikbaar stellen van data. Zonder jullie bijdrage was dit proefschrift niet mogelijk geweest.

Mijn oud-collega's van het Alrijne, in het bijzonder Frits, Sandra, Lenka, Rowena, Rachel, Richard, Nicole, Nick en Tjerk, ik heb een ontzettend leuke en leerzame tijd bij jullie gehad! Het is indrukwekkend om te zien hoeveel innovatie er op de afdeling nucleaire geneeskunde plaatsvindt. Ik hoop dat dit proefschrift heeft bijgedragen aan het verder benadrukken hiervan.

Hoewel ik een ongebruikelijk pad heb gevolgd en slechts een jaar in het LUMC heb doorgebracht, ben ik regelmatig langsgekomen bij de geweldige groep mensen op de afdeling nucleaire geneeskunde. Graag wil ik Petra in het zonnetje zetten; heel erg bedankt voor alle fantoomproeven, die jij altijd als een "speeltje" zag. Het is inspirerend om te zien hoe onderzoek altijd een passie voor je is gebleven! In het bijzonder wil ik de collega's van 'the Corner Office' bedanken, waar ik altijd welkom was. Veel dank aan Wyanne, Pim, Willem, Joeri, Dennis, Karin, Hanneke, Timo, Maaike, Fleur, Marijn, Sietse, Ylva, Vesna en Gonnie voor de research- en Cherry meetings, tripjes naar Antwerpen, de

congressen en vooral de Italiaanse (VIP) en muzikale hoogtepunten in stamkroeg Café 't Centrum van Melzen!

Huidige collega's in het Erasmus MC, hartelijk dank voor jullie interesse in mijn promotieonderzoek en de kans die ik kreeg om mij verder te ontwikkelen binnen de academie.

Lieve Floortje (Flora) en Eline (Khoter), we hebben samen prachtige avonturen beleefd tijdens onze studietijd en nog steeds, vaak vergezeld van urenlange gesprekken met een hapje en een drankje. Dank jullie wel dat jullie mijn paranimfen willen zijn.

Veel dank aan mijn vrienden en vriendinnen voor de fijne momenten samen in alle vormen: van etentjes en borrels tot wandelingen, dansen, sporten en gezamenlijke vakanties. Ik ben ontzettend dankbaar voor zulke geweldige mensen om me heen, die inspireren, een luisterend oor bieden, goede gesprekken mogelijk maken en, minstens zo belangrijk, altiid zorgen voor plezier en ontspanning!

Graag wil ik mijn (schoon)familie heel erg bedanken voor jullie betrokkenheid bij mijn promotie en bij alles ver daarbuiten!

Lieve Ivar, bedankt dat je altijd in mij gelooft en klaarstaat voor mij. Ik ben met dit proefschrift weer een stapje dichterbij de nobelprijs, zoals jij altijd zegt. Lieve Margriet, wat ben ik blij dat jij bij onze familie bent gekomen!

Lieve papa en mama, heel erg bedankt voor jullie onvoorwaardelijke liefde, steun en de kansen die jullie mij hebben geboden. Jullie hebben me geleerd dat je met nieuwsgierigheid en hard werken ver kan komen in het leven. Deze waardevolle basis heeft me enorm geholpen tijdens dit promotietraject!

Lieve Sjoerd, bedankt voor je steun, vertrouwen en liefde. Je weet altijd precies wat ik nodig heb om gemotiveerd te blijven en mijn doelen te bereiken. Ik kijk ernaar uit om samen nog veel mooie avonturen te beleven!